

8-2001

# Influence of viscoelasticity on the nano-micromechanical behavior of latex films and pigmented coatings

Manish Giri

Follow this and additional works at: <http://digitalcommons.library.umaine.edu/etd>



Part of the [Chemical Engineering Commons](#)

---

## Recommended Citation

Giri, Manish, "Influence of viscoelasticity on the nano-micromechanical behavior of latex films and pigmented coatings" (2001).  
*Electronic Theses and Dissertations*. 247.  
<http://digitalcommons.library.umaine.edu/etd/247>

This Open-Access Dissertation is brought to you for free and open access by DigitalCommons@UMaine. It has been accepted for inclusion in Electronic Theses and Dissertations by an authorized administrator of DigitalCommons@UMaine.

**INFLUENCE OF VISCOELASTICITY ON THE NANO-MICROMECHANICAL  
BEHAVIOR OF LATEX FILMS AND PIGMENTED COATINGS**

By

Manish Giri

B.S., University of Roorkee, Roorkee, India, 1996  
M.S., Oregon State University, Corvallis, Oregon, 1998

A THESIS

Submitted in Partial Fulfillment of the

Requirements for the Degree of

**Doctor of Philosophy**

(in Chemical Engineering)

The Graduate School

The University of Maine

August, 2001

Advisory Committee:

William N. Unertl, Professor of Physics, Co-Advisor

Douglas W. Bousfield, Professor of Chemical Engineering, Co-Advisor

Vincent Caccese, Professor of Mechanical Engineering

Albert Co, Professor of Chemical Engineering

Nick Triantafillopoulos, Adjunct Professor of Chemical Engineering, OMNOVA  
Solutions

# INFLUENCE OF VISCOELASTICITY ON THE NANO-MICROMECHANICAL BEHAVIOR OF LATEX FILMS AND PIGMENTED COATINGS

By Manish Giri

Thesis Co-Advisors: Dr. William N. Unertl and Dr. Douglas W. Bousfield

An Abstract of the Thesis Presented  
in Partial Fulfillment of the Requirements for the  
Degree of Doctor of Philosophy  
(in Chemical Engineering)

August, 2001

Nano to microscale deformation behavior of different carboxylated styrene-butadiene copolymer Latexes were investigated using a commercial nanoindentation device. The latexes differed primarily in their glass transition temperature ( $T_g$ ). The bulk dynamic rheological properties, as determined from a rheometer, dictate the axisymmetric deformation behavior of the latexes. Results from dynamic tests performed on latexes were analyzed using the theories in contact and fracture mechanics. Two theories of linear viscoelastic fracture mechanics (LVEFM) were employed to model the *adhesion hysteresis* (loading-unloading cycle) curves to obtain meaningful **cohesive** zone (fracture process zone) parameters and a stress intensity functional ( $K_I(t)$ ) for an entire cycle. The stress intensity functional, extracted from the deformation behavior, is independent of the loading history and was shown to depend only on the crack propagation velocity,

( $da/dt$ ), for the entire cycle. The quantitative values of stress intensities were then discussed in the light of polymer molecular phenomenon's such as viscous chain desorption. Nanoindentation was developed as a tool for systematically investigating both the bulk as well as the *cohesive* zone properties of viscoelastic polymers.

Effect of plastic deformation on the deformation behavior of high pigment volume concentration (PVC) coatings was also analyzed. Polystyrene plastic pigment,  $\text{CaCO}_3$  and Clay pigments were used to form the coatings layers. High PVC coatings are viscoelastic due to the latex present but also contain air, the third phase, which could explain the plastic deformation if a certain critical yield stress is exceeded. At PVC's greater than 70%, the coatings showed significant plastic (permanent) deformation, which has to be accounted for in modeling the hysteresis curves. The residual plastic deformation was confirmed by imaging the indent over a period of time. Modeling the curves resulted in a compressive yield stress ( $\sigma_y$ ) value, which is an important parameter in predicting the calendaring performance of these coatings.

## Acknowledgements

I would like to sincerely thank my thesis advisor, Dr. William N. Unertl and Dr. Douglas Bousfield, for their research guidance, professional advice, and friendship over the years. I would also like to thank my other committee members, Dr. Vinecent Cassese, Dr. Albert Co and Dr. Nick Triantafillopoulos for their interest and advice. I would also like to thank Yu-Yun Lin and Dr. C.-Y. (Herbert) Hui for their technical support.

I would also like to express my gratitude to all the members of the Paper Surface Science Program (PSSP) for providing the financial support and expressing interest in my work. I feel fortunate to have performed my thesis work surrounded by all the wonderful people of LASST. I would also like to acknowledge the support and guidance of Eugeneue Popescu and Nicoleta Mihai.

I would also like to thank my family and friends for their support and encouragement through this. Finally, I wish to express my gratitude to my biggest supporters, my parents, without whom I would never have made it this far. This acknowledgement would not be complete without my deep expression of thanks to my fiancéé, Candace Smejkal. Without her love, support and encouragement this work would not have been possible.

## Table of Contents

Acknowledgements .....	ii
List of Tables .....	vii
List of Figures .....	viii
PART 1: Background .....	1
Chapter 1. Introduction .....	4
1.1 References for chapter 1 .....	6
Chapter 2. Experimental Method .....	7
2.1 Introduction .....	7
2.2 Mode of operation .....	7
2.3 Indenter tips .....	<b>9</b>
2.4 References for chapter 2 .....	10
Chapter 3. Theoretical Background .....	11
3.1 Linear Elastic Fracture Mechanics (LEFM) .....	11
3.1.1 The cohesive zone .....	11
3.1.2 The Dugdale-Bareblatt crack .....	13
3.1.3 Griffith's crack propagation criteria .....	15
3.1.4 Rice's J-Integral .....	16
3.1.5 The JKR theory of contact mechanics .....	18
3.2 Linear Viscoelastic Fracture Mechanics (LVEFM) .....	20
3.2.1 Johnson's crack tip creep theory .....	23
3.2.2 The Hui, Baney, Kramer theory for bonding .....	24
3.2.3 The Lin, Hui, Baney theory for dedonding .....	27
3.2.4 Energy dissipation during viscous chain pull-out .....	32

3.3 Visco-elasto-plastic deformation .....	33
3.3.1 The yield stress criterion .....	35
3.3.2 Regimes of deformation .....	36
3.3.3 Johnson's model for evaluating material yield stress .....	37
3.4 References for chapter 3 .....	40
PART 11: Dynamic Contacts to Viscoelastic Styrene-butadiene Latex Films .....	42
Chapter 4. Latex Film Rheological Properties .....	42
4.1 Sample preparation for dynamic mechanical testing .....	42
4.2 Material creep compliance .....	43
4.3 References for chapter 4 .....	45
Chapter 5. Low Loading Rate Contacts to <b>SB</b> Latex Films .....	46
5.1 Introduction .....	46
5.2 Experimental details .....	46
5.3 Cyclic loading-unloading tests .....	50
5.4 Results and Discussion (Work of adhesion) .....	54
5.5 Conclusions .....	62
5.6 References for chapter 5 .....	63
Chapter 6. Creep tests performed on <b>SB</b> Latex films .....	64
6.1 Introduction .....	64
6.2 Experimental method .....	64
6.3 Results .....	65
6.4 Discussion .....	68
6.5 Conclusions .....	74

6.6 References for chapter 6 .....	76
Chapter 7. Dynamic cyclic tests at all loading rates .....	77
7.1 Introduction .....	77
7.2 Experimental details.....	79
7.3 Results and Discussion .....	84
7.4 Conclusions .....	90
7.5 References for chapter 7 .....	92
Chapter 8. Summary of Linear Viscoelastic Fracture Studies .....	93
8.1 Conclusions .....	93
8.2 Future extensions .....	93
8.3 References for chapter 8 .....	94
<b>PART ■ Dynamic Contacts to Visco-Elasto-Plastic Coating Composites .....</b>	<b>95</b>
Chapter 9. Contacts to pigmented coatings .....	95
9.1 Introduction .....	95
9.2 Motivation .....	96
9.2.1 Effective Medium Approach .....	96
9.2.2 Calendering .....	97
9.2.3 Printing .....	99
9.3 Experimental .....	99
9.4 Results .....	108
9.5 Discussions .....	122
9.6 Conclusions .....	125
9.7 References for chapter 9 .....	127

Chapter 10. Summary of Viscoelastoplastic fracture studies .....	129
10.1 Conclusions .....	129
10.2 Future Extensions .....	129
 PART IV: Influence of Substrate Roughness and Compressibility on Blade Coating .....	130
Chapter 11. A Semi-Quantitative Study of Blade Coating (Simulation) .....	130
11.1 Introduction .....	130
11.2 Compression measurements .....	133
11.3 Model development .....	135
11.3.1 Solid Mechanics .....	135
11.3.2 Fluid Mechanics .....	137
11.4 Results .....	139
11.5 Conclusions.....	143
11.6 References for chapter 11.....	143
 PART V: Summary of Dissertation .....	146
Chapter 12. Summary .....	146
12.1 References for chapter 12 .....	148
 Bibliography .....	149
Appendix A. MathCad file extract for the Johnson's crack tip creep approach .....	158
Appendix B. MathCad file extract for the HBKL complete approach .....	<b>160</b>
 Biography of the Author .....	163

**List of Tables**

Table 4.1 Rheological properties of latexes .....	45
Table 5.1 Styrene-Butadiene/Acrylate latex Parameters.....	47
Table 5.2 Cohesive zone parameters .....	61
Table 9.1 Description of pigmented coatings .....	100
Table 9.2 Dynamic mechanical properties of coatings and their yield stress values.....	108

## List of Figures

Figure 2.1 Nanoindenter Schematics .....	8
Figure 2.2 (a) and (b) Typical Test Protocols .....	9
Figure 2.3 (a) and (b) Images of Different Indenter tips .....	10
Figure 3.1 The cohesive zone .....	12
Figure 3.2 The interaction potentials .....	14
Figure 3.3 Crack tip process zone .....	17
Figure 3.4 An adhesive elastic contact .....	18
Figure 3.5 An approximate crack tip schematic .....	20
Figure 3.6 Contact radius for an entire loading-unloading cycle .....	27
Figure 3.7 Predictions of Fracture Energy from viscous polymer chain desorption theory .....	33
Figure 3.8 An Elastic-Plastic Contact .....	34
Figure 3.9 Residual plastic deformation and recovered crown .....	38
Figure 4.1 Rheological properties of Styrene-butadiene Latexes .....	44
Figure 5.1a Load-displacement plotted vs. time for a typical cyclic test .....	48
Figure 5.1b A typical load-displacement (Adhesion hysteresis) curve .....	49
Figure 5.2a Cyclic tests done at different rates on latex # 1 .....	51
Figure 5.2b Cyclic tests done at different rates on latex # 2 .....	52
Figure 5.2c Cyclic tests done at different rates on latex # 3 .....	52
Figure 5.3 Model fits to hysteresis curves obtained at low loading rates .....	55
Figure 5.4a Typical low loading rate test results using the spherical indenter, with varying work's of adhesion .....	56
Figure 5.4b Effect of varying $W_{ad}$ on the quality of fit .....	56
Figure 5.4c Fits with varying range parameter ( $h_c$ ) .....	57

Figure 9.3 **A** SEM micrograph of the Berkovich indenter ..... 103

Figure 9.4 *a)* **A** typical indent on Coating I made with a Berkovich probe upto a depth of about 1600 nm and *b)* image of the indent over a period of 4 hours using the indenter itself. The final plastic deformation,  $\delta_f$  is about 460 nm ..... 105

Figure 9.5 *a)* **A** typical indent on Coating II made with a Berkovich probe upto a depth of about 1600 nm and *b)* image of the indent over a period of 4 hours using the indenter itself. The final plastic deformation.  $\delta_f$  is about 660 nm ..... 106

Figure 9.6 *a)* **A** typical indent on Coating III made with a Berkovich probe upto a depth of about 1900 nm and *b)* image of the indent over a period of 4 hours using the indenter itself. The final plastic deformation.  $\delta_f$  is about 310 nm.  
This coating shows most recovery ..... 107

Figure 9.7 Creep test results of Different Pigmented Coatings..... 109

Figure 9.8a Creep behavior of different PVC's of Polystyrene/Latex coatings..... 111

Figure 9.8b Elastic modulus as function of PVC ..... 111

Figure 9.9 Evolution of indents over time..... 112

Figure 9.10 Regimes of deformation in an viscoelastoplastic contact..... 115

Figure 9.11 Cyclic test at the same location on coating I..... 116

Figure 9.12 Model fits to indents in Fig. 9.6 using the viscoelastoplastic approach.....118

Figure 9.13 Cyclic test on coating I at different locations ..... 119

Figure 9.14 Cyclic test on coating II at different locations ..... 120

Figure 9.15 Cyclic test on coating III at different locations ..... 121

Figure 11.1 Schematic of a tip contacting a rough surface ..... 133

Figure 11.2 Typical load displacement curve with a creep section..... 134

Figure 11.3 Modulus and Hardness values as a function of depth..... 135

Figure 11.4 Schematic of blade coating process on a rough, compressible substrate..... 136

Figure 11.5 Pressure distribution with $h = 0.18$ mm and $\mathbf{A} = 1$ and 5pm.....	139
Figure 11.6 Pressure distribution with $h = 0.05$ mm and $\mathbf{A} = 1$ and 5pm.....	140
Figure 11.7 Pressure distribution with $\mathbf{A} = 5$ pm and roughness out of phase.....	140
Figure 11.8 Influence of web compressibility on pressure distribution .....	141
Figure 11.9 Pressure distribution with compressibility and roughness .....	142
Figure B.1 MathCad subroutine showing the method for calculating the contact radius during the loading portion .....	160
Figure B.2 MathCad subroutine showing the method for calculating the contact radius during the creep portion .....	161
Figure B.3 MathCad subroutine showing the method for calculating the stress intensity during the crack closing portion .....	161

## **PART I: Background**

In this thesis the nano-micromechanical deformation behavior of elastic, viscoelastic and viscoelastic plastic films have been analyzed using a commercial nanoindentation device. Nano to micro-scale deformation behavior is an important aspect in designing as well as understanding the performance of materials. The application of probe techniques in investigating the response of materials has been well documented. Probe techniques such as the Nanoindentation device and the Atomic Force Microscope (AFM) involve a well-defined probe geometry, which comes into contact with a surface to be investigated. In a contact experiment the probe comes into contact with the surface, indents the surface and finally, pull's off from the surface. The result of such an experiment is a force-displacement curve. A typical force displacement curve is governed by the by the probe shape, the probe-surface interaction potential, the surface modulus and thickness. Hence one of the main advantages of surface probe techniques is their ability to shed light on the both the surface interfacial as well as the bulk properties. A typical result from probe contact test consists of contributions from both the material surface and bulk. Hence deconvoluting the results is a major hurdle in justifying the overall usefulness of contact probe tests. There are various other ways of investigating the surface and bulk material properties of materials. Surface properties can be examined by electron impingement techniques (**ESCA, XPS**), spectroscopy techniques (FTIR, ATR, Raman) and the bulk properties, such as modulus, can be measured by techniques like the Instron and Dynamic Mechanical Thermal Analyzer (DMTA). These separate techniques are therefore required for a complete material analysis.

Metrology techniques such as Scanning Probe Microscopy (SPM), have recently gained importance since they can reveal precise surface topological information, along with the surface modulus. SPM can be extended to study the chemical behavior of surfaces. The chemical composition of the surface influences the forces resulting from the adhesion of the probe with the surface. These techniques can also be used to study the tribological properties of surfaces in the

form of Lateral Force Microscopy (LFM) and the chemical forces originating in a liquid environment in the form of Chemical Force Microscopy (CFM). Hence due to their wide range of applicability, SPM techniques have recently come to the forefront. As mentioned above, one of the major hurdles in analyzing the experimental data from a typical SPM experiment is that the material modulus,  $E$ , must be known a priori. This enables determining the work of adhesion,  $W$ , between the probe and the surface. Theoretical developments in the field of contact mechanics have enabled determination of surface work of adhesion for pure elastic materials from a typical SPM experiments. The most commonly used theory of contact mechanics was first formulated by Johnson, Kendall and Roberts (described later) and is referred to as the JKR theory. The details of this theory and its restrictions in analyzing the behavior of anelastic materials will be discussed in the later chapters.

In industrial operations, which involve two contacting surfaces, SPM techniques are especially useful. In the paper and coatings industry, processes such as coating, calendering and printing involve two surfaces (liquid/solid) coming in contact. The contact interface is dynamic involving interaction of fluid mechanics with solid mechanics. In order to completely understand these process we need to systematically understand both fluid as well as solid mechanics. A lot of work has already gone into coating and ink fluid mechanics. Deformation behavior of solids under time and temperature dependent stresses, however, lacks an in-depth understanding. Recently efforts have focussed on analyzing the material properties using an Instron and Dynamic mechanical thermal analyzer. These techniques have proven to be useful in examining the bulk material behavior. But for processes where two surfaces come in contact followed by a contact rupture both the material bulk and interface play role. Hence it is important to use an experimental technique which probes both the material bulk and interfacial behavior. It is the purpose of this thesis to address certain issues in solid mechanics through simple experiments using a nanoindentation device. The analysis of our experiments will be based on recent theoretical developments in contact and fracture mechanics.

In the first part of this thesis, elastic, viscoelastic and viscoelstoplastic fracture mechanics are discussed. Linear elastic materials regain their original structure once the deforming force is withdrawn. Hence all the deformation energy is completely recovered. Fused quartz behaves as a linear elastic material at room temperature ( $\approx 25^\circ\text{C}$ ). Viscoelastic materials exhibit a time dependent response. The material does not instantly regain its original configuration once the deforming force is withdrawn. Instead, depending on the materials relaxation characteristics, the imposed is completely recovered over a period of time. Elastic-Plastic materials essentially behave as purely elastic materials if the material yield stress,  $\sigma_Y$ , is not exceeded. If the imposed stress exceeds the material yield stress, then the material shows permanent deformation. Viscoelstoplastic materials are like elastic-plastic materials except that they have a time dependent elastic component within the elastic limit. Beyond the elastic limit these materials also exhibit plastic (permanent) deformation. Our goal was to study the nanoscale fracture behavior of these materials.

Linear elastic fracture mechanics is applicable for a wide variety of materials but breaks down for viscoelastic materials. Two recent theories have been proposed to handle linear viscoelastic material behavior. They will be discussed in the linear viscoelastic fracture mechanics section. Finally we will discuss linear viscoelstoplastic fracture mechanics since most practical materials used in the industry are viscoelstoplastic. In the second part results from studies on viscoelastic styrene-butadiene latexes will be presented. In the third part results from studies on viscoelstoplastic pigmented coatings will be presented and finally in the fourth part results from a simulation study of the blade coating operation where fluid mechanics interacts with solid mechanics will be discussed.

## Chapter 1. Introduction

Theoretical models for contacts to viscoelastic materials in the absence of adhesion have been available since the 1960's [1]. In the early 1970's, Barquins and Maugis [2] and Greenwood and Johnson [3] developed models that included adhesion but viscoelastic effects were confined to the periphery of the contact. Johnson later extended this theory to the case of an entire load-displacement cycle. In late 1990's, several experiments demonstrated that viscoelastic effects are not confined to the contact periphery, but include the entire contact zone. Johnson [4] and Unertl [5] have shown that crack tip and long range creep phenomena generally occur on much different time scales. Depending on the characteristic relaxation time of the viscoelastic material and the experimental measurement time, both can be important. Recently, Hui and co-workers [6,7] have put forward a model that accounts for linear viscoelastic response at all length and time scales. Our approach towards describing these contacts in a quantitative way originates from the Johnson-Kendall-Roberts (JKR) theory, as modified by Johnson. After presenting load-displacement data, we demonstrate that this theory provides a robust method to determine the thermodynamic work of adhesion from data obtained at sufficiently low loading rates, if the material compliance is known *a priori*. Work of adhesion,  $\mathcal{W}$  and effective range parameter,  $h_e$ , were determined using the extended JKR model by Johnson. Recent work by Giri et al. [8] shows the details of the procedure for determining the cohesive zone parameters.

The theory by Hui and coworkers [6,7], who extended the work by Schapery [9], is more complete since it is applicable under any loading-unloading condition. This theory however requires an independent determination of the cohesive zone parameters ( $\mathcal{W}$  and  $h_o$ ). They suggest the use of the cohesive zone parameters along with the material properties, to obtain stress intensity functional,  $K_I(t)$ , for the entire loading-unloading cycle under any loading condition. The conventional approach in fracture mechanics is to determine the fracture energy or the strain energy release rate,  $G$ , instead of a stress intensity function. Determination of  $G$  for a viscoelastic

contact is difficult [9] and, therefore, the stress intensity factor approach is more realistic since it also provides detailed information of the crack tip processes. The cohesive zone theory, which uses the viscoelastic correspondence principle, was used for modeling the loading-unloading curves. The determination of stress intensity functional,  $K_I(t)$ , is crucial for the characterization of adhesion between viscoelastic bodies since it controls the stress fields near the contact edge. Once the bonding stress is determined from  $W$  and  $h$ , using the Dugdale-Barenblatt cohesive zone model then a unique relationship between crack propagation velocity  $da/dt$  and  $K_I(t)$ , is obtained. For the bonding (monotonically increasing contact radius) part it was suggested that the stress intensity functional and crack velocity, are related by a simple functional form, which also follows from Schapery's analysis. During loading the initial stress intensity rises rapidly and then slows down with crack velocity. The theory also suggests that a simple relationship might exist between Stress intensity and crack velocity for the debonding phase too, as long as the separation process is not dominated by chemical bond breaking or polymer chain sessions processes. In the first part of this work we investigate the relationship between stress intensity functional,  $K_I(t)$ , and crack velocity for the entire bonding-debonding cycle.

In the second part viscoelastoplastic contacts are dealt with. Recent progress in elastic-plastic contact theory [10] was extended to more realistic viscoelastoplastic materials. This theory takes into account a material compressive yield stress,  $\sigma_y$ , along with the interfacial energetics. Determination of material yield stress for pigmented coatings is important industrial process such calendering and printing. We combine the linear viscoelastic crack tip creep approach suggested by Johnson along with a recent theory proposed by the same author to model contact experiments done on a microscale. This enables determination of material yield stress, which is an important design parameter. This combined theory is approximate but is still useful for understanding the deformation behavior of real composites.

Finally we use a Fortran code to simulate the blade coating of a rough, compressible substrate. This simulation assumes that the material is linear-elastic, isotropic and has a periodic roughness. The simulation results, although preliminary, suggest that the pressure pulse generated underneath the nip could possibly contain multiple fluctuations depending on the extent of roughness and the degree of compressibility. These fluctuations can then potentially harm the uniformity of the coating and lead to printing non-uniformity.

### 1.1 Reference for chapter 1

1. Ting, T C. T. *J. Appl. Mech.* **1966**, 33, 845, Ting, T.C.T. *J. Appl. Mech.* **1968**, 35, 248.
2. Barquins, M., and Maugis, D. *J. Adhesion* **1981**, 13, 53, Barquins, M., *J. Adhesion* **1982**, 14, 63.
3. Greenwood, A. J., Johnson, K. L. *Phil. Mag. A*, **1981**, 43, 697.
4. Johnson, K. L. *Microstructure and Microtribology of Polymer Surfaces*, Eds. V. V. Tsukruk and K. J. Wahl, American Chemical Society, Washington, D.C., **2000**.
5. W. N. Unertl, *Microstructure and Tribology of Polymers*, Eds. . V. V. Tsukruk and K. J. Wahl (American Chemical Society), Washington, DC, **2000**.
6. Hui, C. -Y., Baney, J. M., Kramer, E. J. *Langmuir* **1998**, 14,6570.
7. Lin, Y. Y., Hui, C. -Y., Baney, J. M. *J. Phys. D: Appl. Phys.* **1999**, 32, 2250.
8. Giri, M., Unertl, W. N., Bousfield, D.W. *Tribology Letters*, **2000**, 9, 33.
9. Schapery, R. A. *International J. Fracture* **1989**, 39, 163.
10. Rice, J. M. Proc. 8<sup>th</sup> US Natl. Cong. *Appl. Mech.* LosAngeles: Western Periodicals, **191**, **1979**.
11. Mesarovic, S. Dj., Johnson, K. L. *J. Mech. Phys. of Solids*, **2000**, 48, 2009.

## Chapter 2. Experimental Method

### 2.1 Introduction

In a typical Nanoindentation device a load is continuously applied to the indenter and the depth of penetration of the indenter into the sample is measured in real time as a function of load. For perfectly elastoplastic materials the material properties, such as hardness and elastic modulus, can be estimated from the initial slope of the unloading portion of the load displacement curve using well established models [13]. This method is, however, not valid for studying viscoelastic materials since material creep convolutes its deformation behavior. In this work we use the nanoindentation device to study viscoelastic and viscoelastoplastic materials. The deformation behavior of these materials was modeled using recent developments in the field of fracture and contact mechanics

### 2.2 Mode of operation

The nanoindentation instrument consists of a load-displacement transducer (along with electrostatic force actuation and displacement sensing electronics, Hysitron Inc., Minneapolis, MN) mounted on top of a Atomic Force Microscope (AFM) base with piezo scanner, signal access module and XYZ scanning electronics (Park Scientific CP, Palo Alto, CA). The sample is mounted on the piezo scanner. The experimental set up is shown in Fig.2.1. The load-displacement transducer consists of a three parallel plate (Be-Cu) capacitive structure to apply a force through electrostatic actuation and sense displacement by monitoring the change in capacitance. The maximum applied voltage is in the 10-150 Volts range. The indenter tip is screwed into the tip holder on the center plate, which is spring mounted to the housing. The outer drive plates are fixed. In order to apply a load, a voltage,  $V$ , is applied between the center and the bottom plates. This generates an electrostatic force,  $F$ , given by

$$F = E_f V^2 \quad (1)$$

where  $E_f$  is the electrostatic force constant which is dependent on the area,  $A$ , of the plates and the spacing,  $d$ , between the center and the outer plates.

$$E_f \approx \frac{A}{d^2} \quad (2)$$

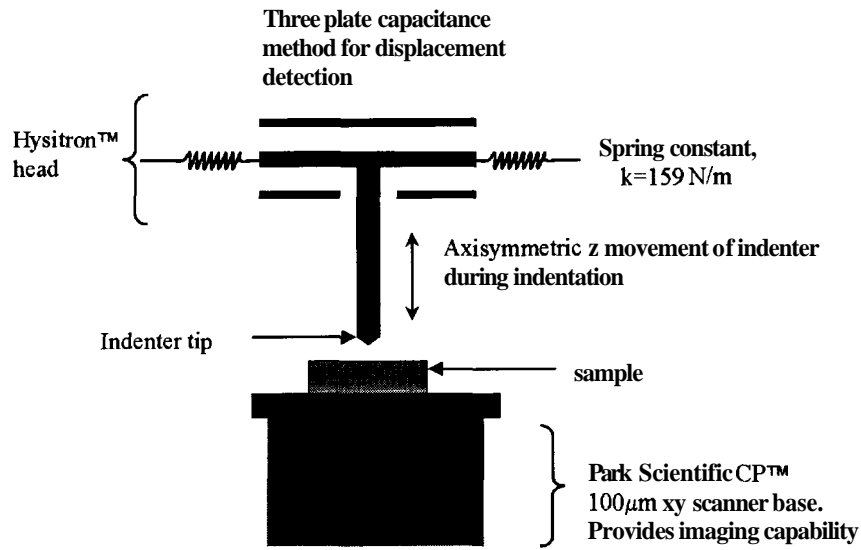


Fig. 2.1 A schematic of the Hysitron Nanoindentation device

The variation of  $E_f$  for this transducer is less than 2% for displacements less than 800nm. The load resolution is  $\sim 100$  nN. Vertical displacement of the tip is determined by measuring the displacement of the center plate relative to the outer plates using the change in capacitance method. The displacement resolution is 0.2 nm. This assembly also allows for indentation as well as imaging capability. The piezo scanner has a lateral scan range of  $100 \times 100 \mu\text{m}^2$  and a vertical  $Z$  range of  $5 \mu\text{m}$ . Indentation experiments can be performed by either the transducer head to generate an indent with force control or by ramping the specimen towards and away from the indenter with displacement control. A computer with data acquisition board (PCI-MIO 16, National Instruments, Austin, TX) is used to control the indenter head and scanner motion as well as col-

lect data. Imaging is accomplished by displacement feedback from the indenter transducer with the AFM scanning electronics and is controlled using the AFM electronics. Fig. 2.2(a) and (b) show typical indentation protocols. Fig. 2.2(a) is a creep test and (b) is a cyclic test. A force modulation capability can also be added to this system to increase its sensitivity. Details of such a modification have been discussed in by Syed Asif et al [2].

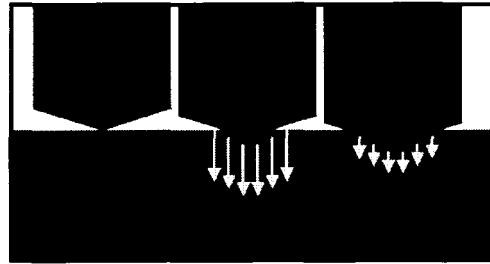


Fig. 2.2 (a) A typical creep test protocol. The test starts with the probe in contact with the sample. A load is applied in 0.05s and held constant for over 60s. Displacement is then plotted as a function of time of deformation.

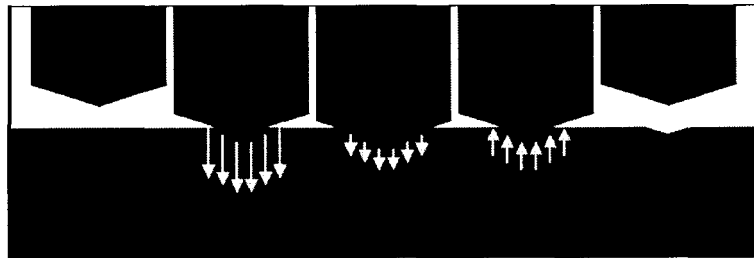


Fig. 2.2 (b) A typical cyclic test protocol. The test starts with the probe out of contact. A cyclic load applied over a time period. A cyclic test results in an adhesion hysteresis curve.

### 2.3 Indenter tips

Two different diamond probes were used for indentation purposes. One was a Berkovich diamond and the other was a paraboloid. The Berkovich probe is a three-sided pyramid with a half angle of  $70.2^\circ$  approximately. The tip of the probe is spherical with a radius of curvature of  $\sim 200$  nm. The paraboloidal probe has a radius of curvature of about  $10\mu\text{m}$ . For all modeling purposes the Berkovich was considered to be a cone and precaution was taken to model indents shall-

lower than 100 nm as spherical contacts. In all cases indents were shallower than 3  $\mu\text{m}$ . Figures 2a and 2b show the different indenter electron micrograph images.

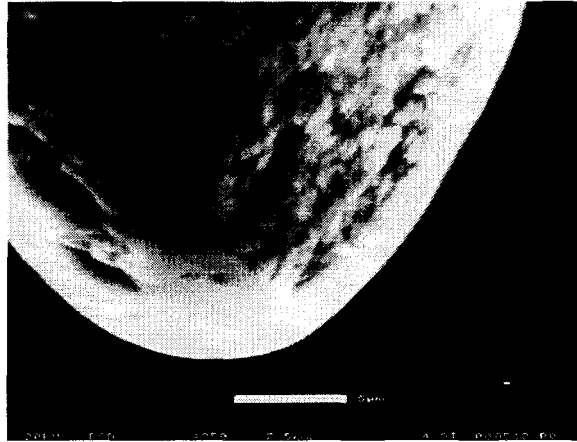


Fig. 2.3 (a) A SEM micrograph of the 10 $\mu\text{m}$  spherical indenter. From the scale of 5 $\mu\text{m}$  it can be seen that the approximate diameter of the probe tip is 20 $\mu\text{m}$ . This was also confirmed with AFM scans of the indenter tip.



Fig. 2.3 (a) An SEM micrograph of the Berkovich indenter. From the scale of 1 $\mu\text{m}$  it can be seen that the probe can be approximated as a cone with the same half angle as the Berkovich (70.29"). The contact area goes with the contact depth as,  $A=24.5h^2$ . Here  $A$  is the contact area and  $h$  is the contact depth.

#### 2.4 References for chapter 2

1. Oliver, W. C., Pharr, G. M. *J. Mater. Res.* 1992, 7, 1564.
2. Asif, S. A. S.; Wahl, K. J.; Colton, R. J. *Rev. Sci. Instrum.* 1999.33, 54

## Chapter 3. Theoretical Background

### 3.1 Linear Elastic Fracture Mechanics (LEFM)

#### 3.1.1 The cohesive zone

The mechanics of contact between a solid hemisphere and a flat surface has been extensively used for studying the surface energy of solids [1-51]. The history of this contact problem has been described in detail in Maugis [6]. Three important but approximate theories have been developed to describe this contact problem. The Hertz theory [7], the Johnson-Kendall and Roberts (JKR) theory [8] and the Derjaguin-Muller-Toporov (DMT) theory [9]. While the Hertz theory assumes that the adhesion between the two contacting bodies cannot be sustained, the JKR and DMT theories allow for adhesion by taking into account the surface energy of the bodies. In the JKR theory the surface energies cause an infinite stress to act at the edge of contact, while in the DMT theory the tensile stress is finite in a cohesive zone outside the contact area but is zero inside.

In Fig. 3.1.1 the small annular region,  $d$ , outside the contact zone  $a$  is the cohesive zone. Maugis [6], used a cohesive zone model to determine the range of applicability of each theory, characterized the transition from DMT to JKR in terms of a single dimensionless parameter  $\lambda$ , which depends on the radius and elastic modulus of the contacting bodies as well as the range and strength of the cohesive forces. Here  $\Lambda$  is the elasticity parameter give by  $\lambda \equiv \sigma_o \sqrt[3]{9R/2\pi WE^*}$ .  $R$  is the radius of the probe,  $W$  is the work of adhesion,  $E^*$  is the effective modulus given by,  $E^* \equiv E/(1-\nu^2)$  where  $E$  is the Young modulus and  $\nu$  is the Poisson ratio. The cohesive zone will be discussed in the light of the Maugis-Dugdale (MD) theory. Figure 3.1.1 shows an intimate contact between a sphere and a flat surface. Contact is maintained over a central region of radius  $a$ , adhesive forces of intensity  $\sigma(r)$  extend to a radius  $c$ .

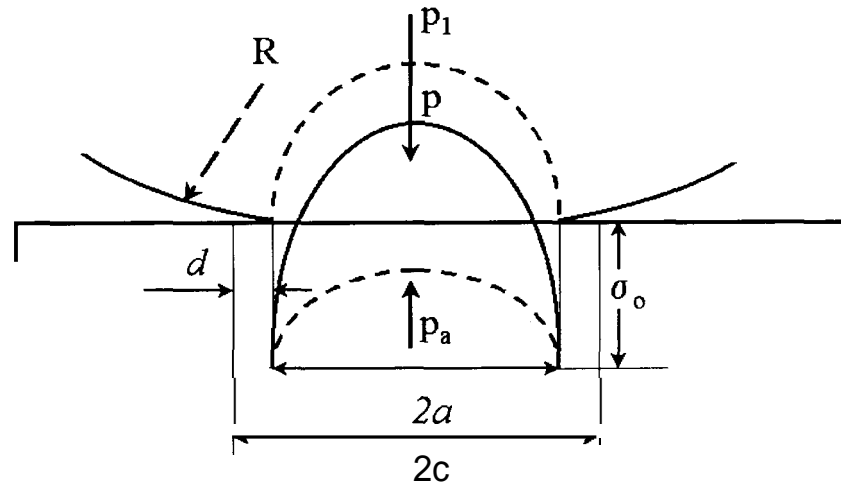


Fig. 3.1 The Cohesive zone model as proposed by Maugis.  $R$  is the probe radius,  $p_1$  is the pressure distribution due to Hertzian contact,  $p_a$  is the pressure distribution due to adhesive forces,  $p$  is the net resultant pressure distribution.  $a$  is the contact radius,  $d$  is the length of the cohesive zone outside the region of contact where adhesive forces are supposed to act.  $c$  is  $a+d$ .  $\sigma_o$  is the cohesive zone stress assumed constant over  $d$  for a Dugdale model.

In the annulus  $a < r < c$  the surfaces separate slightly by a distance increasing from zero to  $h$ . This region is called the crack with the crack tip at the edge of the contact radius  $a$ . The surface traction distribution consists of two terms given by,

- i) The Hertz [7] pressure associated with a contact of radius  $a$ ,

$$p_1(r) = \frac{3P}{2\pi a} \left[ 1 - \left( \frac{r}{a} \right)^2 \right]^{1/2}$$

where

$$P_1 = \frac{4E^* a^3}{3R}$$

ii) The adhesive (Dugdale) stress is,

$$p_a(r) = \begin{cases} \frac{-\sigma_o}{\pi} \cos^{-1} \left( \frac{2a^2 - c^2 - r^2}{c^2 - r^2} \right), & r \leq a \\ -\sigma_o, & a \leq r \leq c \end{cases}$$

where the adhesive force is given by,

$$P_a = -2\sigma_o c^2 \left[ \cos^{-1}(a/c) - a\sqrt{c^2 - a^2} \right]$$

The next section will discuss the shape of the crack in more detail.

### 3.1.2 The Dugdale-Barenblatt crack

It has been shown, both experimentally and theoretically, that attractive forces between mica surfaces vary with separation  $z$  according to  $\sigma_o \propto z^{-3}$ , suggesting that the forces between rubber and glass may be of the same form [8]. There is also present a short-range repulsive force, which is independent of distance and therefore the force-separation curve looks like the Lennard-Jones potential in Fig. 3.1.2. There are both mathematical and conceptual problem is fitting this type of a model. An easier model is the Dugdale model according to which  $W = \sigma_o h_o$ . Schapery [10], extended the Barenblatt analysis by combining the effects of applied load and the surface forces to obtain the crack shape given by,

$$h(x) = \frac{2}{\pi E^*} \int_0^\infty \sigma_s(x') \left[ 2\sqrt{\frac{x}{x'}} - \ln \left| \frac{\sqrt{x} + \sqrt{x'}}{\sqrt{x} - \sqrt{x'}} \right| \right]^{1/2} dx \quad (2)$$

where  $x'$  is zero at the crack tip. By solving equation (2) with the force separation law,

$$\sigma_s = 0 \quad \text{for} \quad x' < 0 \quad \sigma_s = \sigma_o \left( 1 + \frac{x'}{z_o} \right) \quad \text{for} \quad x' > 0$$

This is a more realistic potential. Due to mathematical complexities arising from trying to solve the resulting integral, the Dugdale potential is usually adopted.

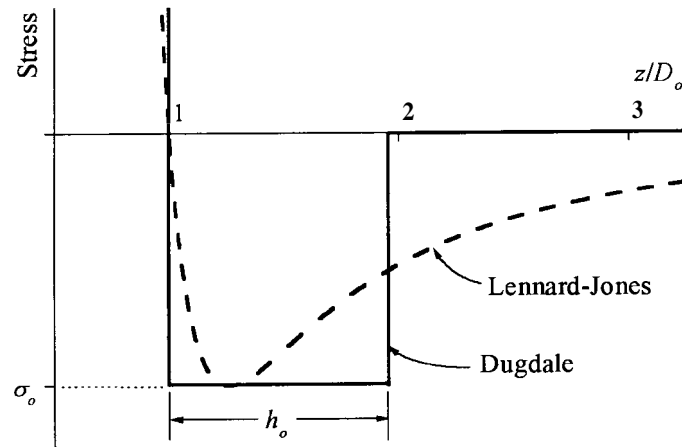


Fig. 3.2 The interaction potential. Both Lennard-Jones potential and a Dugdale potential are shown for comparison

The exact shape of the crack can be found. The initial variation with separation is  $x^{3/2}$ , which then quickly reverts to  $x$  at larger separations. A measure of the length of the crack,  $L$ , is the distance at which the stress falls to about one-eighth of its maximum value at the crack tip. This leads to,

$$L = E'h, / \sigma_o = E^* h_o^2 / 2W$$

For soft elastomers,  $W \cong 50 \text{ mJm}^{-2}$ ,  $h_o \cong 0.3\text{-}0.5 \text{ nm}$  and for  $E \cong 5 \text{ MPa}$  and for equilibrium conditions,  $\sigma_o = 100 \text{ MPa}$ . This result goes to show that,  $L \ll z_o$ , and that, for such materials, the bodies deform to a shape very close to that predicted by the JKR theory which will be discussed below from a fracture mechanics standpoint.

### 3.1.3 Griffith crack propagation criteria

In this section we will first introduce the Griffith's crack propagation criteria, followed by a fracture mechanics approach to the JKR formalism. Then we will discuss the limitations of this elastic "crack propagation criteria", while evaluating the fracture behavior of viscoelastic materials. Starting from the Barenblatt's [113] definition of the "stress intensity factor" at the crack tip, we have,

$$N = \lim_{x \rightarrow 0} (\sigma(x) \sqrt{x})$$

where  $x$  is the distance ahead of the crack tip and  $\sigma(x)$  is the stress in the solid normal to the plane of the crack.  $N$  is related to the stress intensity factor. The more common definition of the stress intensity factor,  $K_I$ , was introduced by Irwin. According to his suggestion  $N$  is related to  $K_I$ , by,

$$N = K_I \sqrt{2\pi}$$

Griffith [12] showed that the critical value of stress intensity factor at which a crack in a linear elastic solid will extend one crack length is given by,

$$K_{Ic} = \sqrt{2WE^*}$$

The theory of elasticity shows that when an elastic sphere is in contact with a plane, the pressure distribution is given by [13],

$$p(r) = \frac{2E^*}{\pi R} \sqrt{a^2 - r^2} - \frac{C}{\sqrt{a^2 - r^2}}$$

where  $a$  is the contact radius. The first term represents the pressure needed to deform the body into an appropriately matching curvature and the second term represents an arbitrary rigid body displacement given by  $\delta = -\pi C/E^*$ . The stress intensity factor at  $r = a$  is then,  $-C/(2a)^{1/2}$ . So from the equation above we have,  $C = (2E^* Wa/\pi)^{1/2}$ . Substituting this value of  $C$  into equation above and then integrating over the entire contact length gives the conventional JKR result,

$$P = \frac{4E^* a^3}{3R} - \sqrt{8\pi W E^* a^3}$$

The use of fundamental equations of fracture mechanics eliminates complications arising due to the total energy minimization concepts of a sphere on plane system as originally used by JKR. Moreover, this method can be readily applied to any contact geometry using the method of Maugis [14].

### 3.1.4 Rice's J-Integral

An alternative to the Barenblatt's cohesive zone model for evaluating the energy release rate at the crack tip is the Rice's J-integral [15]. This integral is essentially a line integral, which has the same value for all paths surrounding the tip of a notch in the two-dimensional strain field of an elastic or elastic-plastic material. The J-integral is defined as,

$$J = \int_{\Gamma} \left( \varepsilon dy - \vec{T} \frac{\partial \vec{u}}{\partial x} ds \right)$$

Where  $\varepsilon$  is the strain energy density,  $\Gamma$  is the curve surrounding the crack tip,  $\vec{T}$  is the traction vector,  $\vec{u}$  is the displacement vector and  $ds$  is an element of arc length along  $\Gamma$ .  $\Gamma$  can be any arbitrary path, independent of singularities, surrounding the crack from its upper to lower surface. Rice demonstrated that the integral is independent of the path, therefore,  $J_{\Gamma_1} = J_{\Gamma_2}$  and they both exactly vanish.

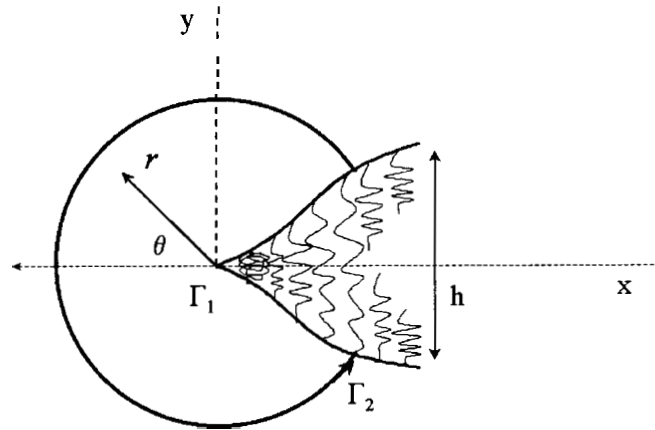


Fig. 3.3 The crack tip process zone. The interfacial chains stretch before they finally start breaking.

This is same as the Griffith's crack propagation criteria.  $J$  may also be evaluated by employing path independence to shrink the contour  $\Gamma$  down to the lower and upper surfaces of the cohesive zone as shown in Fig. 3.1.3. Then since  $dy$  is zero, we have

$$J = \oint \left( -T \frac{\partial \vec{u}}{\partial x} ds \right) = \int_{\delta_0}^{\infty} \sigma(\delta) d\delta$$

where  $\sigma(\delta)$  is the restraining stress between the two separating surface. The classical "Lake-Thomas effect" result can be arrived at by using this result. The Lake-thomas effect is essentially the amplification of the fracture energy by increasing the number of bonds per unit polymer chain length. This integral is useful in wide variety of strain-concentration problems and does so by bypassing the details of the boundary value problems. This approach is also useful in studying elastic-plastic behavior through incremental stress-strain relations. In the following section the JKR method will be discussed in detail before we move to linear viscoelastic fracture mechanics.

### 3.1.5 The JKR theory of contact mechanics

Figure (a) shows the notation used to describe a rigid probe in contact with an initially flat, perfectly elastic substrate under time dependent load  $P(t)$ .  $P(t)$  is perpendicular to the substrate surface. Cylindrical coordinates  $(r,z)$  are used with positive  $z$  into the substrate. The radius of the circular contact is  $a(t)$  and the rate at which it changes is  $V = da/dt$ ;  $\delta(t)$  is the deformation along the symmetry axis. The substrate is assumed isotropic and homogeneous with effective modulus  $E^* \equiv E/(1-\nu^2)$  where  $E$  is the Young modulus and  $\nu$  is the Poisson ratio.

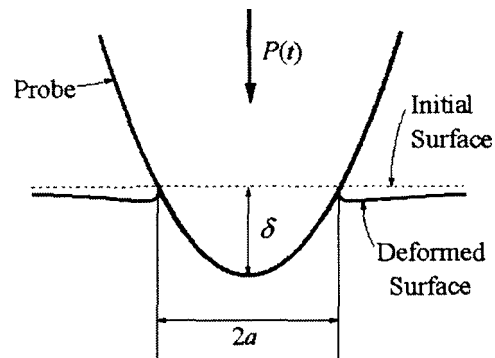


Fig. 3.4 The contact of a paraboloidal solid of revolution with a flat surface. For a Surface Force Microscopy experiment (SFM), the load,  $P$ , and contact depth,  $\delta$ , are the measured variables. Contact radius has to be calculated from  $P$  and  $\delta$ .

Equations presented in this section assume the probe is rigid and axisymmetric with parabolic profile  $f(r) = r^2/2R_o$ , where  $r$  is the radial distance from the probe axis parallel to the substrate surface.

If the potential between the probe and substrate surface is known, the case of an adhesive elastic contact can be solved using elasticity theory. However, in many situations, the interaction potential is not known *a priori* and various approximations are used. Barthel has shown that the behavior of the contact is not very sensitive to the detailed form of the potential as long as the

maximum interaction stress  $\mathbf{a}$ , and effective range of the potential  $h$ , are correct. The theoretical models discussed below use the Dugdale approximation: for  $z < D_o$ ,  $\sigma \rightarrow \infty$  where  $D_o$  is the equilibrium spacing between the probe and substrate surfaces in contact in the absence of load. In the range  $D_o \leq z \leq D_o + h$ , the stress is constant ( $\mathbf{a} = \mathbf{a}_o$ ), and  $\mathbf{a} = 0$  at  $z > D_o + h_o$ .

Dugdale and Lennard-Jones potentials are compared in Fig. 3.1.2.

In this thesis, we are interested in the limit of compliant materials ( $A \gg 5$ ) where the solution is given by Johnson, Kendall, and Roberts (JKR). For this case,

$$P = \frac{4E^* a^3}{3R} - \sqrt{8\pi W E^* a^3} \quad (1)$$

and

$$\delta = \frac{a^2}{R} - \sqrt{\frac{8\pi W a}{3E^*}}. \quad (2)$$

In many cases, however, the potential is not known. This situation is usually treated using the concepts of fracture mechanics. The periphery of the contact is viewed as the tip of a crack. If  $a$  increases, the crack closes, if  $a$  decreases, the crack opens. The crack propagates with speed  $V = da/dt$ . We use a sign convention opposite of that in the fracture mechanics literature, e.g., we take the speed of a closing crack as positive. The energy flow to the crack tip per unit area of crack extension is given by

$$G = \frac{K_I^2}{2E^*} \quad (3)$$

where the parameter  $K_I$  is called the mode one stress intensity factor.  $K_I$  is related to the potential acting between the surfaces of the crack by

$$K_I = \sqrt{\frac{2}{\pi}} \int_0^l \sigma(x) / \sqrt{x} dx. \quad (4)$$

where  $L$  is the crack length, i.e., the distance away from the crack tip over which the potential acts. In the Dugdale model,  $L$  is the distance from the crack tip at which the crack surfaces attain separation  $h_0$ . Since elastic materials have no energy dissipation in the bulk,  $G = W$  at equilibrium. If  $G > W$ , the crack advances and  $a$  decreases. If  $G < W$ , the crack recedes and  $a$  increases. In an elastic contact mechanics experiment,  $K_I$  and  $W$  contain equivalent information about the interaction potential.

### 3.2 Linear Viscoelastic Fracture Mechanics (LVEFM)

Contacts involving viscoelastic materials are more difficult to analyze because not all of the applied energy instantaneously reaches the crack tip. This has the consequence that, in contrast to elastic materials,  $K_I$  depends on the history of the contact and on the details of the crack opening and closing process. Consequently,  $a$  and  $S$  are no longer unique functions of the instantaneous load.

The analysis of viscoelastic cracks has been carried out in a series of four papers by Schapery [10,16,17,18]. Figure 3.2.1 shows the model used for the crack tip.

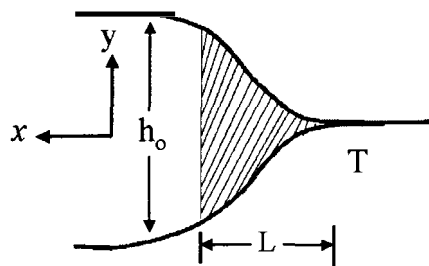


Fig. 3.5 The crack tip zone.

A small region in the immediate vicinity of the contact is referred to as the crack or the *failure* zone. The line defined by the crack tip  $T$  is assumed to lie in a plane. The curvature of the crack

in this plane is assumed small compared to the crack length  $L$ . Additionally,  $L \ll a$ . The failure zone size just behind  $T$  is characterized by  $L$  and height,  $h_{,,}$ . Outside this zone, the material is assumed isotropic, homogeneous, non-aging, and linear viscoelastic with creep compliance function  $C(t)$ . Roughness of the contacting surfaces must not occur on a length scale comparable to  $L$ , but is allowed at much longer or much shorter scales. No limitations are placed on the material inside the zone. It may be highly nonlinear, viscoelastic, and discontinuous as in the case of crazing. The stresses on the surrounding material are assumed perpendicular to the plane of the crack (Mode I).

Schapery derives an expression for  $V$  for the case where  $\sigma$  is approximated by a Dugdale model. The rate of energy flow to the crack tip is

$$G(t) = \frac{1}{2} C(t) K_I^2(t) \quad (5)$$

Equation (5) is similar to the elastic crack propagation criterion except that the time-dependent  $C(t)$  replaces the constant  $E^*$ , thereby, making  $G$  a dynamic quantity. In the short time limit,  $C(t \rightarrow 0) \rightarrow C_0 = 1/E_0^*$ , where  $E_0^*$  is the instantaneous effective modulus. In the long time limit,  $C(t \rightarrow \infty) \rightarrow C_\infty = 1/E_\infty^*$  where  $E_\infty^*$  is the long time effective modulus.

In analytical results, Schapery usually assumes that  $C(t)$  can be approximated as a power law over the time interval of interest;

$$C(t) = C_0 + C_1 t^n \quad (6)$$

where  $C_0$ , and  $C_1$  are constants and  $n$  is determined from the slope of a double logarithmic plot of  $C(t)$  in the time interval of interest. It should be noted that in section 3.2.2 the compliance is given by,

$$\phi(t) = \phi_0 + \phi_1 t^m$$

which is of the same form except for the symbols. For most polymers,  $0 \leq n \leq 0.5$ . The time for the crack to propagate distance  $L$  is

$$\tau_{crack} = g(n)^{1/n} \frac{L}{V} \quad (7)$$

where  $g(n)^{1/n}$  is a slowly varying function of  $n$  in the range 0.278 – 0.347. Following Schapery, we use  $g(n)^{1/n} = 1/3$ , so that  $\tau_{crack} = L/3V$ . The physical requirement that the stress at the crack tip be finite leads to a relationship between stress intensity factor and the crack length  $L$

$$L \approx \frac{\pi}{2} \left( \frac{K_I}{\sigma_o I_1} \right) \quad (8)$$

where  $I_1$  is a dimensionless integral given by,

$$I_1 \approx \int_0^1 f(L\eta) \eta^{-1/2} d\eta$$

where  $\eta = x/L$ . Equation (4) can be rewritten as  $L = \frac{d_o}{E_\infty C(\tau_{crack})}$ , where

$$d_o = \frac{\pi E_\infty^* h_o^2}{4 W} \quad (9)$$

is the crack length in the elastic limit and the constant  $I_1 < 2$  if the stress distribution in the cohesive zone is constant. The dependence of crack velocity on stress intensity is given by

$$V(t) = \frac{da}{dt} = \frac{\pi}{2} \left( \frac{K_I}{\sigma_o I_1} \right)^2 \left[ \frac{\lambda_n C_1}{C(t) (1 - K_I^2/K_{Ig}^2)} \right]^{1/n} \quad (10)$$

where  $K_{Ig}$  is the stress intensity factor in the glassy limit ( $t \rightarrow 0$ ) corresponding to the glass modulus,  $1/C_o$ . This result clearly illustrates that the relation between stress intensity factor and crack tip velocity is specific for a material compliance function.

Since  $G$  is a function of crack speed  $V$  and  $G \rightarrow W$  in the limit  $V \rightarrow 0$ ,

$$G(V) = W \beta(V) \quad (11)$$

where  $\beta(V)$  is greater than unity for an opening crack and less than unity for a closing crack.

Following Schapery, Johnson [19] showed that, for a closing crack,

$$\beta_{cl} \cong E_\infty C(\tau_{crack}) < 1 \quad (12)$$

and, for an opening crack,

$$\beta_{op} \cong \frac{1}{E_{\infty} C(\tau_{crack})} \gg 1. \quad (13)$$

Note that equations. (8),( 12) and (13) use  $E_{\infty}$  and not  $E_{\infty}^*$ .

### 3.2.1 Johnson's Crack tip creep theory

Johnson [19] uses the Schapery results to extend the JKR theory of adhesive contacts to the case of linear viscoelastic materials. He implicitly assumes that the loading is slow enough that material outside the crack failure zone is completely relaxed, i.e.,  $\tau_{crack}$  is long compared to the characteristic relaxation time of the viscoelastic material. He determines  $\tau_{crack}$  by eliminating  $L$  from equations (7) and (8). Substituting  $\tau_{crack}$  into equations (12) and (13) yields  $\beta_{op}$  and  $\beta_{cl}$  as functions of crack speed.

In the elastic JKR theory, the pressure acting on the contact consists of two parts. One is the Hertz pressure due to the compressive load and is distributed smoothly over the entire contact. The other is due to the adhesive interaction and is most important at the contact periphery, For viscoelastic materials, surface energy  $W$  is replaced by its scaled value  $W\beta(V)$  in the equations, so that the expression for the net contact force, becomes

$$\bar{P} = \bar{a}^3 - \sqrt{2\beta\bar{a}^3} \quad (14)$$

where reduced units  $\bar{P} \equiv P/6\pi RW$  and  $\bar{a} \equiv a/(9\pi R^2 W/2E_{\infty}^*)^{1/3}$  have been used. For the

case of constant loading or unloading rates ( $|d\bar{P}/dt| = \bar{P}_o/t_o$ ), differentiating equation (14) with

respect to  $\bar{a}$  leads to a differential equation

$$\frac{d\beta}{d\bar{a}} = 3\sqrt{2\bar{a}\beta} - 3\left(\frac{\beta}{\bar{a}}\right) - \sqrt{\frac{2\beta}{\bar{a}^3}} AC(\tau_{crack})\tau_{crack} \quad (15)$$

where  $A = (\bar{P}_o/t_o)(36RE_{\infty}^*W^2/\pi h_o^3)^{2/3}$ . Equations (7), (8), (12) and (15) can be solved

simultaneously by numerical integration to find the variation of  $\beta_{cl}$  with  $\bar{a}$ . The initial condition

for the loading cycle is given by  $\beta_{cl} = j$  when  $\bar{a} = 0^-$ . Here for most cases,  $0.9 < j < 1.0$ .

Equations (7), (8), (13) and (15) yield the variation of  $\beta_{op}$  with  $\bar{a}$ . For the unloading portion, the initial condition is given by  $\beta_{op} = j$  when  $\bar{a} = \bar{a}_{max}$ , the contact radius reached at the end of the loading cycle.

Unlike the case of macroscopic contacts, it is usually not possible to measure the contact radius directly in Scanning Probe Microscopy (SPM) or nanoindentation experiments. Therefore, the relationship between contact depth and contact radius is a crucial one if Johnson extended JKR model is to be compared directly with experimental data. Following Hui, Baney and Kramer, the contact depth at any instant  $t$  can be calculated once the contact radius is known

$$\delta(t) = \frac{a(t)^2}{R} - \sqrt{2\pi a(t)G(t)C(t)} \quad (16)$$

where  $G(t)$  is given by equation (5).

### 3.2.2 The Hui, Baney, Kramer theory for bonding, ( $\dot{a} \geq 0$ )

In this section, we describe the HBK model [20] to analyze the bonding phase of the cyclic test data. Their analysis assumes the probe is a paraboloid [ $f(r) = r^2/2R$ ] but their results are easily extended to other axisymmetric shapes. The substrate is assumed to be a linear viscoelastic material whose mechanical response is described by a creep compliance function  $C(t)$  with  $C(0) = C_o$  and a stress relaxation function  $\psi(t)$  with  $\psi(0) = \psi_o$ . These functions are assumed unchanged from their bulk values near the surface. The periphery of the contact is described as the tip of a closing crack. HBK assume the cohesive zone at the crack tip must be finite in extent, that stresses are finite everywhere, and the rate of energy flow into the cohesive zone is dependent on the crack speed,  $\dot{a}(t) = da/dt$ . Following the usual approach of fracture mechanics, the energy flow is parameterized in terms of a Mode I stress intensity factor  $K_I$ .  $K_I$  is

a measure of the magnitude of the stress field at the crack tip. In general,  $K_I$  depends on the compliance function, the geometry of the contact, the load, and the displacement. Unlike elastic materials for which  $K$  is a constant, the stress intensity factor for a viscoelastic material will in general be a functional of the time, the displacement, and the speed of displacement,

$$K_I[\dot{h}(t), h(t), t].$$

For axisymmetric contacting surfaces with parabolic profiles, the contact area and deformation are given by, (note:  $C(t) = C_o + C_1 t^n = \phi(t) = \phi_o + \phi_1 t^n$ )

$$a^3(t) = \frac{3R}{4} \left\{ \frac{3R\pi\phi_o^2 K_I^2(t)}{2} + \phi(t) * P(t) + \phi_o K_I(t) \sqrt{\left[ \frac{3\pi R\phi_o K_I(t)}{2} \right]^2 + 3\pi R[\phi(t) * P(t)]} \right\} \quad (17)$$

and

$$h(t) = \frac{a^2(t)}{R} - \frac{K_I(t) \sqrt{\pi a(t)}}{\psi_o} \quad (18)$$

where \* represents an integral operator, e.g.,  $\phi(t) * P(t) = \int_0^t \phi(t-\tau) \frac{\partial P(\tau)}{\partial \tau} d\tau$ . As

discussed by Ting [10], equations (17) and (18) are valid only if  $\dot{h}(t) > 0$ . The speed of the crack is determined using Schapery's solution for a closing crack, i.e.  $\dot{h}(t) > 0$ . In this model, the cohesive forces acting between the surfaces are approximated using a Dugdale potential with range  $h_o$ , stress per unit area of  $\sigma_o$ , and work of adhesion  $W = \sigma_o h_o$ . The crack speed is given by

$$\dot{h}(t) = \frac{\pi h_o^2 K_I^2(t)}{8W^2} \left[ \frac{\phi_1}{\phi_o \lambda(K_I)} \sqrt{\frac{\pi}{4}} \frac{\Gamma(m+1)}{\Gamma(m+3/2)} \right]^{\frac{1}{m}} \frac{1}{[1 + \lambda(K_I)]^2} \quad (15)$$

with

$$\frac{2m+1}{4W(m+1)} \phi_o K_I^2(t) \left\{ \frac{8Wm(m+1)}{\phi_o K_I^2(t)(2m+1)} \right\}^{-1} \quad (16)$$

where  $\Gamma(m)$  is the gamma function .

Schapery showed that only the behavior of  $\phi(t)$  near  $t \approx L/\phi(t)$  is important, where  $L$  is the crack length, defined as the distance from the crack tip at which the crack width becomes equal to  $h$ . For times near  $t \approx L/\phi(t)$ ,  $\phi_1$  and  $m$  can be calculated from the measured creep compliance using a method described by Schapery.

For a load controlled experiment,  $P(t)$  is specified and the above equations are solved simultaneously to obtain the time variation of  $a$  and  $h$ . In a creep test,  $P(t) = 0$  if  $t < 0$  and  $P(t) = P_o$  if  $t \geq 0$ , where  $P_o$  is constant. For this case, HBK show that

$$K_I = \sqrt{\frac{1}{4\pi\phi_o^2 a^3(t)} \left[ \frac{4a^2(t)}{3R} - \phi(t) * P(t) \right]} \quad (19)$$

The displacement  $h(t)$  is determined from equation (18) using the value of  $a(t)$  obtained by numerical solution of the differential equation

$$\frac{da(t)}{dt} = \frac{\pi^{3/2} h_o^2 \phi_1^{1/m} \Gamma(m+1)}{4W^2 \phi_o^{1/m} \Gamma(m+3/2)} \frac{K_I^2}{\left[ 1 + \lambda \left( \frac{\phi_o K_I^2}{2W} \right) \right]^2 \left[ \lambda \left( \frac{\phi_o K_I^2}{2W} \right) \right]^{1/m}}. \quad (20)$$

The solution requires some care since equation (20) diverges at  $t = 0$ .

These results of the HBK model can be used to fit the loading phase. In our analysis of small contacts, we focus on  $h$  rather than  $a$  because  $h$  is a directly measurable quantity whereas  $a$  is not. Equivalent expressions to equations (17)-(20) for a conical indenter (or any other axisymmetric probe) are straightforward to derive using the approach of Maugis.  $W$  was determined from the displacement vs. load data as described below. The stress per unit area of  $\sigma_o = W/h_o$  was estimated using an effective interaction range  $h_c = 0.5$  nm.

For an elastic substrate and a parabolic or spherical probe, it is well-known that the maximum tensile load (usually called the pull-off force) depends on the thermodynamic work of adhesion  $W$ , and the radius of curvature of probe, but is independent of the modulus. In contrast, the maximum tensile load for viscoelastic materials is strongly influenced by the rate of loading and unloading.

### 3.2.3 The Lin, Hui, Baney theory for debonding ( $\dot{a} \leq 0$ )

During the debonding phase the contact radius is being attained for the second time. In other words the contact the contact area at time  $t_u$  is the same as that at time  $t_l$ . Here  $t_l$  is some time during the bonding phase and  $t_u$  is the time during the debonding phase corresponding to same contact area as  $t_l$ . So in Fig 3.2.2,  $t_l < t_m$  and  $t_u \geq t_m$ . The time  $t_u$  is determined during the unloading phase and is given by the condition,

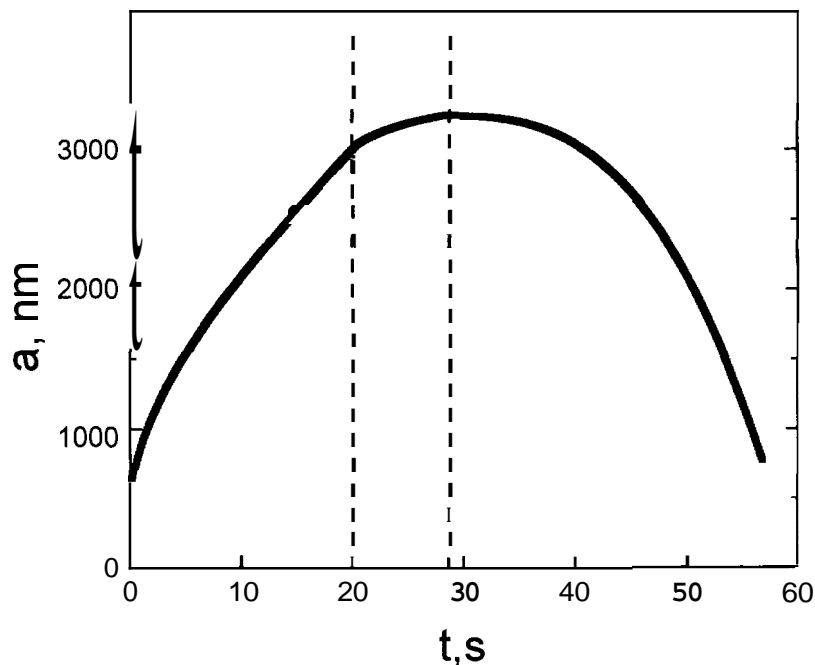


Fig. 3.6 Contact radius for an entire loading-unloading cycle

$$a(t_u) = a(t_l) \quad \text{where } t_u \geq t_m \text{ and } t_l < t_m \quad (20)$$

The functional form of  $a(t_l)$  must be known *a priori* and then  $t_u$  can be obtained by solving the above equation numerically. One must observe that while the function  $a(t_u)$  is defined in the

interval  $t \geq t_m$ , it assumes values in the interval  $t \in [t_m, t_f]$ . A new function,  $t_f(t)$ , was then defined as,

$$t_f(t) \equiv \begin{cases} t_f & \text{when } t < t_m \\ t & \text{when } t \geq t_m \end{cases} \quad (21)$$

For a load controlled test the stress intensity factor  $K_I(t)$  for  $t \geq t_m$  is given by [21],

$$K_I(t) = E(t - t_f(t)) C_o K_I(t_f(t)) - \frac{E(0)}{2\sqrt{\pi a(t)^{3/2}}} \int_{t_{\max}}^t C(t - \tau) d \left[ F(\tau) - \int_{0^-}^{\tau} E(\tau - \theta) dg(\theta) \right]$$

$$\text{where } g(\theta) = \int_{0^-}^{\theta} C(\theta - \xi) dF(\xi) \quad (22)$$

It should be noted that this expression is independent of contact geometry. The material compliance function is given by the form,  $C(t) = C_o + C_1 t^n$  and the corresponding relaxation function,  $E(t)$  is determined by the equation,

$$E(t) = L^{-1} \left[ \frac{1}{s^2 L[C(t)]} \right] \quad (23)$$

where  $L$  is the Laplace transform. Since computing the relaxation function of the above creep compliance is analytically challenging we use a simple alternative. If the slope of the double logarithmic plot of modulus and time is approximately a constant,  $m$ , then the relaxation function can be approximated by [22],

$$E(t) = \frac{\sin(m\pi)}{m\pi C(t)} \quad (24)$$

which is shown to give reasonable results. The loading function is linear, i.e.,  $P(\xi) = \frac{P_o}{t_o} \xi$ ,

where  $P_o$  and  $t_o$  are the maximum load and loading time respectively. The data consists of entire time histories of contact depth and applied load  $P(\xi)$ . The first term in equation [22] above is

completely determined from the loading phase data. HBKL [21] assume a functional form for the contact radius during the unloading cycle, which exactly satisfies the unloading displacement data. The functional form used to describe the unloading contact radius is give by,

$$a(t_u) = a_{\max} - At,^3 - Bt,^2$$

where  $a,$  is the maximum contact radius and A and B are arbitrary constants. The relationship between the contact radius and contact depth is given by,

$$\delta(t_u) = \frac{a(t_u)^2}{R} - \sqrt{\frac{2\pi W a(t_u)}{E(t_u)}} \quad (25)$$

where  $E(t_u)$  is the relaxation function of the material. The second term is more complex and requires the evaluation of a triple convolution integral. The innermost integral, which is given by  $g(\theta)$ , is evaluated only in the interval  $[0, t_u]$  and requires data from the bonding phase of the experiment. After evaluating this first convolution the complete second term now is,

$$\frac{E(0)}{2\sqrt{\pi}a(t)^{3/2}} \int_{t_{\max}}^t C(t-\tau) d \left[ F(\tau) - \int_{0^-}^{t_f(\tau)} E(\tau-\theta) C(\theta) \frac{P_o}{t_o} \right] \quad (26)$$

this can be simplified and written as,

$$\frac{E(0)}{2\sqrt{\pi}a(t)^{3/2}} \int_{t_{\max}}^t C(t-\tau) \left[ \frac{dF(\tau)}{d\tau} - \frac{d}{d\tau} \int_{0^-}^{t_f(\tau)} E(\tau-\theta) C(\theta) \frac{P_o}{t_o} \right] d\tau \quad (27)$$

The second convolution is a function of  $\tau$  evaluated in the interval  $[t_{\max}, t]$ . This can be further simplified and written as,

$$\frac{E(0)}{2\sqrt{\pi}a(t)^{3/2}} \int_{t_{\max}}^t C(t-\tau) \left[ \frac{dF(\tau)}{d\tau} - \frac{P_o}{t_o} E(0) C(\tau) d\tau + \frac{P_o}{t_o} E(\tau) C(0) d\tau \right] \quad (28)$$

Therefore, we are now reduced to a single integral which is evaluated during the unloading or debonding portion. The first term of this integral is simple to evaluate. The first integral term will

be negative since the load is decreasing with time therefore  $P(\xi) = \frac{P_o}{t_o} \xi$ . We will discuss the

second and third term. The second term can be written as,

$$-\frac{E(0)^2}{2\sqrt{\pi}a(t)^{3/2}} \frac{P_o}{t_o} \int_{t_{\max}}^t C(t-\tau)C(\tau)d\tau \quad (29)$$

For a standard solid these integrals are simple to evaluate but if the material compliance function

is given by the form  $C(t) = C_0 + C_1 t^n$ , the key term in the evaluation of the above integral is

$$-\frac{E(0)^2 C_1^2}{2\sqrt{\pi}a(t)^{3/2}} \frac{P_o}{t_o} \int_{t_{\max}}^t (t-\tau)^n \tau^n d\tau \quad (30)$$

As long as  $n < 1$  and  $\left(\frac{\tau}{t}\right)^2 < 1$ , a series expansion method can be used to evaluate this integral.

Only the first two terms in the expansion are considered and therefore this solution is a second order approximation. The expanded form of the integral is approximately given by,

$$\int_{t_{\max}}^t t^n \tau^n \left[ 1 - n \left(\frac{\tau}{t}\right) + \frac{n(n-1)}{2!} \left(\frac{\tau}{t}\right)^2 \right] d\tau \quad (31)$$

The third term is interesting since it uses one of the fundamental results of linear viscoelasticity which relates creep compliance,  $C(t)$ , and relaxation modulus,  $E(t)$ . The third integral term is given by,

$$\frac{E(0)^2}{2\sqrt{\pi}a(t)^{3/2}} \frac{P_o}{t_o} \int_{t_{\max}}^t C(t-\tau)E(\tau)d\tau \quad (32)$$

From linear viscoelasticity it follows that,

$$L[C(t)]L[E(t)] = \frac{1}{s^2} \quad (33)$$

Inverse Laplace transform of this equation results in

$$\int_0^t C(t-\tau)E(\tau)d\tau = t \quad (34)$$

Using the above result the third term can be simply written as

$$\frac{E(0)^2}{2\sqrt{\pi}a(t)^{3/2}} \frac{P_o}{t_o} (t-t_{\max}) \quad (35)$$

Hence it is only the second term which requires computation. All other terms can be evaluated analytically irrespective of the material compliance function. Let the second term in equation (22) be represented by  $\zeta(t)$ . Therefore, equation (22) can now be rewritten as,

$$K_I(t) = E(t-t_f(t))C_o K_I(t_f(t)) - \frac{E(0)}{2\sqrt{\pi}a(t)^{3/2}} \frac{P_o}{t_o} \zeta(t) \quad (36)$$

where  $\zeta(t)$  represents  $\int_{t_{\max}}^t C(t-\tau)[\tau - E(0)C(\tau)d\tau + E(\tau)C(0)d\tau]$  and is a negative term.

Therefore the stress intensity for the unloading cycle is always greater than that during the loading cycle with a continuity at zero crack velocity.

Rearranging equation (36) to express contact radius in terms of  $K_I(t)$ ,

$$a(t) = \left[ \frac{\frac{E(0)}{2\sqrt{\pi}} \frac{P_o}{t_o} \zeta(t)}{E(t-t_f(t))C_o K_I(t_f(t)) - K_I(t)} \right]^{2/3} \quad (37)$$

The first step in the solution is to assume a form for  $a(t)$  that exactly satisfies equation (25) above to give  $\delta(t)$ .  $K_I(t)$  can then be calculated from equation (36) above. A second approach is to assume a form for  $K_I(t)$ . This will then lead to  $a(t)$  through equation (37). This calculated  $a(t)$  should then be related to  $\delta(t)$  through equation (25).

### 3.2.4 Energy dissipation during viscous chain pullout

In this section a totally different approach to studying fracture in polymers is described. The force needed to break a bond does not have a fixed value. This value depends on the thermal state of the system and the rate of the fracture process. Energy dissipation taking place as the polymer chain extend and relax during fracture influences the energy required to rupture a bond. This is described in detail in a recent paper [23]. In this section we will discuss a possible kinetic coupling between the interfacial and bulk processes. Under the action of a constant viscous force, chains desorb from a surface according to the equation,

$$-\frac{d}{dt} \sum_b = \frac{\sum_b}{\tau} \exp\left(\frac{-\mu V \lambda}{kT}\right) \quad (38)$$

where  $\sum_b$  is the areal density of the chains in the bonded state,  $\lambda$  is the activation length of the bond,  $\tau$  is the chain relaxation time,  $V$  is the velocity,  $k$  is the boltzmann constant,  $T$  is the temperature and  $\mu$  is the viscous friction coefficient. The solution to this equation is an exponential in the bond survival time,  $t$ . The energy dissipation corresponding to detachment of a chain now shows a strong velocity dependence given by,

$$G = \mu V^2 \tau \exp\left(\frac{-\mu V \lambda}{kT}\right) \quad (39)$$

Fig. 3.2.3 show the dependence of  $G$ , normalized by its initial value, on velocity for a set of values of the interfacial parameters. It should be noted that this behavior is very similar to the stress intensity factor during debonding from experiments done on viscoelastic latexes. The results will be shown in chapter 7.

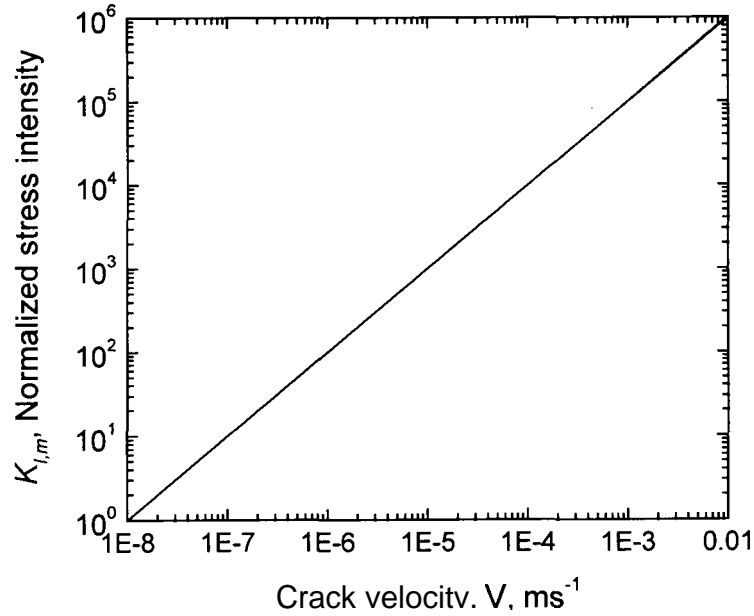


Fig. 3.7 Normalized stress intensity factor plotted as a function of crack velocity using equation (39) above. The trend in this behavior should be noted. In chapter 7 we will show that the normalized stress intensity obtained from continuum mechanics is similar to this behavior predicted by polymer chain dynamics

### 3.3 Visco-elasto-plastic deformation

For contact between large compliant elastic bodies, the JKR approach can be adopted to express the material deformation as a function of applied load. Figure 3.3.1 depicts such as contact experiment. The radius of the contacting probe is  $R$  and the contact radius is given by  $a$ . For contact mechanics to apply,  $a \ll R$ . Outside the contact zone is the cohesive zone represented by the annulus  $c$ . The asymptotic solution assumes that the adhesive traction is limited to the contact region, ( $r < a$ ), and the cohesive zone is much smaller than the contact zone. For smaller bodies, the cohesive zone plays an important role and must be taken into account. The load corresponding to an adhesive traction within the contact is given by,

$$P = 2K_I \sqrt{\pi a^3} \quad (40)$$

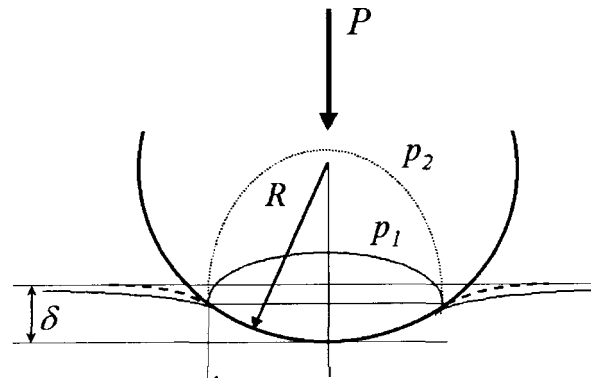


Fig. 3.8 A typical contact experiment showing a possible effect on deformation dynamics due to material plasticity. The dashed line is for a purely elastic material whereas the solid line is for an elasto-plastic material.

where  $K_I$  is the mode I stress intensity factor and  $a$  is the contact radius and  $P$  is the load corresponding to adhesive traction. At initial separation is related to the work of adhesion ( $W$ ) by the Griffith's crack propagation criteria, given by the simple Irwin's relationship,

$$W = \frac{K_I^2}{2E^*} \quad (41)$$

where  $E^*$  is the effective material elastic modulus. Under equilibrium  $G=W$ , but due to viscoelastic dissipative effects ( $G/W$ ) can be as high as the ratio between the material instantaneous and relaxed modulus [14]  $E_o / E_\infty \approx 10 - 50$ . For pure styrene butadiene latex films this ratio can be as high 1000 as reported in the experiments dealing with fracture of rubber. The JKR relation, which modifies the Hertzian contact for the contact of a rigid sphere of radius  $R$  on a flat elastic surface of modulus  $E^*$ , to account for adhesion is therefore given by,

$$P = \frac{4E^* a^3}{3R} - \sqrt{8\pi W E^* a^3} \quad (42)$$

The contact depth is related to the contact radius by the relationship given by,

$$\delta = \frac{a^2}{R} - \sqrt{\frac{2\pi W a}{E^*}} \quad (43)$$

Here  $P$  is the total load. The above two relationships can then be used to follow the elastic displacement of a contact experiment. It should be noted that this relation is valid so long as the complex stresses generated by the applied load are within the yield stress of the material. So for incipient loading this relationship is valid, but as we approach the material yield limit due to increasing contact load, plastic yield has to be accounted for by using an appropriate yield criterion. The next section deals with the onset of plastic yield after an initial elastic response.

### 3.3.1 The yield stress criterion

The load at which plastic yield begins in the complex stress field of two contacting solids is related to the yield point of the softer material in an indentation experiment through an appropriate yield criteria [24]. For most ductile materials this criteria is usually taken to be governed by either the von Mises' shear strain-energy criteria, whereby,

$$J_2 \equiv \frac{1}{6} \{ (\sigma_1 - \sigma_2)^2 + (\sigma_2 - \sigma_3)^2 + (\sigma_3 - \sigma_1)^2 \} = k^2 = \frac{\sigma_y^2}{3} \quad (44)$$

or by the Tresca's maximum shear stress criteria,

$$\max \{ |(\sigma_1 - \sigma_2)|, |(\sigma_2 - \sigma_3)|, |(\sigma_3 - \sigma_1)| \} = 2k = \sigma_y \quad (45)$$

in which  $\sigma_1$ ,  $\sigma_2$  and  $\sigma_3$  are the principal stresses in the state of complex stress and  $k$  and  $\sigma_y$  denote the values of yield stress of the material in simple shear and simple compression or tension respectively. The difference between these two criteria's is hardly significant when the anisotropy of the material is considered. Using the Tresca's criteria, the maximum shear stress in the axisymmetric contact of two solids of revolution can be calculated. The maximum shear stress occurs beneath the surface on the axis of symmetry. Along this axis  $\sigma_1$ ,  $\sigma_2$  and  $\sigma_3$  are the

principal stresses with  $\sigma_1 = \sigma_1$ . The maximum value of  $|\sigma_z - \sigma_r|$  for a poisson ratio,  $\nu$ , of 0.3 is  $0.62p_o$  at a depth of  $0.48a$ . Thus by the Tresca's criteria the value of  $p$ , for yield is given by,

$$p_o = \frac{3}{2} p_m = 3.2k = 1.6\sigma_y \quad (46)$$

Therefore for a Hertzian contact of a sphere of radius  $R$  with a flat surface, the load to initiate yield is related to the maximum contact pressure by,

$$p_o = \left( \frac{6PE^*}{\pi^3 R^2} \right)^{1/3} \quad (47)$$

Therefore, the yield criteria then becomes,

$$P_y = \left( \frac{\pi^3 R^2}{6E^{*2}} \right) p_o^3 \quad (48)$$

This equation clearly describes an important material selection criteria according to which in order to sustain high loads the material should not only have high yield strength but also a lower elastic modulus.

### 3.3.2 Regimes of deformation

The fully plastic condition is reached when  $E^* a / R \sigma_y \approx 40$  or  $P/P_y \approx 400$ . This criterion will be used for determining the transition from elastic to plastic deformation. **If** in the fully plastic regime with no pile up or sink in, the contact depth is related to the contact load by the relation,

$$\delta = 1.235 \left( \frac{P}{P_y} \right) \frac{R \sigma_y^2}{E^{*2}} \quad (49)$$

This relationship is important since it relates two key variables, applied load  $P$  and penetration depth  $\delta$ , which is measured in an indentation experiment.

### 3.3.3 Johnson's theory for evaluating material yield stress

During the unloading of a contact that has plastically yielded during loading, the initial response is elastic. Work done by Tabor et. al.[25] using a hard steel ball of radius  $R$  on a softer metal led to the observation that permanent indentation under had a radius  $R'$ , which was greater than  $R$  due to elastic compression of the ball. When the load is removed the indentation shallows to some extent due to instantaneous elastic recovery. The effective radius of curvature of this recovered crown  $R'$  can be estimated using the Hertz relationship,

$$R' = \frac{4E^* a_o}{3\pi H} = \frac{4E^* P_o^{1/2}}{3(\pi H)^{3/2}} \quad (50)$$

Since the loading stresses are much higher than the yield stress and,  $C_y \geq 800$ , complete similarity is achieved in the contact the pressure profile under the contact is nearly uniform. Therefore, the shape of the contact is not necessarily spherical but elliptic. The values of  $R'$  will therefore be substantially higher than  $R$ . The exact value of  $R'$  will, however, depend on hardness  $H$  and the maximum deforming load,  $P_o$ . Figure 4 illustrates this situation. Greater the difference between  $R$  and  $R'$ , greater is the plastic deformation. This radius of the recovered crown can now be used to model the unloading part of the indent using the JKR relationship, given by

$$P = \frac{4E^* a^3}{3R'} - \sqrt{8\pi W E^* a^3} \quad (451)$$

But since these coatings consist of approximately 25% latex the unloading response is not expected to be completely elastic-plastic.

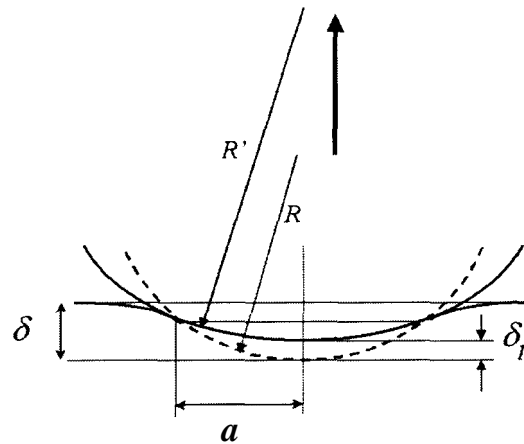


Fig. 3.9 The residual impression of a plastically deformed surface. The dashed line shows initial contact impression at maximum deformation. When the load is withdrawn, the material recovers partially leaving a residual deformation given by  $\delta_p$ . Solid line shows the final impression shape. Unloading can therefore be treated as the elastic recovery of a crown of radius  $R'$ .

Introducing pigments in a continuous latex matrix changes its mechanical properties. Coatings containing upto 75% pigment volume ratio exhibit viscoelastic behavior [26,27] and therefore dissipative effects due to the viscoelastic response of the latex will convolute the results.

Dissipative effects, especially during decohesion (debonding) part is important since they are convoluted by material plasticity and therefore separating these disparate effects is imperative for a complete analysis. Crack tip creep effects have limited effects during decohesion and in our case since  $E_o / E_\infty \approx 10 - 50$ , the dissipative effects are restricted even further. For modeling decohesion, however, we have adopted the crack tip creep approach due to Johnson. The bulk creep compliance of these materials measured by Prall [28] were used to determine the creep compliance of these pigmented coatings. Johnson's crack tip creep model is suitable for this analysis since the time frame of testing is far removed from the characteristic relaxation times of the material and therefore material creep effects will be restricted to the crack tip zone. According

to the Johnson's approach, during debonding the load vs. displacement behavior of the material should follow,

$$P = \frac{4E^* a^3}{3R'} - \sqrt{8\pi W \beta E^* a^3} \quad (52)$$

In dimensionless form this equation is given by,

$$\bar{P} = \bar{a}^3 - \sqrt{2\beta\bar{a}^3} \quad (53)$$

where reduced units  $\bar{P} \equiv P/6\pi R W$  and  $\bar{a} \equiv a/(9\pi R^2 W/2E_\infty^*)^{1/3}$  have been used. For the case of constant loading or unloading rates ( $|d\bar{P}/dt| = \bar{P}_o/t_o$ ), differentiating eqn. with respect to  $\bar{a}$  leads to a nonlinear non-homogenous differential equation,

$$\frac{d\beta}{d\bar{a}} = 3\sqrt{2\bar{a}\beta} - 3\left(\frac{\beta}{\bar{a}}\right) - \sqrt{\frac{2\beta}{\bar{a}^3}} A C(\tau_{crack}) \tau_{crack} \quad (54)$$

where  $A = (\bar{P}_o/t_o)(36RE_\infty^*W^2/\pi h_o^3)^{2/3}$  and  $\beta$  is given by

$$\beta = \frac{1}{\phi(\tau^*)} \quad (55)$$

where,  $\phi(t)$  is the material creep compliance function and  $t^*$  is the representative time for the debonding process and to a first approximation is given by Schapery's relationship,

$$\tau_* = \frac{1}{3} \left( \frac{E_\infty^* h_o^2}{WV\phi(\tau^*)} \right) \quad (56)$$

For the materials analyzed the creep compliance is given by the form

$$\phi(t) = (E_\infty + E_1 t^{-p})^{-1} \quad (57)$$

where  $E_\infty^*$  is the material relaxed modulus,  $W$  the interfacial work of adhesion,  $V$  the effective crack velocity ( $da(t)/dt$ ), and  $h$ , is an effective range parameter and is approximately  $\cong 0.5nm$ .

The equations (52) through (55) can be solved simultaneously to model the debonding portion.

The values of  $E_{\infty}$ ,  $E$ , and  $\rho$  are listed in table 2 in chapter 9. The material creep compliance was obtained from bulk rheological tests done by Katharina et. al. on a Dynamic Mechanical Thermal Analyzer (DMTA).

### 3.4 References for chapter 3

1. Landman, U., Luedtke, W. D., Burnham, N. A., Colton, R. J., *Science* 1990,248,454.
2. Carpick, R. W., Ogletree, D. F., Salmeron, M. *Appl. Phys. Lett.* 1997, 70, 1548.
3. Lantz, M. A., O'Shea, S. J., Welland, M. E., Johnson, K.L. *Phys. Rev. B* 1997, 55, 10776.
4. Hurtado, J. A., Kim, K. S. *Proc. R. Soc. Lond. A* 1999.
5. Hurtado, J. A., Kim, K. S. *Proc. R. Soc. Lond. A* 1999.
6. Maugis, D. J. *Colloid Interface Sci.* 1992, 150,243.
7. Hertz, H., Reine, J. *Agnew. Math.* 1882, 92, 156.
8. Johnson, K. L., Kendall, K., Roberts, A. D. *Proc. R. Soc. Lond. A* 1971,324,301.
9. Derjaguin, V., Muller, V. M., Toporov, Y. P. *J. Colloid Interface Sci.* 1975, 53, 3 14.
10. Schapery, R. A. *Int. J. Fracture* 1975, 11,369.
11. Irwin, J. R.J. *Appl. Mech.*, 24, 361.
12. Johnson, K. L., J. A. Greenwood *J. Colloid and Interface Sci.*, 1997, 192,326-333.
13. Barenblatt, G. I. *Adv. Appl. Mech.* 1962, 7, 55.
14. Maugis, D. *Langmuir* 1995, 11, 679.
15. Rice, J.R. *J. Appl. Mech.* 1968,7, 379.
16. Schapery, R. A. *Int. J. Fracture* 1975, 11, 141.
17. Schapery, R. A. *Intl. J. Fracture* 1975, 11, 549.
18. Schapery, R. A. *International J. Fracture* 1989, 39, 163.

19. Johnson, K. L *Microstructure and Microtribology of Polymer Surfaces*, eds. V. V. Tsukruk and K. J. Wahl, American Chemical Society, Washington, D.C., **2000**.
20. Hui, C.-Y., Baney, J. M., Kramer, E. J. *Langmuir* **1998**, **14**, **6570**.
21. Lin, Y. Y., Hui, C.-Y., Baney, J. M. *J. Phys. D: Appl. Phys.* **1999**, **32**, 2250.
22. Ferry, J. D. *Viscoelastic Properties of Polymers*, **1980**, John Wiley & Sons: New York.
23. Ghatak, A., Vorvolakos, K., She, H., Malotky, D. L., Chaudhury, M. K. *J. Phys. Chem. B*
24. K.L. Johnson, *Contact Mechanics*, Cambridge University Press, **1985**.
25. Tabor, D., *Proc. R. Soc. Lond.*, **1948**, **A192**, 247, **181**, **364**.
26. Nielsen, L.E.; *Mechanical Properties of Polymers and Composites*, Decker, New York, **1974**, vol. 2.
27. Joyce, M., Hagen, R., and de Ruvo, A., Mechanical consequences of coating penetration, *Journal of Coatings Technology*, **1997**, **69**, **869**, **53-58**.
28. Micromechanical Properties of Pigmented Coatings, A thesis by Katharina Prall, Dept. of Chemical Engineering, University of Maine, Orono, ME **04473**, **2000**.

## **PART 11: Dynamic Contacts to Viscoelastic Styrene-Butadiene Latex Films**

### **Chapter 4. Latex Film Rheological properties**

#### **4.1 Sample preparation for dynamic mechanical testing**

Dynamic mechanical properties of the latex films were determined using the parallel plate geometry of the Bohlin CVO rheometer. These latexes are in 50% hydrophobic solids dispersion in water. When exposed to their minimum film forming temperatures (MFFT), these latexes form clear films. We wanted to study the properties of these latex films. Latex films of appropriate dimensions (1 mm thick and 4 cm dia.) were made using a Teflon™ cast. These films were then loaded into the equipment geometry. The initial step was to heat the sample at least 50°C above its glass transition temperature ( $T_g$ ). This process ensured proper adhesion between the parallel plates and the sample. Heating the sample above its  $T_g$ , also relieved any residual stresses in the sample due to loading.

Small Amplitude Oscillatory strain (SAOS) tests were then performed on the sample at five different temperatures and over a range of frequencies at each temperature. The temperatures used were 5°C, 25°C, 35°C, 65°C and 80°C. Master curves for the dynamic relaxation data were then constructed using the William-Landel-Ferry [1] time-temperatures superposition principle. The shift factors were noted and have been reported in [2]. The material compliance was determined from these master curves. This data contains information about the shear modulus,  $G'$ , of latexes. The shear modulus can be converted into elastic modulus,  $E'$ , by using the Trouton's ratio of 3, assuming incompressibility ( $\nu=0.5$ ). The primary goal of this work was to also compare this bulk rheological data with the localized nano-rheological measurements done with the nanoindentation device.

## 4.2 Material creep compliance

The analysis in this section requires knowledge of the creep compliance function of the latex  $C(t)$ . We assume it to be the same as for bulk and calculate it from the measured shear modulus. To facilitate this calculation and to obtain  $C(t)$  in an analytical form more suitable for the analysis, we used the following functional form

$$C(t) = \begin{cases} \frac{1}{E_o} + At^p & t < t_o \\ \frac{1}{E_\infty + Bt^{-q}} & t > t_o \end{cases} \quad (1)$$

where  $E_o$  is the instantaneous modulus ( $E$  in the limit  $\omega \rightarrow \infty$ ),  $E_\infty$  is the relaxed modulus (limit  $\omega \rightarrow 0$ ) and  $p$  and  $A$  are constants. Constants  $B$  and  $q$  are determined using the requirement that  $C(t)$  and its first derivative be continuous at  $t_o$ . Schapery has shown that the power law dependence for  $t < t_o$  is always a good approximation for contacts involving polymers [3]. The form for  $t > t_o$  was chosen because it is simple and gives a good fit to the data. For the latexes studied here,  $E_o$  values are near 1-2 GPa and  $E_\infty$  values are in the range 0.1-0.5 MPa.  $C(t)$  was calculated directly from  $E(\omega)$  using a sequence of transformations [4] as shown below,

$$\int_0^t C(t-\tau)E(\tau)d\tau = t$$

which is the inverse Laplace Transform relation between the creep compliance and relaxation modulus. This yields  $E(\tau)$ , which is related to the acquired data,  $E(\omega)$ , by the Fourier Transform given by,

$$E(t) = \frac{2}{\pi} \int_0^\infty E(\omega) \frac{\sin(\omega t)}{\omega} d\omega$$

Constants  $p$  and  $A$  were determined by fitting this  $E(\omega)$  to the measured shear moduli assuming a Poisson ratio  $\nu = 0.5$  so that  $E = 3G$ . The resulting values are listed in Table 1. Latex **4**, how-

ever, followed a standard body creep compliance for the most part of the indentation frequency-testing regime. The compliance function of latex # 4 for  $t < 100$ s is given by,

$$C(t) = 1 - \left(1 - \frac{E_\infty}{E_o}\right) \exp\left(-\left(\frac{E_o E_\infty}{E_o - E_\infty}\right) \frac{t}{\eta}\right)$$

The instantaneous modulus,  $E_o$ , of this latex was 3.2 GPa, the relaxed modulus,  $E_\infty$  of 18 MPa and the viscous dashpot element,  $\eta$ , had a value of 2.2 GPas. This simple approximation of latex #4 as a standard solid simplifies the calculation considerably, but in section 3.2.3 we have dealt mainly with the procedures for calculation stress intensity functional for a creep compliance given by the form in equation (1).

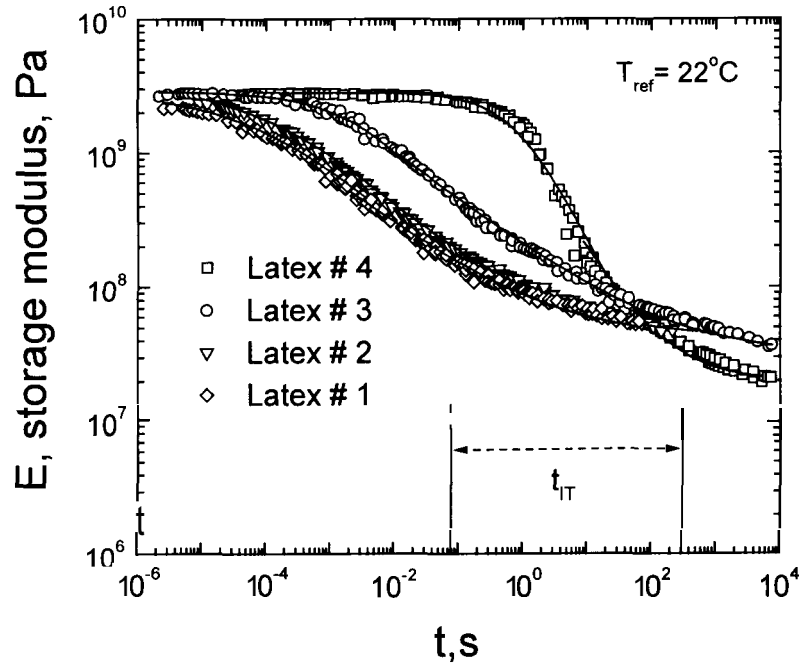


Fig. 4.1 Storage modulus of four different styrene butadiene latexes as measured in a parallel plate rheometer using small amplitude oscillatory shear experiment. The shear modulus was converted into elastic modulus using the Trouton's ratio assuming incompressibility. The time frame accessible to indentation testing is indicated by  $t_{IT}$ .

The time corresponding to the response times of the indenter is indicated in the figure 4.1 as  $t_{IT}$ .

Indentation is sensitive to the rheological response of the sample within this frequency interval.

The resonant frequency of the indenter is close to 120 Hz and therefore tests done close to this frequency contain effects due to indenter inertia. Long time tests done over a time of 1000s were affected by indenter drift.

Latex	$E_o$ (MPa)	$E_\infty$ (MPa)	$P$	$M$ ( $s^P$ /MPa),	$t_o$ (s)
1	1600	24	<b>0.45</b>	0.04	0.0 1
2	1650	<b>25</b>	0.45	0.035	0.0 1
3	2600	16	0.5	0.003	<b>0.1</b>

Table 4.1. Parameters of the material compliance functions

Latex film rheological properties are sensitive to the glass transition temperature ( $T_g$ ) alone. Latex 1 is the best film forming latex with a smallest particle size. Latex 2 had a particle size almost twice that of latex 1. Both latex 1 and 2 contain the same total acid functionality. Latex 3 contains acrylates along with the acids. Latex 1, 2 and 3 are all crosslinked internally with a chain transfer agent used during emulsion polymerization. Latex 4 is styrene-acrylate with a very low degree of crosslinking.

#### 4.3 References for Chapter 4

1. Ferry, J. D. *Viscoelastic Properties of Polymers*, **1980**, John Wiley & Sons: New York.
1. Giri, M., Unertl, W. N., D. W. "Dynamic Contacts to Adhesive Viscoelastic Materials: Work of Adhesion," *Langmuir*, **2001**, in press.
2. Schapery, R. A. *International J. Fracture* **1989**, *39*, **163**.
3. Findley, W. N., Lai, J. S., Onaran, K. *Creep and Relaxation of Nonlinear Viscoelastic Materials* (Dover, Mineola, N.Y., **1989**).

## Chapter 5. Low Loading Rate Contacts to SB Latex films

### 5.1 Introduction

Mechanical contacts between elastic materials with nanometer to micrometer dimensions are well understood, including the increasingly important role of adhesion as the contact size decreases [1,3]. For elastic materials, the contact radius  $a$  and penetration  $\delta$  are uniquely determined by the applied load  $P(t)$ , the elastic properties of the contacting materials, and the thermodynamic work of adhesion  $W$ . Fits of  $a$  vs.  $P$  or  $S$  vs.  $P$  data to the appropriate theoretical models allows  $W$  and the effective moduli of the contacting materials to be determined. Contacts involving elastomers are less well understood but approximate models are available that allow estimates of  $W$  and mechanical properties [1,3].

In contrast, contacts to viscoelastic materials are poorly understood [4]. There is very little quantitative data and, until quite recently, there were no theoretical models including both viscoelastic response and adhesion. In this paper, we present a detailed experimental study of micrometer-sized contacts between a rigid probe (diamond) and three viscoelastic materials (Styrene-Butadiene latexes). A preliminary report has been published [4]. These results are analyzed using two new models. In this paper, we show that, at low loading rates, an approximate model due to Johnson [5] provides a robust method to determine  $W$  and the effective range of the potential. In a subsequent chapter, we show that the data can be fit at all loading rates using a theory developed by Hui and co-workers [6,7].

### 5.2 Experimental Details

The polymers studied were films cast from aqueous hydrophobic suspensions of carboxylated styrene/butadiene copolymer latexes (provided by Omnova Solutions Inc., Performance Chemicals Division, Akron, OH). Three latexes were studied. Their properties are summarized

in Table 5.1. They differed in their glass transition temperatures, particle size and degree of crosslinking. The glass transition temperatures,  $T_g$ , were 5 °C for latex 1 and latex 2 and 20 °C for latex 3 as determined with a DSC. Latex 4 is a styrene-acrylate latex with a low degree of crosslinking with a  $T_g$  of 28°C and was provided by BASF. Latex 1 and latex 2 differed primarily in their particle size crosslinking with latex 2 having a larger size.

Latex	Styrene-butadiene ratio	Degree of internal crosslinking	Diameter (nm) from CHDF	$T_g$ (°C) from DSC
1	3:2	medium	130	0
2	3:2	medium	190	0
3	4:2	high	190	20

Table 5.1. Styrene-Butadiene/Acrylate Latex Properties

Latex 3 had the highest degree of crosslinking. Film samples were prepared by depositing the latex suspension on Mylar, drying in ambient air, heating for about 1 hr to about 50 °C above  $T_g$ , and then washing with deionized water. All samples were tested within 2 days of preparation. The final thickness of these films was 0.1-0.2 mm. The root-mean-square roughness of the films, as measured with contact mode atomic force microscopy (AFM), was typically 10 nm over areas of several square micrometers. AFM images typically show evidence of residual particle structure since the crosslinked parts of the original latex particles remain intact during film formation. Crosslinking hinders the film formation under ambient conditions since crosslinking reduces the melt flow. This introduces some heterogeneity into the samples and is responsible for most of the intrinsic surface roughness. It is also probably the major cause of variation in the contact properties from point to point on the surfaces.

Contacts were made with diamond probes in a nanomechanical testing system (Hysitron PicoIndenter mounted on a Park Scientific Instruments CP scan base). Two probe shapes were used: Berkovich and a 10  $\mu\text{m}$  diameter spherical tip. An ideal Berkovich indenter is a triangular pyramid whose cross sectional area increases as  $A(h) = 24h^2$  with distance  $h$  from the tip, but the actual indenter is rounded at the tip. The effective radius was estimated to be  $R \approx 200$  nm by assuming a spherical end shape and fitting the  $A(h)$  data for small values of  $h$ . All data have been corrected for the 159 N/m stiffness of the support springs. Contacts were controlled with a predetermined loading/unloading cycle  $P(t)$ . The displacement (also called deformation or depth of penetration)  $\delta(t)$  of the rigid probe was measured continuously during the contact cycle. Thermal drift of about 0.05 nm/s limited measurements times to a few hundred seconds.

Figure 5 shows a result of typical cyclical loading-unloading experiments. Fig. 5.1(a) shows load and displacement vs. time for a high loading rate of 2.5 N/s and Fig 5.1 (b) shows displacement vs. load for a much lower loading rate of 0.8 mN/s.

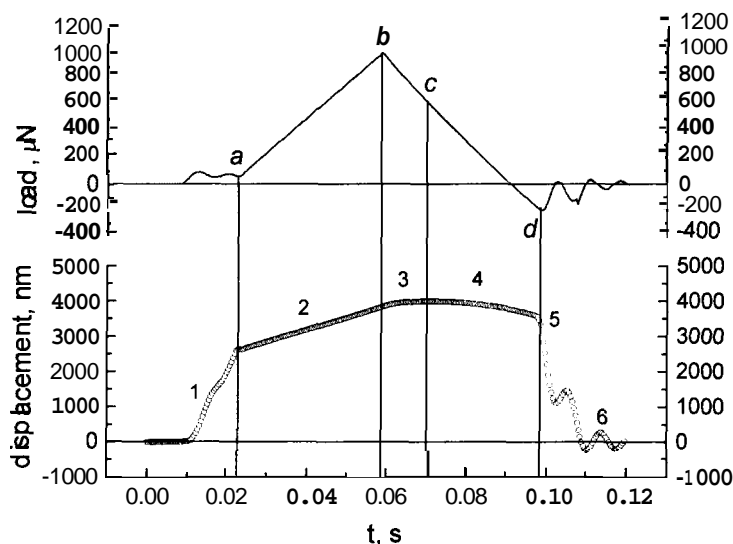


Fig. 5.1 (a) Load and displacement plotted vs. time for a cyclic test

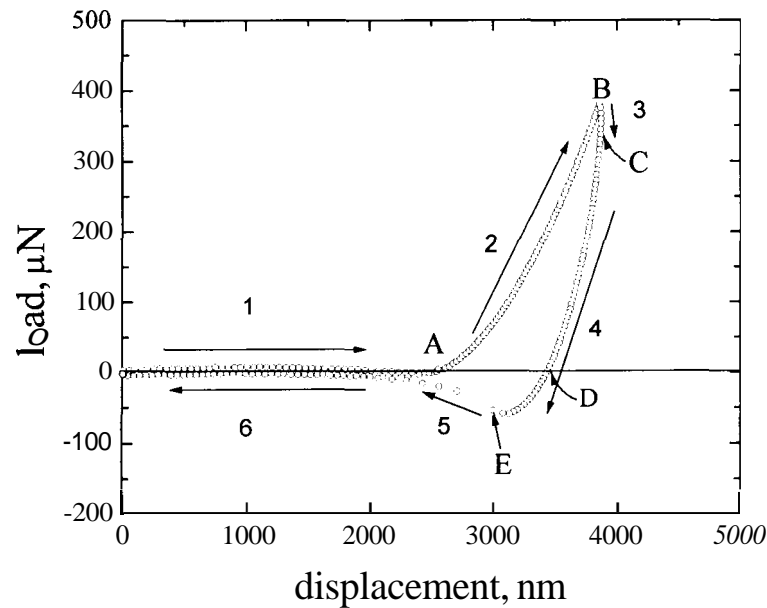


Fig. 5.1 (b) **A** typical hysteresis loop, showing load as a function of displacement.

Initially, the probe is about  $2.5\ \mu\text{m}$  out of contact, which is necessary to achieve tensile loads sufficient to overcome the probe-sample adhesive forces during the unloading portion of the cycle. During segment 1, the probe is brought rapidly into contact, which occurs at point **A**. If the time to achieve contact was less than about  $0.1\ \text{s}$ , inertial effects cause the indenter motion through air to be nonlinear, as is the case in Fig. 1(a). Once contact is achieved, the stiffness of the contact is large enough that inertial effects are no longer important. In segment 2, the load is increased at a constant rate  $dP/dt$  under feedback control to a predetermined maximum value  $P_{max}$ , which is reached at B. During the compressive portion of unloading (segment 3), the rate was  $-dP/dt$ . The unloading rate was not constant during the tensile portion (segment 4), since it is determined entirely by the extension of the indenter springs, which can not be controlled by the feedback system. The total time of contact  $t_c$  could varied between  $0.04\ \text{s}$  and  $2000\ \text{s}$ . **All** measurements were carried out at room temperature ( $\approx 25\ ^\circ\text{C}$ ).

Bulk rheological properties were measured using small amplitude oscillatory modulations in a parallel plate rheometer (Bohlin Instruments) over the frequency range 0.01 Hz to 30 Hz for temperatures of 5, 25, 35, 60, and 80 °C. Strains were kept in the range 0.0006 to 0.003 to insure that deformations were in the linear regime. Samples 1 mm thick with radii of 2 cm were cast in a Teflon mold. The rheological properties of the latexes have been discussed in the previous section.

### 5.3 Cyclic loading-unloading tests

Since all the theoretical models assume that the contacts have linear viscoelastic response, it is important to ensure that the strains and strain rates were low enough to avoid any plastic deformation. This was done as follows. First, a cyclic loading-unloading experiment was carried out at a high loading rate of  $-0.024$  N/s. Second, the probe was held above the location of this indent for 2 hours. After the rest period, the loading-unloading cycle was repeated. The displacements at initial contact, the slopes of the loading curves, the pull-off forces, and areas under the adhesion hysteresis curves were compared for the two cycles. These quantities were always identical within the experimental precision. Imaging studies demonstrate that lateral drift is negligible over tens of hours. To eliminate the possibility of vertical drift during the wait, the displacement to reach initial contact was determined at several symmetrically located nearby points. Their average was the same as the initial displacement to contact. Thus, we conclude there is no significant residual plastic deformation under the experimental conditions used in the experiments reported here.

For each of the latexes, sets of load-displacement curves were obtained over a wide range of loading rates. The same maximum displacement ( $1.5 \mu\text{m} \pm 5\%$ ) was used in each case. Contacts using the Berkovich tip were made deeper than 300 nm to minimize effects of tip rounding. Contacts using the spherical probe were shallower than  $2 \mu\text{m}$  so that the probe profile could be ap-

proximated as a paraboloid in the analysis. Indents were also substantially deeper than 10 nm to minimize effects due to surface roughness and possible variations of sample stiffness near the surface. Measurements of the near surface stiffness of Latex 1 were made at Naval Research Laboratory using the force modulation technique described in the introduction . The measured stiffness was found constant for indentations deeper than about 10 nm. Whether the near surface variation is due to surface roughness or true variation in creep compliance is not known.

Results for each latex, obtained with a Berkovich indenter, are shown in Fig. 5.2 (a), (b) and (c). The basic features are the same for each set of data and have been discussed in detail in conjunction with the Fig 5.1(b).

The adhesion hysteresis (i.e., the energy dissipated during a loading cycle) is measured by the area enclosed by the cycle. This hysteresis is largest for the shortest contact times and decreases continuously as the contact time increases.

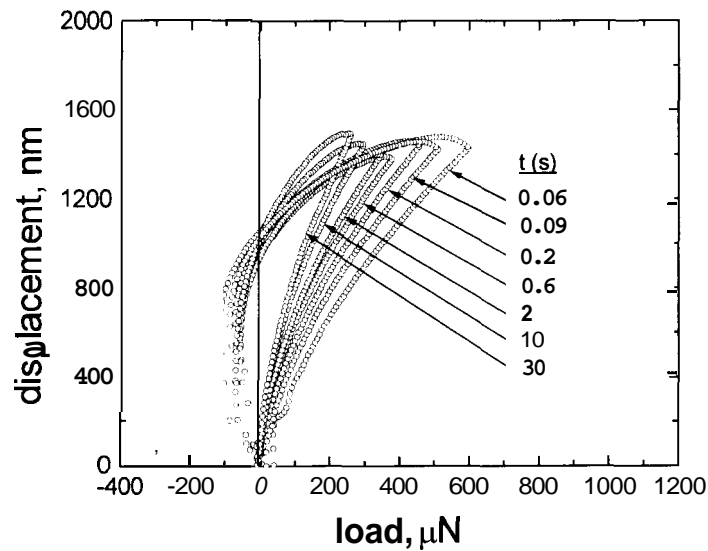


Fig. 5.2 (a) Cyclic tests results from indentations done on Latex # 1 with different time periods of contact

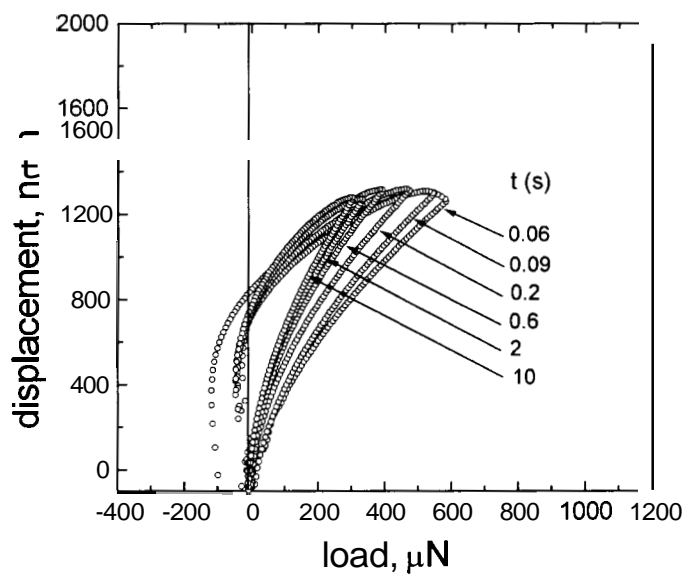


Fig. 5.2 (b) Cyclic tests results from indentations done on latex # 2 with different time periods of contact.

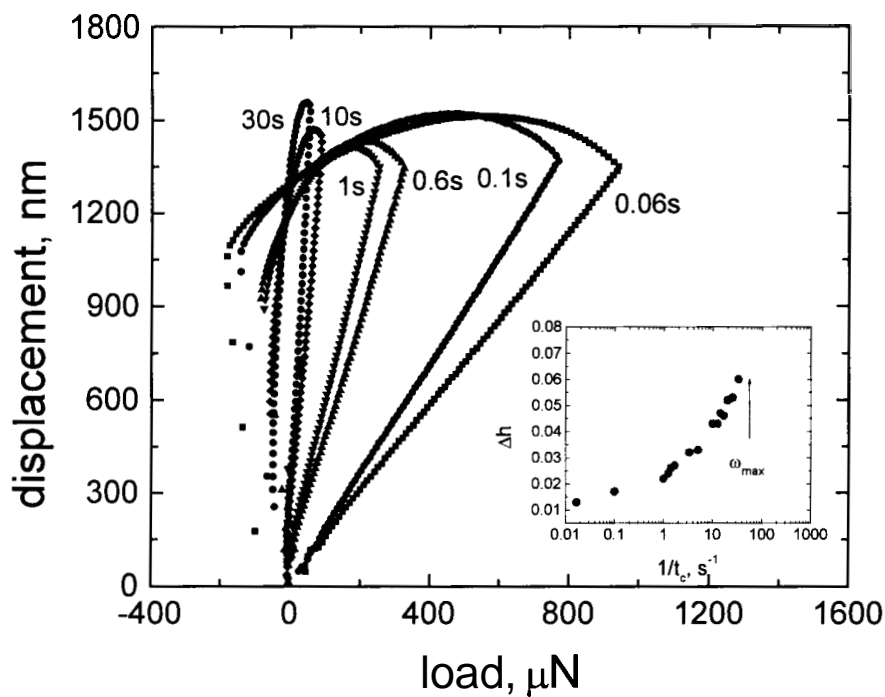


Fig. 5.2 (c) Cyclic tests results from indentations done on Latex # 3 with different time periods of contact. Insert shows the relative increase in contact depth after the load starts decreasing. This is an approximate way of measuring the relaxation time distribution in viscoelastic polymers.

For the shortest contact times, the probe continues to penetrate into the latex after the maximum applied load is reached. This is most pronounced for Latex 3. The maximum displacement occurs during the unloading portion of the cycle. This is precisely the behavior expected for long range viscoelastic creep. The insert in Fig. 5.2 (c) plots the portion of the penetration that occurs after maximum load as a function of inverse contact time;  $\Delta h$  is the difference between the maximum displacement and the displacement at maximum load.  $\Delta h$  reaches its largest value at the shortest  $t_c$ . Also shown in the insert is  $\omega_{\max}$ , the frequency at which the bulk  $\tan \delta$  has its maximum value. For Latex 3,  $\omega_{\max} \approx 0.02$  s at 24 °C. Creep effects should be largest at  $\omega_{\max}$  and decrease on either side. This decrease is clearly observed at short  $1/t_c$ . Unfortunately, the experiments could not reach the shorter contact times needed to confirm the expected decrease in  $\Delta h$  for large  $1/t_c$  but came closest to  $\omega_{\max}$  for Latex 3.

The largest tensile (negative) load achieved is the *effective pull-off force*,  $P_{\text{eff}}$ . Unlike the more familiar case of a spherical probe, the displacement is always positive at  $P_{\text{eff}}$ . This is a general property of conical indenters even for elastic materials. Using the approach of Maugis, it is straightforward to show that pull-off occurs when  $P_{\text{el}} = -54W^2 \tan^3 \alpha / \pi E^*$  and  $h_{\text{el}} = +3W \tan \alpha / E^*$  where  $\alpha$  is the cone's enclosed half-angle. The Berkovich indenter is frequently approximated as a cone in the indentation literature and we use this approximation in the analysis below.

The general features of data obtained with the spherical probe are the same as discussed above for the Berkovich probe. Fig. 5.3 and Fig. 5.4 show typical data obtained with the spherical probe. In contrast to the Berkovich data, the effective pull-off occurs at displacements near zero as is typically observed for elastic contacts.

#### 5.4 Results and Discussion (Work of Adhesion)

In this section, we demonstrate that the data obtained at the lowest loading rates are described well by the extended JKR model. In particular, we determine the appropriate experimental conditions necessary to extract the thermodynamic work of adhesion. The dynamics of contact formation and rupture are controlled by the interplay of the viscoelastic response of the materials and the thermodynamic work of adhesion. We now show how the thermodynamic work of adhesion can be determined. In the limit of very long contact times ( $t_c \rightarrow \infty$ ), the contact would behave elastically with modulus equal to the relaxed modulus  $E_\infty$ . In this case, the load-displacement data could be analyzed using the standard JKR theory. For a spherical probe, the work of adhesion could then be determined directly from the pull-off force since  $W = -2P_{el}/3\pi R$ . Johnson has suggested that  $P_{el}$  might be determined by plotting the effective pull-off force as a function of loading rate ( $P_{eff}$  vs.  $dP/dt$ ) and extrapolating to the limit  $dP/dt \rightarrow 0$ . However, for the latexes studied here, the smallest  $dP/dt$  obtainable with our apparatus is too large for such an extrapolation cannot be made reliably.

To overcome this difficulty, we use Johnson's extended JKR theory to analyze the entire hysteresis cycle. In this model, only the creep compliance function  $C(t)$  and two parameters, an effective work of adhesion  $W_{eff}$  and the effective range of the interaction potential  $h$ , are required to calculate an entire load-displacement cycle. We assume that the bulk  $C(t)$  is valid near the surface and determine  $W_{eff}$  and  $h$ , by fitting the entire set of load-displacement data for each latex, including results for both probe shapes. The load-displacement cycle was divided into three sections: loading (**AB** in Fig. 5.1(b)) unloading under compression (BCD), and unloading under tension (DE). In each region, the applied load  $P(t)$  was fit to a simple polynomial.

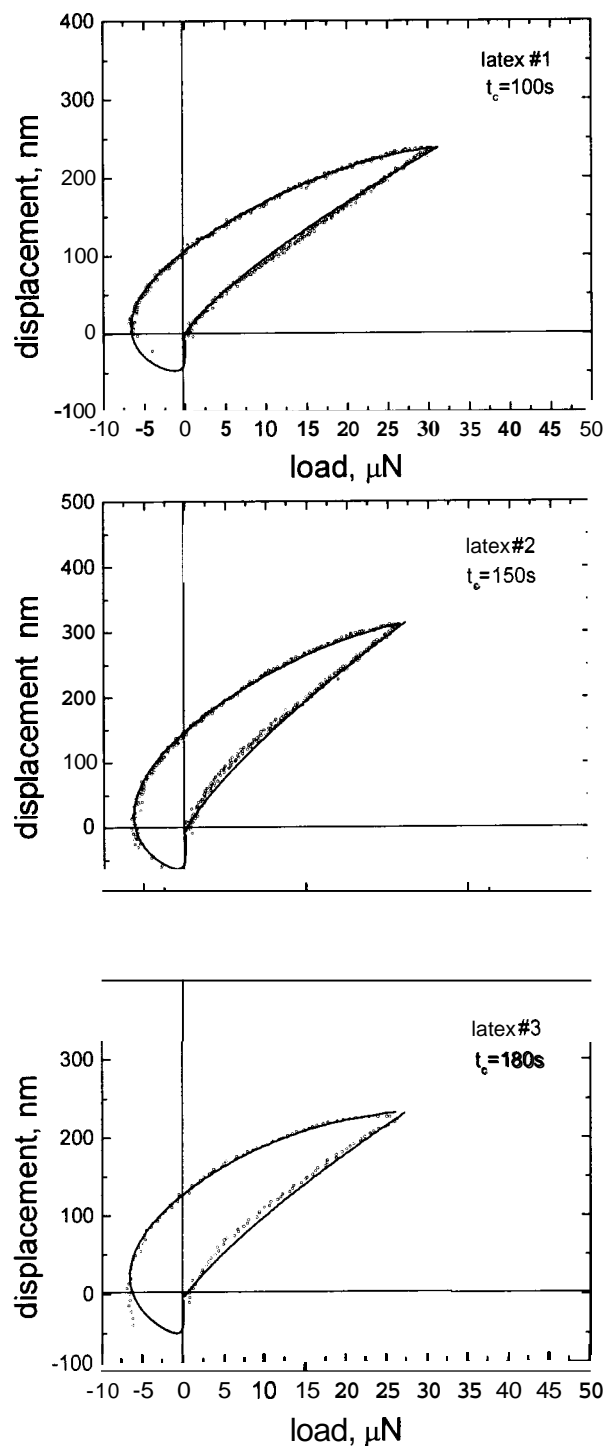


**Fig. 5.3** Model fits to hysteresis curves obtained at low loading rates on the three latexes with a spherical probe. Equations 8, 9, 11 and 12 described in section 3.2.1 were used to model these load-displacement curves.

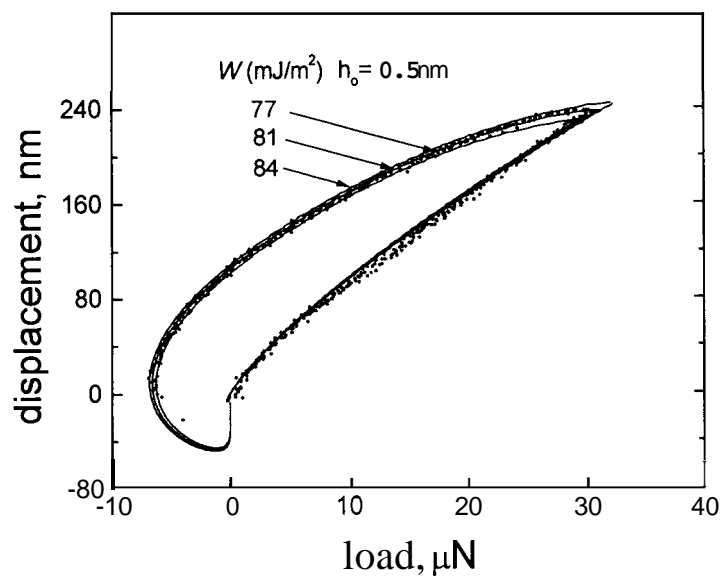


Fig. 5.4 (a) Effect of varying the work of adhesion,  $W$ , on the quality of fit. The interaction range parameter was held constant **0.5** nm and only the work of adhesion,  $W$ , was varied.

This polynomial was nearly linear in the first two sections, where feedback control was possible, but contained significant higher order contributions for unloading under tension, due to the lack of feedback control.

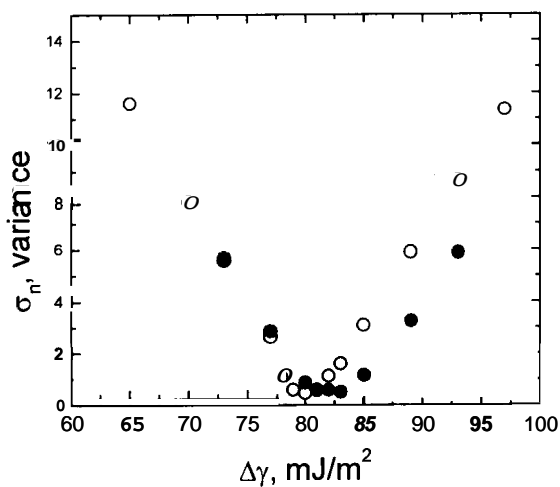


Fig. 5.4 (b) Effect of varying the work of adhesion,  $W$ , on the quality of fit.

Using this  $P(t)$ , the differential equation, (see chapter on LVEFM) was solved numerically for various  $W_{eff}$  and  $h_o$ .

Typical results for latex 1 are shown in Fig. 5.4 (a) for a spherical probe. For this data set, the best fits were obtained for  $h_o = 0.5$  nm and  $W_{eff} = 80$  mJ/m<sup>2</sup>. Fig. 4(a) compares fits for  $W_{eff} = 77$  mJ/m<sup>2</sup>, 81 mJ/m<sup>2</sup>, and 84 mJ/m<sup>2</sup> at constant  $h_o = 0.5$  nm. Visual comparison easily distinguishes the best fit to within  $\pm 5$  mJ/m<sup>2</sup>. Fig. 5.4 (b) and 5.4 (d) plot the variance of the fits as function of  $W_{eff}$  and  $h_o$ , respectively.

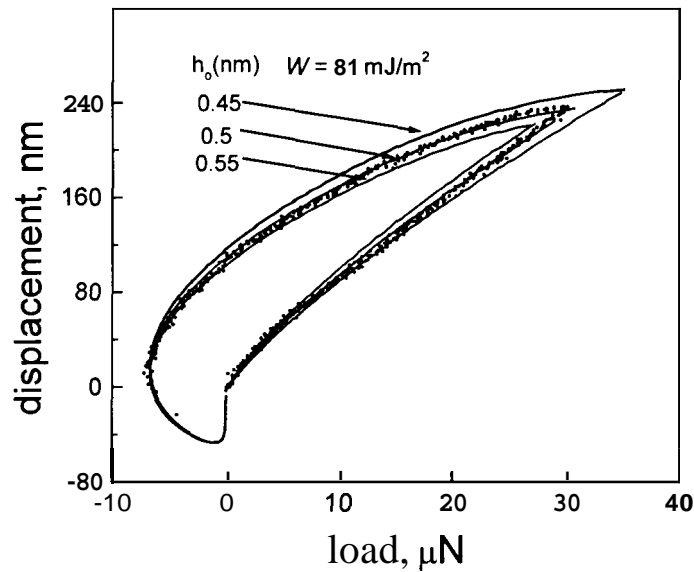


Fig. 5.4 (c) Effect of varying the range parameter,  $h_o$ , on the quality of fit. The interaction range parameter was held constant 0.5 nm and only the work of adhesion,  $W$ , was varied.

The solid dots are for the data shown in Fig. 5.4 (a) and the open circles are for another load-displacement cycle obtained under nearly identical conditions but at a different point on the sample. Fig. 5.4 (c) shows the sensitivity of the fits to  $h_o$ , for  $W_{eff} = 80$  mJ/m<sup>2</sup>; there is no difference in location of the minimum variance from point to point on the sample. We estimate the uncertainties in  $h_o$  and  $W_{eff}$  by their values at which the variance has increased ten percent above its mini-

mum. **By** this criterion,  $W_{eff}$  can be determined for a particular data set to within  $1 \text{ mJ/m}^2$  and  $h_o$  to within  $0.05 \text{ nm}$ .

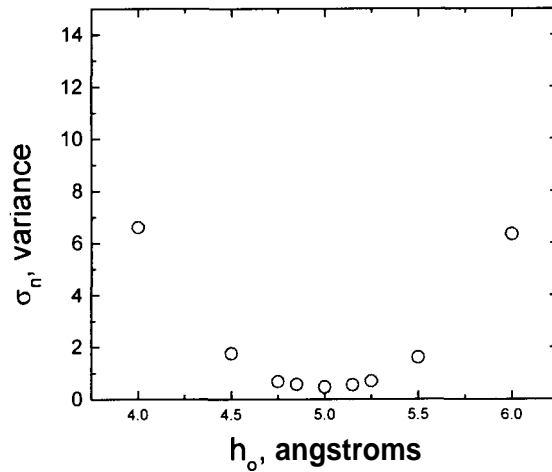


Fig. 5.4 (d) Effect of varying the range parameter,  $h_o$ , on the quality of fit.

The Johnson model is valid only if the loading rate is slow enough to avoid significant bulk creep. The range of  $dP/dt$  that satisfies this criterion can be determined from the requirement that the same  $W_{eff}$  must fit the entire load-displacement curve independent of  $dP/dt$ . Fig. 5.5 shows  $W_{eff}$  vs.  $dP/dt$  for latex 1.  $W_{eff}$  values extracted from data obtained at low loading rates are all the same. However, once  $dP/dt$  increases above a few  $\mu\text{N/s}$  for Latex 1, bulk creep effects become important and  $W_{eff}$  values increase. Thus, we empirically determine the range of  $dP/dt$  for which  $W_{eff}$  is constant and conclude that this value is  $W$ , the thermodynamic work of adhesion of the contact.

The data also has the expected geometrical scaling. Fig. 5.6 compares examples of the best fits to data obtained with the Berkovich indenter for each latex. In the calculations, the indenter was approximated as a cone with an enclosed half-angle of  $70.40^\circ$ .

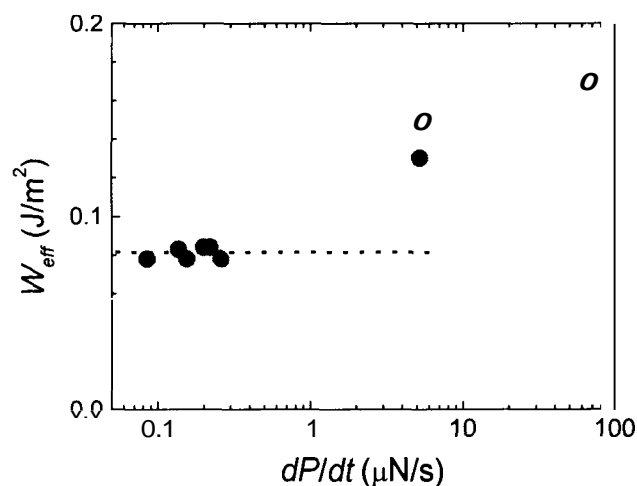


Fig. 5.5 Effect of loading rate,  $dP/dt$ , on the fitting value of work of adhesion,  $W$ .

Fits are as good as those obtained for the spherical probe. Furthermore, as shown in table 2, very similar values of the works of adhesion are obtained for each probe shape. The uncertainties quoted are the standard deviations of  $W_{\text{eff}}$  values determined for a range of low loading rates.

The values of  $W$  obtained for the three latexes are comparable to previous determinations of  $W$  (70-85  $\text{mJ/m}^2$ ) measured for similar styrene-butadiene latexes. These studies were carried out on individual particles by a very different method. AFM was used to measure the contact angles after the particles had spread on various substrates including calcite, glass, and polystyrene.

Fits to the data using the extended JKR model are excellent. Clear minima in the variance make it possible to determine  $W$  to within about  $\pm 1 \text{ mJ/m}^2$  and  $h_o$  to within about  $\pm 0.05 \text{ nm}$ . However, the optimum values of  $W$  determined from different data sets vary by more than  $\pm 1 \text{ mJ/m}^2$ . For example, the minimum variance for two sets of data shown in Fig. 5.4(b), differ by about  $2 \text{ mJ/m}^2$ .

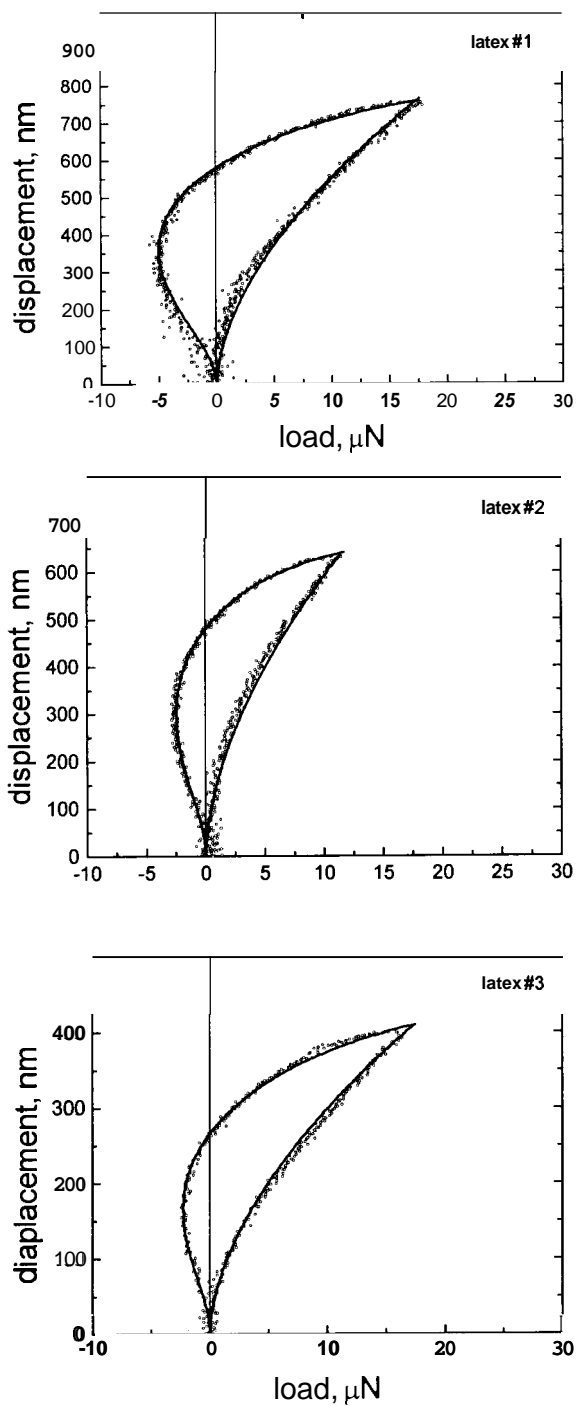


Fig. 5.6 Model fits to hysteresis curves obtained at low loading rates on the three latexes with a Berkovich probe.

The most likely cause of this variation is small lateral variations in the latex surface energy. Such variations could also explain the anisotropic spreading of individual latex particles on various substrates [8,9].

Latex	Berkovich Probe		Spherical Probe	
	$W(\text{mJ}/\text{m}^2)$	$h_o$ (nm)	$W(\text{mJ}/\text{m}^2)$	$h_o$ (nm)
1	<b>84 f3</b>	$0.5 \pm 0.05$	<b>80 f3</b>	$0.5 \pm 0.05$
2	<b>64 ±2</b>	$0.5 \pm 0.05$	<b>68 f3</b>	$0.5 \pm 0.05$
3	$75 \pm 1$	$0.5 \pm 0.05$	$73 \pm 2$	$0.5 \pm 0.05$

Table 5.2. Cohesive zone parameters for different latexes.

The effective range of the interaction potential was  $h_c = 0.5 \pm 0.05$  nm for all of the latexes regardless of probe shape. This distance is comparable to spacings in molecular or inert gas solids and hydrogen bond lengths. It clearly indicates that the interaction between the diamond probe and the latexes is short-range.

The fits are poorest on the loading portion of the cycle (see Fig. 5.3, Fig. 5.4(a) and Fig. 5.6). Sometimes the curvature is slightly higher than the data and sometimes slightly lower. This variation is likely due to local variations in the compliance resulting from the residual crosslinked structure of the latex particles. Thus, more systematic studies of these variations could be used to characterize local variations in mechanical properties at sub-micrometer length scales. As seen from Table 5.2, adhesion is greatest for Latex # 1 because of its good film forming characteristics. Latex T<sub>g</sub> also has an influence on its adhesion to the Diamond tip.

## 5.5 Conclusions

Cyclic loading/unloading experiments were carried on three styrene-butadiene copolymer latexes with a nanoindenter. Loading conditions were chosen to avoid plastic deformation. Hysteresis occurs because of unrecoverable work done during each cycle. Specifically, a higher force is needed to reach a certain displacement during loading than during unloading. The amount of energy dissipated in each cycle increases with increasing loading rate for the range of loading rates that could be achieved with the nanoindenter.

These data are used to verify an extended JKR model proposed recently by Johnson. This model combines classical JKR theory with a fracture mechanics model of crack initiation and growth in linear viscoelastic materials due to Schapery. The major assumption of the model is that viscoelastic effects are limited to the periphery of the contact. Longer-range creep effects are ignored. This limits applicability of the model to low loading rates. The extended JKR model provides excellent fits to the data obtained at low loading rates. The fitting is robust since distinct minima are found for both fitting parameters, the work of adhesion and the effective range of the potential acting between the probe and substrate.

Works of adhesion are determined to within a few  $\text{mJ/m}^2$  and are consistent with previous determinations on similar materials. This uncertainty appears to be caused mostly by point-to-point variations in surface properties. Thus, the technique can be used to study small heterogeneity in surface energy at the sub-micrometer scale.

At higher loading rates, bulk creep effects become increasingly important and the assumptions of the Johnson model are no longer valid and the more complex HBKL [7] model must be used. However, the HBKL analysis is simplified by the knowledge of the work of adhesion and range parameter obtained by the extended JKR model. In a subsequent paper, we apply the HBLK model to our data and discuss the resulting stress intensity factors.

## 5.6 References for chapter 5

1. Carpick, R. W., Ogletree, D. F., Salmeron, M. *Appl. Phys. Lett.* 1997, 70, 1548.
2. Lantz, M. A., O'Shea, S. J., Welland, M. E., Johnson, K.L. *Phys. Rev. B* 1997, 55, 10776.
3. Johnson, K. L. *Proc. R. Soc. Lond. A* 1997, 453, 163.
4. Unertl, W. N. *J. Adhesion* 2000, in press.
5. Johnson, K. L. *Microstructure and Microtribology of Polymer Surfaces*, eds. V. V. Tsukruk and K. J. Wahl, American Chemical Society, Washington, D.C., 2000.
6. Hui, C.-Y., Baney, J. M., Kramer, E. J. *Langmuir* 1998, 14, 6570.
7. Lin, Y. Y., Hui, C.-Y., Baney, J. M. *J. Phys. D: Appl. Phys.* 1999, 32, 2250.
8. Unertl, W. N. *Langmuir* 1998, 14, 2201.
9. Woodland D. D, Unertl, W. N. to be Published.

## Chapter 6: Creep tests performed on SB Latex films

### 6.1 Introduction

Dynamic contact's to viscoelastic styrene-butadiene films were made using the nanoindentation device. In this section we will discuss the stress intensity factors obtained from creep tests. Determination of stress intensity factor requires specification of the cohesive zone parameters a priori. In the previous chapter we discussed the method for determining the cohesive zone parameters. In this chapter we will discuss the method to determine stress intensity functional and investigate its dependence on the crack propagation velocity. Stress intensity factors for styrene-butadiene latexes are reported.

### 6.2 Experimental method

The samples were carboxylated styrene-butadiene copolymer latexes provided by the Performance Chemicals Division of Omnova Solutions, Inc. The Latexes differed in their glass transition temperatures, which were in the range 0 °C to 28 °C, and their particle size. Thick films of the aqueous suspension were cast onto Mylar substrates followed by drying in air, washing in distilled water and heating to about 50 °C above  $T_g$  to insure complete film formation. The final film thickness was  $\geq 300 \mu\text{m}$  and were several orders of magnitude thicker than the deepest indentations. The root-mean-square surface roughness of the films was determined by scanning probe microscopy to be less than 10 nm. The bulk viscoelastic properties were characterized by measuring the shear modulus over the frequency range 0.01 Hz to 30 Hz for temperatures of 5, 25, 35, 60, and 80 °C and will as discussed in chapter 4. The time-dependent relaxation modulus  $E(t)$  was calculated from this data using time-temperature superposition and assuming a Poisson ratio of 0.5. For these materials, instantaneous relaxation moduli  $E_o(t \rightarrow 0)$  were near 1 GPa and long time storage moduli  $E_\infty(t \rightarrow \infty)$  were in the range 0.1-0.5 MPa. The creep compliance

$\phi(t)$  is a material property of a viscoelastic material. Contacts were controlled with a predetermined loading/unloading cycle  $P(t)$ . The displacement (also called deformation or depth of penetration)  $h(t)$  of the rigid probe was measured continuously during the contact cycle. Thermal drift of about 0.05 nm/s limited measurement times to less than about 800-1000 s. Two types of measurement were made: creep and cyclic. Creep tests started with the probe in contact at the lowest possible load ( $-2 \mu\text{N}$ ). The load was increased to a predetermined value, typically in less than 50 ms, then held constant except for a small decrease due to stretching the 159 N/m springs in the indenter as the probe penetrated into the sample. Cyclic tests will be described in the next section. All measurements were carried out at room temperature ( $\approx 25 \text{ }^\circ\text{C}$ ).

### 6.3 Results

This Section describes typical displacement vs. load data and creep data. Fig. 6.1 shows a set of displacement vs. load data obtained with a Berkovich indenter on latexes with  $T_g = 5 \text{ }^\circ\text{C}$ , and  $20 \text{ }^\circ\text{C}$ . The loading and unloading times were 0.1 s. The maximum load was adjusted

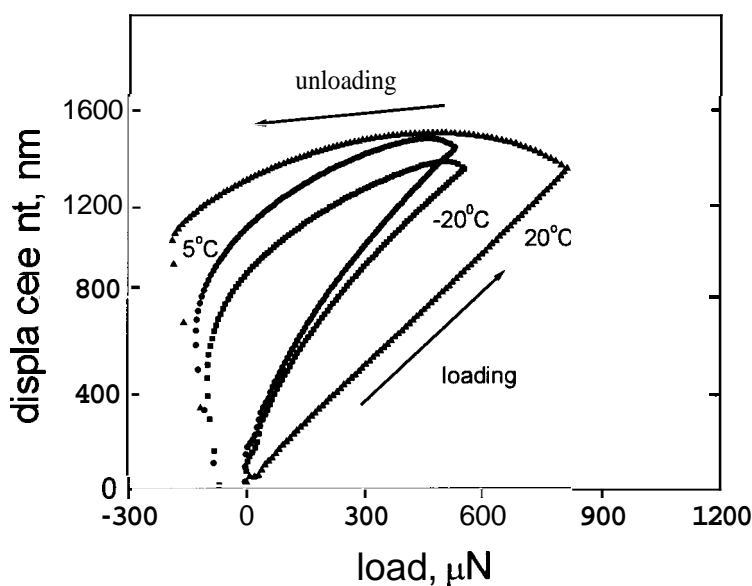


Fig. 6.1 Cyclic tests performed under similar loading conditions on the three latexes.

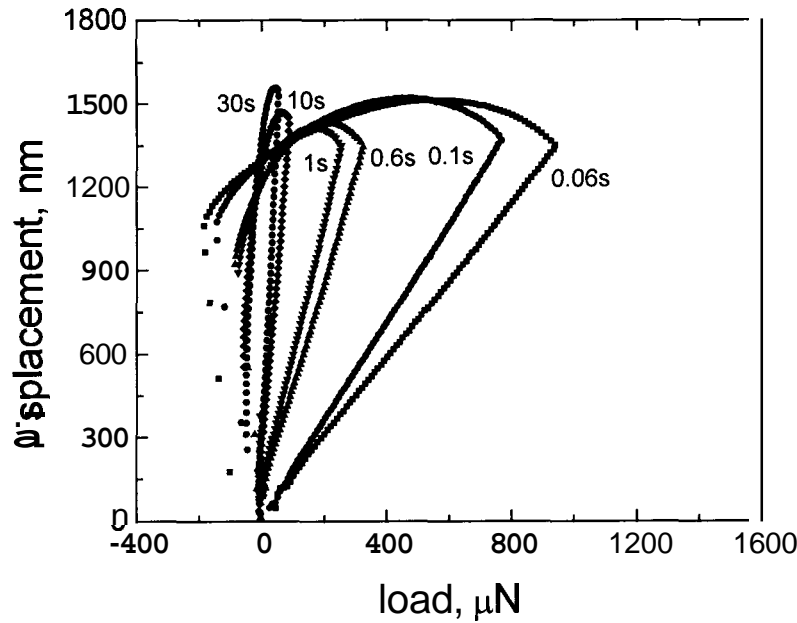


Fig. 6.2 Cyclic tests performed on latex # 3 under different time scales of contact. It can be seen that as the contact time increases the material behaves as a much softer material.

to achieve approximately the same penetration into each sample. Fig. 6.2 shows the effect of increasing the contact time for the case of  $T_g = 20^\circ\text{C}$ .

The area enclosed by each cycle is the work done to move the probe through the cycle. This area would be zero for a perfectly elastic contact. Displacement increases smoothly during the loading cycle. In all cases in Fig. 6.2, the displacement  $h$  continues to increase during the initial part of the unloading cycle, i.e., *well after* the maximum load is achieved. These delayed maxima are due to long-range creep effects occurring on a length-scale is comparable to the contact radius  $a$  [1,2,3]. Such creep effects are expected to be most pronounced when  $t_c$  is comparable to a characteristic relaxation time  $T$  of the viscoelastic sample. The insert in (previous chapter) b shows the fractional increase in displacement beyond maximum load  $\Delta h \equiv (h_{\max} - h_{p_{\max}})/h_{p_{\max}}$  as a function of inverse contact time.  $\Delta h$  increases significantly as the contact time decreases. Calculations based on the Ting model [1] suggest that  $\Delta h$  should reach a maximum when  $1/t_c \propto \omega_{\max}$  where  $\omega_{\max}$  is the measured frequency at which the loss tangent has its maximum.

The arrow in the insert indicates  $\omega_{max}$ . Unfortunately, the instrument used for these experiments is unable to make measurements at smaller  $t_c$  to determine whether  $\Delta h$  decreases at higher  $t_c$  as expected.

After passing through its maximum value, the displacement decreases continuously as the load decreases into the tensile (negative load) regime. In this regime, the load can no longer be controlled by the feedback system of the PicoIndenter since it is due only to the stretched springs of the indenter. The load reaches its maximum negative value at  $P_p$ .  $P_p$  is frequently called the pull-off force because, for measurements carried out under load control on elastic materials, the contact becomes unstable at this point. This instability is described by Greenwood [4]. The probe and sample separate when the slope of the unloading curve becomes equal to the inverse stiffness of the indenter springs, e.g.,  $dh/dP = -1/\kappa = -6.3 \text{ mm/N}$ . In the present work, in contrast to most SFM measurements where  $\kappa$  is very small, the separation point is not at  $P_p$  because of the large stiffness of the indenter. Furthermore, for viscoelastic materials the displacement  $h_p$  at  $P_p$  depends on the loading rate, unlike elastic materials.

Fig. 6.3 shows creep data for the latex with  $T_g = 5 \text{ }^\circ\text{C}$  obtained with the spherical indenter and Berkovich indenters. Loading was in 0.05 s. The initial elastic penetration is followed by a much slower viscoelastic creep response. The other latexes have similar creep response.

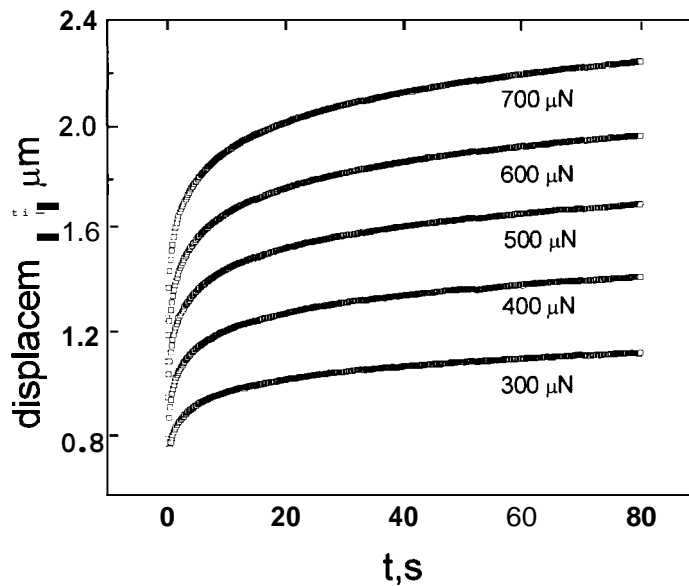


Fig. 6.3 Creep test results from indents made on latex 1 with a spherical indenter

#### 6.4 Discussion

In this section, we use the HBK [5] model to analyze the creep relaxation data. Their analysis assumes the probe is a paraboloid [ $f(r) = r^2/2R$ ] but their results are easily extended to other axisymmetric shapes. The substrate is assumed to be a linear viscoelastic material whose mechanical response is described by a creep compliance function  $\phi(t)$  with  $\phi(0) = \phi_0$  and a stress relaxation function  $\psi(t)$  with  $\psi(0) = \psi_0$ . These functions are assumed unchanged from their bulk values near the surface. The periphery of the contact is described as the tip of a closing crack. HBK assume the cohesive zone at the crack tip must be finite in extent, that stresses are finite everywhere, and the rate of energy flow into the cohesive zone is dependent on the crack speed,  $\dot{a}(t) = da/dt$ . Following the usual approach of fracture mechanics, the energy flow is parameterized in terms of a Mode I stress intensity factor  $K_I$ .  $K_I$  is a measure of the magnitude of the stress field at the crack tip. In general,  $K_I$  depends on the compliance function, the geometry of the contact, the load, and the displacement. Unlike elastic materials for which  $K$  is a constant,

the stress intensity factor for a viscoelastic material will in general be a functional of the time, the displacement, and the speed of displacement,  $K_I [\dot{a}(t), h(t), t]$ .

For axisymmetric contacting surfaces with parabolic profiles, the contact area and deformation are given by

$$a^3(t) = \frac{3R}{4} \left\{ \frac{3R\pi\phi_o^2 K_I^2(t)}{2} + \phi(t) * P(t) + \phi_o K_I(t) \sqrt{\left[ \frac{3\pi R\phi_o K_I(t)}{2} \right]^2 + 3\pi R [\phi(t) * P(t)]} \right\} \quad (1)$$

and

$$h(t) = \frac{a^2(t)}{R} - \frac{K_I(t) \sqrt{\pi a(t)}}{\psi_o} \quad (2)$$

where \* represents an integral operator, e.g.,  $\phi(t) * P(t) = \int_0^t \phi(t-\tau) \frac{\partial P(\tau)}{\partial \tau} d\tau$ . As

discussed by Ting [13, equations (1) and (2) are valid only if  $\dot{a}(t) > 0$ . The speed of the crack is determined using Schapery's solution for a closing crack [6], i.e.  $\dot{a}(t) > 0$ . In this model, the cohesive forces acting between the surfaces are approximated using a Dugdale potential with range  $h_o$ , stress per unit area of  $\sigma_o$ , and work of adhesion  $W = \sigma_o h_o$ . The crack speed is given by

$$\dot{a}(t) = \frac{\pi h_o^2 K_I^2(t)}{8W^2} \left[ \frac{\phi_o}{\lambda(K_I)} \sqrt{\frac{\pi}{4}} \frac{\Gamma(m+1)}{\Gamma(m+3/2)} \right]^m \frac{1}{[1 + \lambda(K_I)]^2} \quad (3)$$

with

$$\lambda(K_I) = \frac{2m+1}{4W(m+1)} \phi_o K_I^2(t) \left\{ 1 + \sqrt{1 - \frac{8Wm(m+1)}{\phi_o K_I^2(t)(2m+1)^2}} \right\} - 1 \quad (4)$$

where  $\Gamma(m)$  is the gamma function and the creep compliance function has been assumed to have the form,

$$\phi(t) = \phi_o + \phi_1 t^m .$$

Schapery showed that only the behavior of  $\phi(t)$  near  $t \approx L/\alpha(t)$  is important, where  $L$  is the crack length, defined as the distance from the crack tip at which the crack width becomes equal to  $h_o$ . For times near  $t \approx L/\alpha(t)$ ,  $\phi_1$  and  $m$  can be calculated from the measured creep compliance using a method described by Schapery.

For a load controlled experiment,  $P(t)$  is specified and the above equations are solved simultaneously to obtain the time variation of  $a$  and  $h$ . In a creep test,  $P(t) = 0$  if  $t < 0$  and  $P(t) = P_o$  if  $t \geq 0$ , where  $P_o$  is constant. For this case, HBK show that

$$K_I = \sqrt{\frac{1}{4\pi\phi_o^2\alpha^3(t)} \left[ \frac{4a^2(t)}{3R} - P_o\phi(t) \right]} . \quad (6)$$

The displacement  $h(t)$  is determined from equation (2) using the value of  $\alpha(t)$  obtained by numerical solution of the differential equation

$$\frac{da(t)}{dt} = \frac{\pi^{3/2}h_o^2\phi_1^{1/m}\Gamma(m+1)}{4W^2\phi_o^{1/m}\Gamma(m+3/2)} \frac{K_I^2}{\left[ 1 + \lambda \left( \frac{\phi_o K_I^2}{2W} \right) \right]^2 \left[ \lambda \left( \frac{\phi_o K_I^2}{2W} \right) \right]^{1/m}} \quad (7)$$

The solution requires some care since equation (7) diverges at  $t = 0$

These results of the HBK model were used to fit the creep data of Fig. 6.3. In our analysis of small contacts, we focus on  $h$  rather than  $a$  because  $h$  is a directly measurable quantity whereas  $a$  is not. The fits used the measured bulk creep compliance function. For data obtained with the Berkovich indenter, the probe was approximated as a cone with enclosed half-angle of  $70.299^\circ$ . Equivalent expressions to equations (1)-(7) for a conical indenter (or any other axisymmetric probe) are straightforward to derive as discussed earlier.  $W$  was determined from the displacement vs. load data as described below. The stress per unit area of  $\mathbf{a}_r = W/h_o$  was estimated using an effective interaction range  $h_o = 0.5$  nm.

The thermodynamic work of adhesion between each latex and the probe was determined from dynamic contact data like that in Fig. 6.1 and Fig. 6.2 using the method suggested by Johnson. This has been discussed in the previous chapter. For an elastic substrate and a parabolic or spherical probe, it is well-known that the maximum tensile load (usually called the pull-off force) depends on the thermodynamic work of adhesion  $W$ , and the radius of curvature of probe, but is independent of the modulus [7]. In contrast, as is clear from Fig. 6.1 that the maximum tensile load for viscoelastic materials is strongly influenced by the rate of loading and unloading. As in HBK, Schapery's theory of crack growth is used to determine  $\mathcal{K}$ , but Johnson also treats the case of an opening crack [ $\mathcal{K}(t) < 0$ ]. Johnson's approximate theory allows the entire loading-unloading cycle to be calculated for cases in which the contact time is long compared to  $T$ , the characteristic relaxation time of the viscoelastic material.

We used Johnson's model to fit the displacement vs. load data as described in the previous chapter. The measured creep compliance was used. The only remaining parameter in the model is the work of adhesion, which we used as a fitting parameter. Fig. 5.3, in the previous chapters, shows an example for the latex with  $T_g = 5^\circ\text{C}$  and a contact time of 160 s. Fits are shown for  $W_{eff} = 75 \text{ mJ/m}^2$ ,  $85 \text{ mJ/m}^2$ , and  $95 \text{ mJ/m}^2$ . The loading cycle is fit equally well by all these  $W_{eff}$ , but the unloading cycle is best fit by  $W_{eff} = 85 \text{ mJ/m}^2$ .  $W_{eff} = 95 \text{ mJ/m}^2$  produces displacements and maximum tensile load that are too large whereas  $W_{eff} = 75 \text{ mJ/m}^2$  produces values that are too small.  $W_{eff}$  can easily be determined to within about  $\pm 3 \text{ mJ/m}^2$  for each displacement vs. load data set. In the range for which Johnson's model is valid,  $W_{eff}$  should be independent of  $dP/dt$ . This condition is clearly fulfilled for  $dP/dt$  less than about  $0.3 \mu\text{N/s}$ . At higher  $dP/dt$ , bulk creep effects are clearly present in the displacement vs. load data. The average of the  $W_{eff}$  for  $dP/dt = 50.03 \mu\text{N/s}$  yields  $W = 81.8 \pm 0.3 \text{ mJ/m}^2$  for the latex with  $T_g = 5^\circ\text{C}$ .

Fig. 6.4 shows  $K_I(t)$  for the latex with  $T_g = 5^\circ\text{C}$  determined from the data of Fig. 6.3 using the HBK model. For all of the latexes studied,  $K_I$  lies in the range  $7 - 24 \text{ kN/m}^{3/2}$  for both

Berkovich (Fig. 6.4a) and spherical (Fig. 6.4b) probes. For a given load, the  $K_I$  for the Berkovich indenter increase more slowly and reach smaller values than for the spherical indenter. At shorter times, the behavior is very different. For the Berkovich indenter,  $K_I$  decreases initially, passes through a minimum, and then rises slowly. For the spherical indenter,  $K_I$  increases over the entire range. The stress  $\sigma$  at the periphery of the contact can be estimated since, for a simple crack,  $\sigma = K_I \sqrt{\pi L}$  where  $L$  is the crack length [7]. Using values of  $L$  estimated by the Schapery theory, we find  $\sigma$  to be on the order of a few hundred MPa.

The precise values of  $K_I$  are also dependent on the choice of  $h_o$ , the effective range of the potential acting between the diamond probe and latex specimen. The results presented in Fig. 6.4 assumed  $h_o = 0.5$  nm. Increasing  $h_o$  to 0.75 nm causes a nearly uniform upward shift in  $K_I$  values by about 4 % for the data at 700  $\mu$ N load and less for the other loads. Decreasing  $h_o$  to 0.25 nm causes a downward shift in  $K_I$  values by about 4 % at 700  $\mu$ N and less for other loads. Thus, the effect of changing  $h_o$ , is small, for example, compared to changing the load.

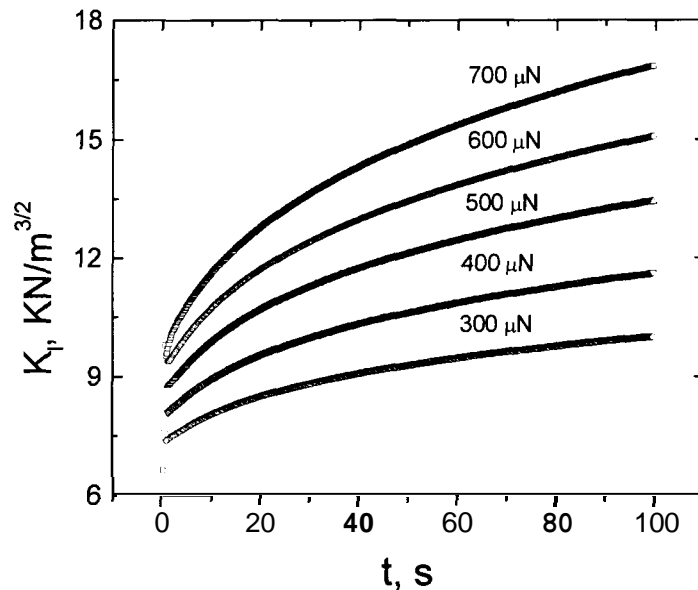


Fig. 6.4 (a) Stress intensity factor as a function of time from creep tests conducted on latex 1 with a Berkovich probe. The stress intensity factor is an increasing function of contact time for crack closing (bonding)

Since  $h$  (and  $a$ ) are functions of  $K_I$ , they could, in general, depend on the entire loading history. If this were the case, there would be little utility in using  $K_I$  to describe the adhesion of the contact. However, if the relationship between  $h$  and  $K_I$  can be approximated by a simple functional relationship, then  $K_I$  can provide a useful alternative to the normal approach that emphasizes surface energy. Empirically, we find that all of the creep data for all of the latexes and both indenter shapes have the approximate functional form

$$K_I \propto \left( \frac{dh}{dt} t \right)^n \quad (8)$$

where  $n$  is very close to one-half. This is demonstrated in Fig. 6.5, which includes data from the entire range of  $T_g$ , the entire range of loads, and both indenter shapes. The overall trend of the

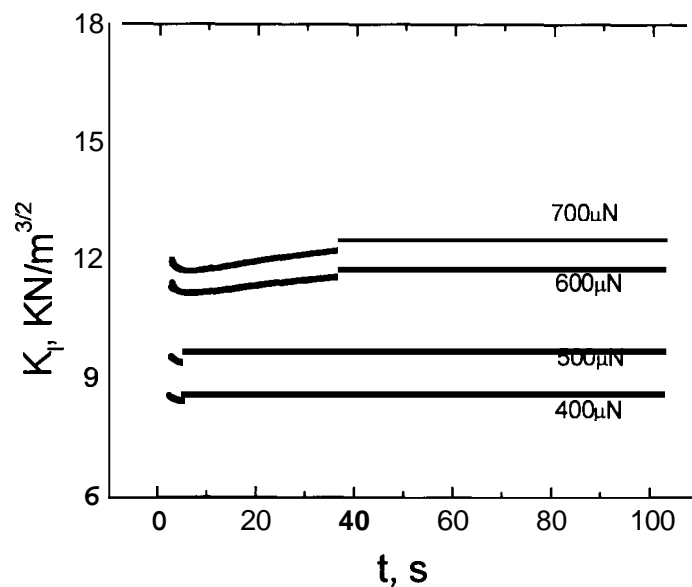


Fig. 6.4 (b) Stress intensity factor as a function of time from creep tests conducted on latex 1 with a spherical probe. The stress intensity factor is an increasing function of contact time for crack closing (bonding)

data is clearly described by equation (8). However, within the band of data there are weaker trends. For example, data obtained with a Berkovich probe tends to lie higher than that obtained with a spherical probe. Data for higher loads lies above data for lower loads. Data for high  $T_g$  samples lies below that of low  $T_g$  samples.

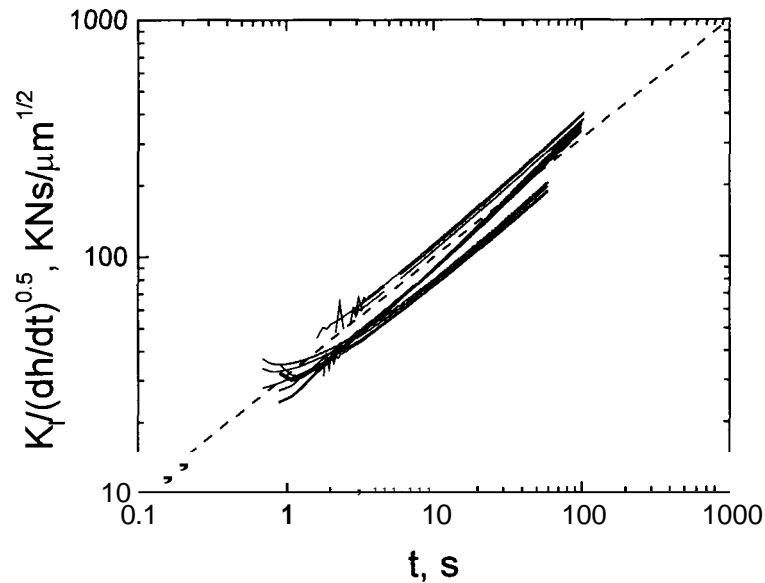


Fig. 6.5 Stress intensity factor normalized by the crack propagation velocity for creep tests. Data shown here is for both probe shapes and different latexes. The universal dependence of stress intensity on crack velocity is in accordance with the HBK theory.

## 6.5 Conclusions

We have measured load-displacement and creep relaxation for a series of styrene-butadiene latexes. Delays between the time of maximum load and maximum displacement demonstrate the presence of bulk viscoelastic creep, which is significant for certain ranges of contact time. Delayed maxima are not observed if the loading rate is small enough. In this low-loading-rate regime, we show that a model due to Johnson allows reasonable values of the thermodynamic work of adhesion to be extracted from the data as long as the loading rate is small enough. This model considers viscoelastic effects at the contact periphery and neglects bulk creep effects.

From the perspective of fracture mechanics, changing contact area corresponds to opening or closing of a crack whose tip is at the periphery of the contact. The detailed processes that control this motion are assumed to occur in a small ‘failure zone’ at the crack tip. Outside this zone, the material is linearly viscoelastic. Inside, its behavior can be complex. It may be nonlinear and viscoelastic, as occurs in crazing. In the simplest cases, only atomic-scale interactions, such as vander Waals interactions, may be involved. The stress intensity factor  $K_I$  is a parameter that represents the reaction of the failure zone on the surrounding material. It is a direct measure of the local stresses that act on the failure zone. The stress intensity factor is the most information a contact mechanics measurement can obtain about the mechanism of failure at the crack tip. Once  $K_I$  is known, the response of the crack to changing externally applied stresses is completely determined regardless of the complexity within the fracture zone.

The HBK model provides the framework to carry out this analysis for axisymmetric adhesive contacts involving linear viscoelastic materials. In general,  $K_I$  can be a complex functional of the history of the contact. If this were always true, each contact situation would be a special case. However, the creep studies presented here suggest that  $K_I$  can have a simple form. Specifically, we show empirically, that  $K_I$  can be approximately describe by a simple function of the displacement (deformation) and time for the entire set of creep data. The dependence on glass transition temperature, load, and indenter geometry are found to be weak. This result shows that the stress intensity factor has a nearly universal functional form for the carboxylated styrene-butadiene latexes and range of creep loading conditions used here. In the future, we will determine whether this result extends to a broader range of loading histories and to other materials systems.

## 6.6 References for Chapter 6

1. Ting, T C. T. *J. Appl. Mech.* **1966**, 33, 845, Ting, T.C.T. *J. Appl. Mech.* **1968**, 35, 248.
2. Johnson, K. L *Microstructure and Microtribology of Polymer Surfaces*, eds. V. V. Tsukruk and K. J. Wahl, American Chemical Society, Washington, D.C., **2000**.
3. W. N. Unertl, *Microstructure and Tribology of Polymers*, eds. . V. V. Tsukruk and K. J. Wahl (American Chemical Society), Washington, DC, **2000**.
4. Greenwood, A. J. *Proc. R. Soc. Lond. A* 1997,453, 1277.
5. Hui, C.-Y., Baney, J. M., Kramer,E. J. *Langmuir* 1998, 14, 6570.
6. Schapery, R. A. *International J. Fracture* 1989, 39, 163.
7. Young, R. J., Lovell, P. A. *Introduction to Polymers*, Second ed. (Chapman & Hall, London, 1991).

## Chapter 7. Dynamic cyclic tests at all loading rates

### 7.1 Introduction

Interfacial processes such as dynamic wetting of a solid surface by a liquid, fracture of an adhesive joint and friction between two solids are rate dependent. The rate dependence is attributed to either the interface itself or the bulk of the material. **Soft** elastomeric materials are ideally suited for fracture studies using the basic principles of contact mechanics. In a typical contact experiment, after an initial jump to contact the contact radius increases as the surfaces are brought together and then decreases as they are pulled apart. Increasing contact radius is referred to as bonding or “crack closing” and decreasing contact radius is called debonding or “crack opening”. According to the JKR theory of contact mechanics, when two elastic solids establish a complete contact, then under equilibrium, the elastic forces are completely balanced by the interfacial forces. The JKR relation gives for a sphere on a flat surface,

$$P = \frac{4E^* a^3}{3R} - \sqrt{8W\pi E^* a^3} \quad (1)$$

Where  $P$  is the applied load,  $a$  the radius of contact,  $E^*$  the effective elastic modulus,  $W$  the interfacial work of adhesion and  $R$  the radius of the probe. The JKR theory has limited applicability due to the requirement that the material be linear elastic. Most latexes are viscoelastic especially at temperatures close to the glass transition temperatures ( $T_g$ ). Till recently there was no theory to adequately treat contacts to linear viscoelastic materials.

---

\*The standard procedure to solve a boundary value problem in the linear quasi-static theory of viscoelasticity is to apply the Laplace transform to the time dependent field equations and boundary conditions. *So* if there exists a solution to the transformed problem then a solution to the original problem can be found by taking the transform inversion, which could be mathematically intricate.

For linear viscoelastic materials the contact radius depends on the entire history of the applied load rather than on the current state on load. Material deformation during the debonding phase unloading depends on the deformation during the bonding phase. Similarly the stress intensity factor,  $K_I$ , is determined by the entire loading history and not simply the current state of load. In the JKR theory the strain energy release rate or the energy flow to the crack tip per unit crack advance,  $G$ , is related to  $K_I$  by

$$G = \frac{K_I^2}{2E^*} \quad (2)$$

Where  $E^*$  is the effective modulus of the material. This clearly suggests that the energy flow to the crack tip is independent of the details of the bonding and separation process at the crack tip (edge of contact) or in the bulk of the material since the material properties are represented by a single quantity,  $E^*$ . However for a viscoelastic material a single modulus for the entire contact zone cannot be defined since the material response is stress/strain dependent and different points in the contact zone are subjected to different stress/strain histories. Therefore, the energy flow to the crack tip cannot be simply defined for a viscoelastic material since bulk dissipation renders time dependence to the process.  $G$  depends not only on the material rheological properties (creep compliance) and the stress intensity functional but also on the details of the bonding or debonding process.

When the contact radius is a non-decreasing function of time, the JKR theory for a viscoelastic contact has been extended by Hui et al [1] using the crack closing theory by Schapery. The Dugdale-Barenblatt cohesive zone model was used and it was shown that the contact radius depends only on the current value of stress intensity factor,  $K_I$ . It was then suggested that the relationship between crack velocity and  $K_I$  could serve as an alternative way for characterizing the adhesion between viscoelastic surfaces. Stress intensity factors for contact on styrene-butadiene latex films with diamond probes was obtained by Giri et al [2] using this methodology by Hui et

al for a simple creep experiment. It was then shown that  $K_I$ , could be expressed in a simple functional form, given by

$$K_I = A \frac{da^n}{dt} \quad (3)$$

When the contact radius is a decreasing function of time then the analysis becomes more complicated since the correspondence principle cannot be applied directly. Recently, however, Lin et al [3] have extended the work by Hunter [4] and Graham [5] to include adhesion in the viscoelastic contact problem. The focus of this chapter is to analyze the stress intensity factor,  $K_I$ , obtained from using the above two methodologies suggested by Hui et. al. [1,3] for cyclic tests performed on styrene-butadiene latex films. We further compare our results for crack growth with the empirical relation by Maugis and Barquins [6]. This simple dependence of fracture energy on crack opening velocity given by,  $G = W(1 + (a_T V)^{0.6})$  is shown to be inapplicable. Here  $G$  is the strain energy release rate,  $W$  the work of adhesion,  $V$  the crack velocity and  $a_T$  the William-Landel-Ferry shift factors. The exponent is not fixed at 0.6, but it varies between **0.2** and **0.8** for most polymers analyzed [6]. A new relationship between stress intensity during unloading,  $K_I$ , normalized by the stress intensity at debonding initiation,  $K_{I,m}$ , and crack opening velocity is then proposed which is similar to the relationship proposed by Maugis and Barquins except for two aspects. Their universal relationship is in terms of a strain energy release rate or a fracture energy,  $G$ , whereas we report our results in the form of a stress intensity functional,  $K_I$ . Their exponent is close to 0.6 whereas our exponent is about **2** for the particular latex analyzed. We further show that this relation is also independent of contact geometry.

## 7.2 Experimental details

The samples were carboxylated styrene-butadiene copolymer latexes provided by the Specialty Polymers Division of Omnova Solutions, Inc. They differed primarily in their glass

transition temperatures, which were in the range  $-20\text{ }^{\circ}\text{C}$  to  $+28\text{ }^{\circ}\text{C}$ . Thick films of the aqueous suspension were cast onto Mylar substrates followed by drying in air, washing in distilled water and heating to about  $50\text{ }^{\circ}\text{C}$  above  $T_g$  to insure complete film formation. The final film thickness was  $\geq 300\text{ }\mu\text{m}$  and were several orders of magnitude thicker than the deepest indentations. The root-mean-square surface roughness of the films was determined by scanning probe microscopy to be less than  $10\text{ nm}$ . The bulk viscoelastic properties were characterized by measuring the shear modulus over the frequency range  $0.01\text{ Hz}$  to  $30\text{ Hz}$  for temperatures of  $5, 25, 35, 60,$  and  $80\text{ }^{\circ}\text{C}$  and will be discussed in detail elsewhere. The time-dependent relaxation modulus  $E(t)$  was calculated from this data using time-temperature superposition and assuming a Poisson ratio of  $0.5$ . For these materials, instantaneous relaxation moduli  $E_o(t \rightarrow 0)$  were near  $1\text{ GPa}$  and long time storage moduli  $E_{\infty}(t \rightarrow \infty)$  were in the range  $0.1\text{-}0.5\text{ MPa}$ . The creep compliance  $\phi(t)$  is a material property a viscoelastic material and is used in the analysis below. It describes the time-dependent response of the strain to a change in the applied stress;  $\phi(t)$  can be calculated directly from  $E(t)$  since their Laplace transforms are related by  $\hat{\phi}(s) = 1/s^2 \hat{E}(s)$ .

Contacts were controlled with a predetermined loading/unloading cycle  $P(t)$ . The displacement (also called deformation or depth of penetration)  $h(t)$  of the rigid probe was measured continuously during the contact cycle. Thermal drift of about  $0.05\text{ nm/s}$  limited measurements times to less than about  $800\text{-}1000\text{ s}$ . Cyclic tests began with the probe out of contact, which allowed us to achieve tensile loads during the unloading portion of the cycle. The load was applied using a predetermined loading/unloading cycle and the displacement measured simultaneously. The load was increased at a constant rate  $dP/dt$  to a predetermined maximum value  $P_{max}$  in a time interval  $t_c/2$  that was varied between  $0.02\text{ s}$  and  $1000\text{ s}$ ;  $t_c$  is the total contact time. During the compressive portion of unloading the rate was  $-dP/dt$ . During the tensile portion, the load was determined entirely by the extension of the indenter springs and could not be controlled by the feed-

back system. All measurements were carried out at room temperature ( $\approx 25\text{ }^\circ\text{C}$ ). In this paper we will focus our analysis on the cyclic tests. The creep test analysis has been discussed in the previous chapter.

Since all the theoretical models assume that the contacts have linear viscoelastic response, it is important to ensure that the strains and strain rates were low enough to avoid any plastic deformation. This was done as follows. First, a cyclic loading-unloading experiment was carried out at a high loading rate of  $\sim 0.024\text{ N/s}$ . Second, the probe was held above the location of this indent for 2 hrs. After the rest period, the loading-unloading cycle was repeated. The displacements at initial contact, the slopes of the loading curves, the pull-off forces, and areas under the adhesion hysteresis curves were compared for the two cycles. These quantities were always identical within the experimental precision. Imaging studies demonstrate that lateral drift is negligible over tens of hours. To eliminate the possibility of vertical drift during the wait, the displacement to reach initial contact was determined at several symmetrically located nearby points. Their average was the same as the initial displacement to contact. Thus, we conclude there is no significant residual plastic deformation under the experimental conditions used in the experiments reported here.

For each latex, sets of load-displacement curves were obtained over a wide range of loading rates. In the case of the Berkovich tip, indents were made deeper than **300** nm to minimize effects of tip rounding. In the case of the spherical probe, indents were shallower than  $2\text{ }\mu\text{m}$  so that its profile could be approximated as a paraboloid in the analysis. Indents were also substantially deeper than 10 nm to minimize effects due to surface roughness and possible variations of sample stiffness near the surface. Measurements of the near surface stiffness of latex 1 were made at Naval Research Laboratory using the force modulation technique described in the introduction. The measured stiffness was found constant for indentations deeper than about 10 nm. Whether the

near surface variation is due to surface roughness or true variation in creep compliance is not known.

The results for a Berkovich indenter are shown in Figures from previous chapters. The adhesion hysteresis, i.e., the energy dissipated during a loading cycle is measured by the area enclosed by the cycle. For latex #4, this hysteresis is smallest for the shorter contact times then increases as the contact time increases before finally decreasing at very large contact times. In all experiments except for the very fast ones, the probe continues to penetrate into the latex after the maximum applied load is reached.

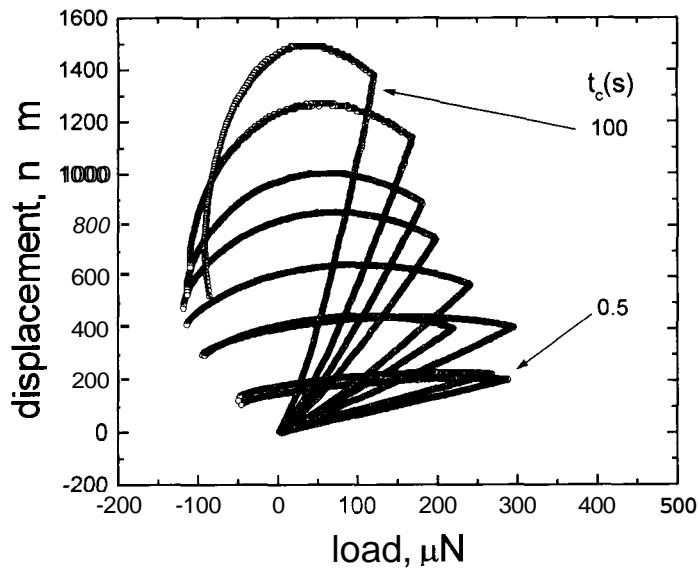


Fig 7.1 Load vs. displacement curves (adhesion hysteresis curves) from cyclic tests done on latex # 4 with a spherical probe. The adhesion hysteresis increases first as the contact time increases before finally decreasing at very large contact times.

The maximum displacement occurs during the unloading portion of the cycle. This is precisely the behavior expected for long range viscoelastic creep. Fig. 7.2 (a) plots the portion of the penetration that occurs after maximum load as a function of inverse contact time;  $\Delta\delta$  is the difference between the maximum displacement and the displacement at maximum load. **Also** shown in the insert is  $\omega_{\max}$ , the frequency at which the bulk  $\tan \delta$  has it maximum value.

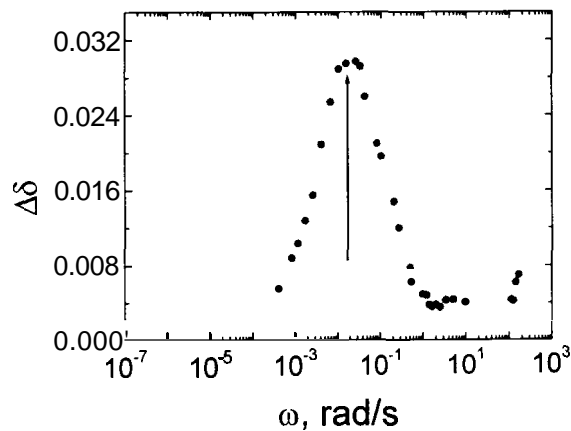


Fig. 7.2 (a) Relative increase in contact depth after load starts decreasing from cyclic tests done on latex # 4.

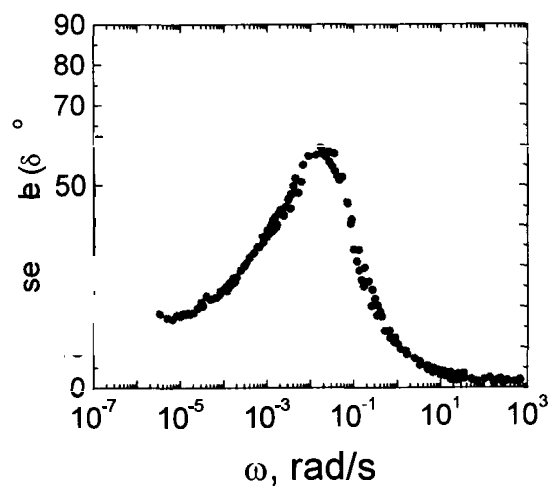


Fig. 7.2 (b) Phase angle as a function of oscillation frequency from dynamic mechanical tests done on latex # 4 with a parallel-plate rheometer.

For latex 1,  $\omega_{\max} \approx 40$  s at 24 °C, which can be seen from Fig. 7.2 (b). Therefore the material is most dissipative when the experimental contact time is closest to the most dominant relaxation time constant of the material [7]. Creep effects should be largest at  $\omega_{\max}$  and decrease on either side. As expected,  $\Delta\delta$  peaks at  $1/t_c$  close to  $\omega_{\max}$  for latex 4. The largest tensile (negative) load achieved is the *effective Pull-Offforce*,  $P_{\text{eff}}$ . Unlike the more familiar case of a spherical

probe, the displacement is always positive at  $P_{eff}$ . This is a general property of conical indenters even for elastic materials. Using the approach of Maugis, it is straightforward to show that pull-off occurs when  $P_{el} = -54W^2 \tan^3 \alpha / \pi E^*$  and  $h_{el} = +3W \tan \alpha / E^*$  where  $a$  is the enclosed half-angle of the cone. The Berkovich indenter is frequently approximated as a cone in the indentation literature and we use this approximation in the analysis below.

The general features of data obtained with the spherical probe are the same as discussed above for the Berkovich probe and show typical data obtained with the spherical probe. In contrast to the Berkovich data, the effective pull-off occurs at displacements near zero as is typically observed for elastic contacts.

### 7.3 Results and Discussion

Figure 7.1 shows load vs. displacement curves from indents made on latex # 4 with a spherical probe at different contact times. A delayed maximum in the contact depth can be seen in all the curves and is predominant in the 40s indent. These delayed maxima are due to long-range creep effects occurring on a length-scale is comparable to the contact radius  $a$  [1,2,3]. Such creep effects are expected to be most pronounced when  $t_c$  is comparable to a characteristic relaxation time  $T$  of the viscoelastic sample. Fig. 7.2 (a) shows the fractional increase in displacement beyond maximum load  $\Delta \delta = (\delta_{max} - \delta_{F,max}) / \delta_{F,max}$  as a function of inverse contact time.  $\Delta \delta$  increases significantly as the contact time decreases. Calculations based on the Ting model suggest that  $\Delta \delta$  should reach a maximum when  $1/t_c \approx \omega_{max}$  where  $\omega_{max}$  is the measured frequency at which the loss tangent has its maximum. The arrow in the insert indicates  $\omega_{max}$ .

Fig. 7.3 shows the behavior of stress intensity factor for the different loading histories in Fig 7.1. The details for calculating  $K_I(t)$  from the load-displacement data are shown in sections 3.2.2. and 3.2.3.  $K_I(t)$  is calculated for the bonding part first followed by the debonding part.

Stress intensity, at the initial point of contact is determined by the glassy modulus of the material, which is about 1 GPa in case of latex 1. For a work of adhesion of about  $0.066 \text{ J/m}^2$ , and a glassy modulus of 1 GPa the instantaneous stress intensity should be about  $11000 \text{ N/m}^{-3/2}$  as shown in the figure below by a horizontal dashed line.

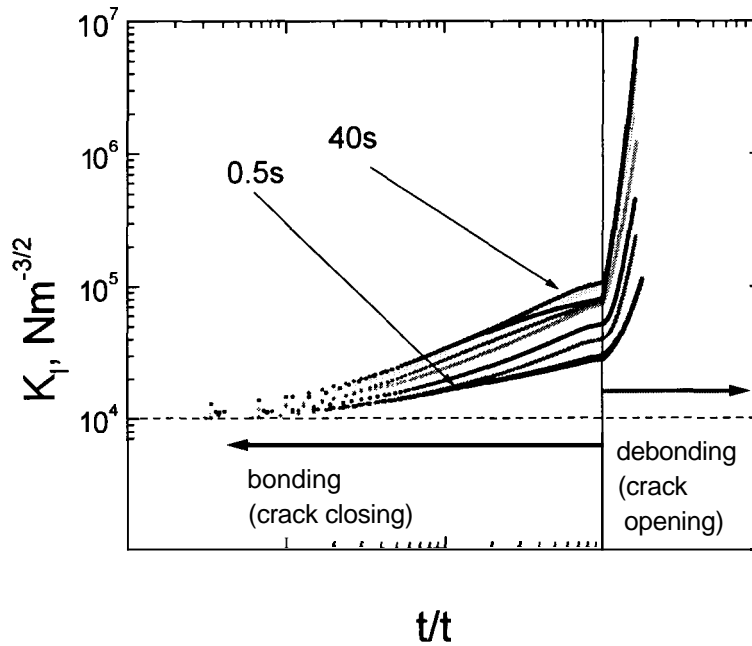
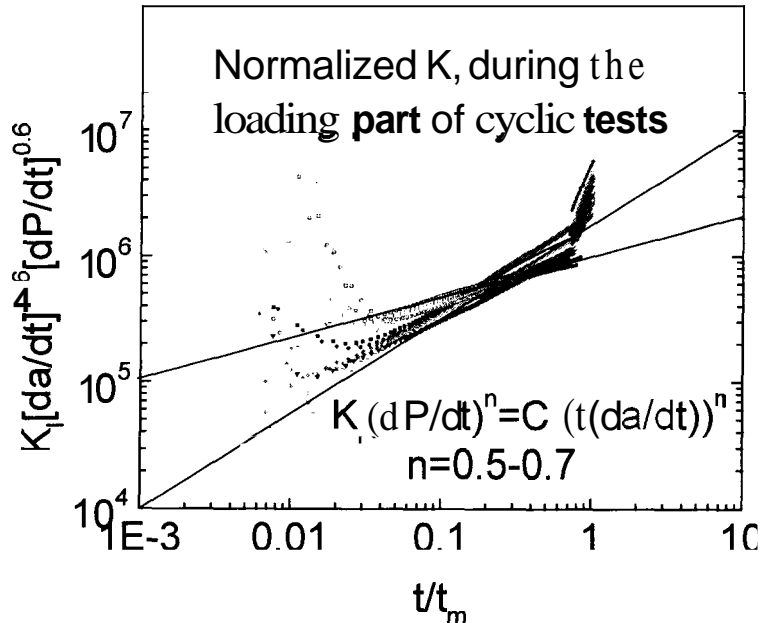


Fig. 7.3 Stress intensity factor for all cyclic tests for the entire bonding-debonding cycle.  $K_I$  increases from its glassy value and reaches its maximum value at contact rupture. The equations used for calculating  $K_I(t)$  from the load-displacement curve are given in sections 3.2.2 and 3.2.3. Dashed line indicates the instantaneous value of stress intensity,  $K_I$ .

All curves in Fig. 7.3 are approaching this initial value of stress intensity as  $t \rightarrow 0$  irrespective of their loading histories implying that crack will propagate at high velocities. The stress intensities are plotted against normalized time ( $t/t_m$ ), where  $t_m$  is the time at maximum displacement. In all the curves it can be seen that the rise in  $K_I(t)$  becomes gradual as the crack closing velocity approaches zero. At  $t/t_m = 1$ , when the contact radius starts decreasing, debonding initiates. For all of the latexes studied,  $K_I$  lies in the range  $7 - 24 \text{ kN/m}^{3/2}$  for both probes. For a given load, the  $K_I$  for the Berkovich indenter increase more slowly and reach smaller values than for the spherical

indenter. At shorter times, the behavior is very different. For the Berkovich indenter,  $K_I$  decreases initially, passes through a minimum, and then rises slowly. For the spherical indenter,  $K_I$  increases over the entire range. Figure 7.4 shows  $K_I$  normalized by the crack propagation velocity and the loading rate, plotted as a function of normalized time,  $t/t_m$ . The curves show similar trend and follow the functional form given by (1). The stress  $\sigma$  at the periphery of the contact can be estimated since, for a simple crack,  $\sigma = K_I/\sqrt{\pi L}$  where  $L$  is the crack length. Using values of  $L$  estimated by the Schapery theory, we find  $\sigma$  to be on the order of a few hundred MPa. Since  $h$  (and  $a$ ) are functions of  $K_I$ , they could, in general, depend on the entire loading history. If this were the case, there would be little utility in using  $K_I$  to describe the adhesion of the contact. However, if the relationship between  $h$  and  $K_I$  can be approximated by a simple functional relationship, then  $K_I$  can provide a useful alternative to the normal approach that emphasizes surface energy.



**Fig. 7.4** Normalized stress intensity factor for the bonding phase of the cyclic tests. Stress intensity can be expressed a function of crack propagation velocity and the loading rate.

Empirically, we find that all of the creep data for all of the latexes and both indenter shapes have the approximate functional form given by equation (1). We observe that, when the stress intensity functional is normalized by the crack velocity and loading rate a universal relationship is obtained. This enables expressing crack velocity in terms of stress intensity and loading conditions for the entire loading cycle. The relationship between crack velocity and stress intensity functional is unique once a cohesive zone model is established.

$$K_I = \left( \frac{d\delta}{dt} \right)^n \left( \frac{dP}{dt} \right)^{-n} t^s \quad (1)$$

where  $n$  is close to **0.6** and  $s$  varies from 0.45-0.75 for the materials studied here. This is demonstrated in the previous chapter too. The overall trend of the data is clearly described by equation (1). However, within the band of data there are weaker trends and there are digressions in the early part of the contact. There is clearly a marked departure from this trend during the initial part of the curves. This can possibly be due to inaccuracy in determining the exact point of contact. It is also seen that data obtained with a Berkovich probe tends to lie higher than that obtained with a spherical probe. Data for higher loads lies above data for lower loads. Data for high  $T_g$  samples lies below that of low  $T_g$  samples. A discontinuity in the curves exists at the point of maximum load. It should also be noted that once the crack starts slowing down, the quasi-steady state approximation made in this analysis becomes invalid and this restricts our ability to model the transition from positive to negative  $da/dt$ . During unloading, the crack opening velocity increases so does the stress intensity till final detachment. This relationship is unique for a given cohesive zone. Therefore one can then characterize the adhesion based on the relationship between crack velocity and stress intensity.

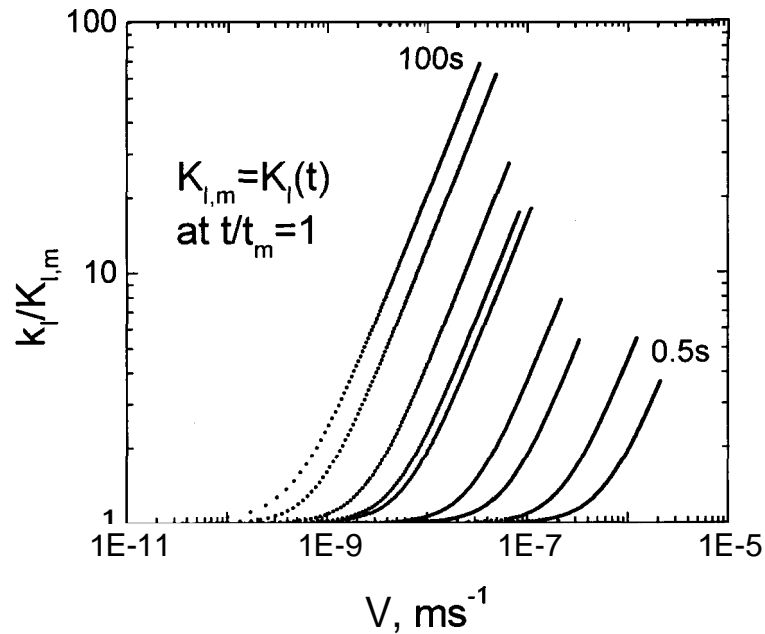


Fig. 7.5 Stress intensity during the debonding part,  $K_I$ , normalized by the value of stress intensity at the beginning of unloading ( $K_{I,m}$ ), plotted as a function of crack velocity,  $V = da/dt$ .

It should be noted that the stress intensity  $K_I(t)$  is completely determined from the bonding phase of the contact and controls the local stress field near the edge of the contact. Two bodies with identical material properties and contact zones of different sizes will have identical stress fields near the edge of the contact as long as the stress intensity factors are equal. However, the same cannot be said about the deformation of a material point near the contact edge since deformation is dependent on the stress history. Thus the stress intensity factor is a key parameter in describing adhesive viscoelastic contacts. It should also be noted that since stress intensity is a continuous function for the entire contact cycle.

As suggested by Hui et al., a relation between debonding rate and stress intensity for the debonding phase may exist. The cohesive zone parameters,  $W$  and  $h_c$ , have been specified using the procedure described in chapter 5 where creep effects were restricted to the crack tip, i.e., near the contact edge only.

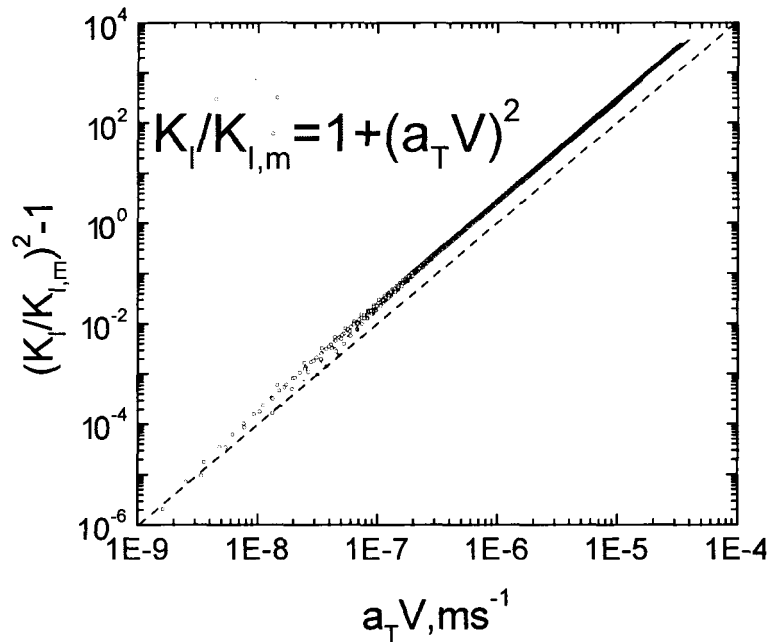


Fig. 7.6 Debonding stress intensity,  $K_I$ , expressed in a universal form, as a function of crack velocity,  $V$ , which has been shifted using the WLF shift factor,  $a_T$ . The load-displacement data used was from the spherical probe (Fig. 7.1).

We use the procedure described by Hui et al. [1,3] to propose relationship between stress intensity during unloading,  $K_I$ , normalized by the stress intensity at debonding initiation,  $K_{I,m}$ , and crack opening velocity. This relationship is similar to the relationship proposed by Maugis and Barquins. In the experiments done by Maugis and Barquins, before unloading the indenter or before peeling, the contact was allowed to attain complete equilibrium and hence their unloading fracture energies are normalized by the equilibrium work of adhesion. In our experiments, as unloading starts the contact is still not in complete equilibrium since the crack velocity is not exactly zero. The crack velocity undergoes a rapid transition from positive to negative. Therefore we normalized unloading stress intensity with respect to its value at debonding initiation ( $K_{I,m}$ ). Figure 7.6 shows the behavior of debonding stress intensity for all the curves in Fig 7.1. The functional form that represents all the curves is given by,

$$K_I^2 = K_{I,m}^2 (1 + (a_T V)^2) \quad (4)$$

where  $V$  is the debonding crack velocity and  $a_T$  is the WLF shift factor. The curves in Fig 7.5 have been shifted with respect to the highest frequency indent to yield Fig 7.6. This relationship is independent of contact geometry. In spite of having the same general trend, the curves still differ in terms of the magnitude of stress intensity. It should be noted that the debonding stress intensities are in general greater for a conical indenter for similar indent depths and contact times. This can be explained by examining the probe shape closely. For a conical probe, during debonding higher crack velocities can be attained when compared to a spherical probe for the same contact rate of change of contact depth. For two different loading histories that give the same stress intensity factors at some instant must have the same crack velocity at that instant. This high value of  $K_I$  is therefore due to the higher value of crack velocity.

#### 7.4 Conclusions

Cyclic loading/unloading experiments were carried on three styrene-butadiene copolymer latexes with a nanoindenter. Hysteresis occurs because of unrecoverable work done during each cycle. For the latexes analyzed the amount of energy dissipated in each cycle increases with increasing loading rate for the range of loading rates that could be achieved with the nanoindenter. Delays between the time of maximum load and maximum displacement demonstrate the presence of bulk viscoelastic creep, which is significant for certain ranges of contact time. Delayed maxima are not observed if the loading rate is small enough. These data are used to verify an extended JKR model proposed recently by Johnson. This model combines classical JKR theory with a fracture mechanics model of crack initiation and growth in linear viscoelastic materials due to Schapery. The major assumption of the model is that viscoelastic effects are limited to the crack tip. Longer-range creep effects are ignored. This limits applicability of the model to low loading rates. The extended JKR model provides excellent fits to the data obtained at low loading

rates. The stress intensity factor  $K_I$  is a parameter that represents the reaction of the failure zone on the surrounding material. The stress intensity factor is the most information a contact mechanics measurement can obtain about the mechanism of failure at the crack tip. Once  $K_I$  is known, the response of the crack to changing externally applied stresses is completely determined regardless of the complexity within the fracture zone.

The HBK[3] model provides the framework to carry out this analysis for axisymmetric adhesive contacts involving linear viscoelastic materials. In general,  $K_I$  can be a complex functional of the history of the contact. If this were always true, each contact situation would be a special case. However, the creep and cyclic studies with different probe shapes presented here suggest that  $K_I$  can have a simple form. Specifically, for loading we show empirically, that  $K_I$  can be approximately describe by a simple function of the displacement (deformation) and time for the entire set of bonding data. The dependence on probe shape was found to be weak. The behavior of stress intensity during the decreasing contact area (debonding) can be presented in a form similar to the one by Maugis and Barquins except for the value of the exponent. We observe that the debonding stress intensities can be expressed as a function of the crack opening velocity in a form that is independent of the contact geometry and follows the same time scale shifting given by the WFL factor.

It should be noted that during deformation, energy is dissipated in the form of viscous absorption as well as heat absorption. Recently, the total energy absorbed by latexes before failure in a tensile test was measured using a differential gas pressure stretch calorimetry [7]. We have neglected any conversion of input work into heat energy. The extent of deformation (strain amplitude) in our nanoindentation analysis is much smaller than the high strains generated in regular tensile tests and, therefore, this assumption is reasonable.

## 7.5 **References for chapter 7**

1. Hui, C.-Y., Baney, J. M., Kramer, E. J. *Langmuir* 1998, 14, 6570.
2. Giri, M., Unertl, W. N., Bousfield, D.W. *Tribology Letters*, 2000, 9, 33.
3. Lin, Y. Y., Hui, C.-Y., Baney, J. M. *J. Phys. D: Appl. Phys.* 1999, 32, 2250.
4. Hunter, S. C. *J. Mech Phys. Solids* 1960, 8, 219.
5. Graham, G. A. C. *Int. J. Eng. Sci.* 1967, 5, 495.
6. Maugis, D., Barquins, M. *J. Phys. D: Appl. Phys.* 1978, 11, 1989.
7. Agarwal, N., Farris, R. J. *J. Coatings Technology*, 1999, 71, 896, 61-72.

## Chapter 8. Summary of Linear Viscoelastic Fracture Studies

### 8.1 Conclusions

A method for predicting the work of adhesion of viscoelastic materials using a fracture mechanics approach is presented. Two different models are used to understand the deformation behavior of these materials. Both methods rely on the presence of a small cohesive zone or the process zone in the immediate vicinity of the contact. In the first method, as proposed by Johnson [1], viscoelastic dissipative effects are assumed to be limited to the cohesive zone whereas the remainder of the material is assumed to be in a relaxed state. This method allows for a fairly accurate prediction of the material work of adhesion and the effective range of the cohesive zone if the material compliance is known. Once the cohesive zone parameters have been established, we can then describe the deformation behavior of any material under any given loading condition using the theory proposed by Hui, Baney, Lin and Kramer [2,3]. They propose the use of a stress intensity factor,  $K_I(t)$ , instead of strain energy release rate,  $G(t)$  for understanding viscoelastic contacts. We have computed the stress intensity factors for various viscoelastic styrene-butadiene latexes using their theory and expressed it as a function of the bonding and debonding velocity. The stress intensity factor contains information about the cohesive zone stresses and their distribution and hence is an important parameter to gain deeper insight of the cohesive zone processes. We finally compare the results of this continuum mechanics approach to theoretical prediction for a viscous chain desorption and comment on the similarities.

### 8.2 Future extensions

We have investigated the deformation of styrene-butadiene latex films in our work. The work should be extended to other viscoelastic materials. In our experiments we used diamond probe of different shapes for indentation purposes. Therefore, the work of adhesion and the dynamics of contact are limited to the surface chemistry, contamination of the probe. In order to test

and extend the applicability of this method in understanding the cohesive zone, different probe chemistries have to be used.

One way would be to simply attach a glass particle or a polystyrene bead to the diamond surface and then conduct adhesion experiments at sufficiently slow rates in order to make sure that the particle does not detach under the application of a small force. These results can then be compared with the results of only diamond on latex. The next step would be to modify the glass surface by depositing a Self-Assembled-Monolayer (SAM) with different terminal functionality. Indenting with this modified surface would enable direct comparison of this continuum mechanics approach with polymer chain dynamics prediction. Experiments like this have been conducted on a macro scale using a JKR apparatus and on a nanoscale using an Atomic Force Microscope, but no work has been done on a smaller micro scale where both nano and macroscale processes take place simultaneously.

Experiments should also be conducted in a liquid environment. Changing the characteristics of the liquid environment such as pH, ionic strength would influence the orientation of polymer chains on the glass bead and therefore affect the fracture behavior.

### 8.3 Reference for chapter 8

1. Johnson, K. L *Microstructure and Microtribology of Polymer Surfaces*, eds. V. V. Tsukruk and K. J. Wahl, American Chemical Society, Washington, D.C., **2000**.
2. Hui, C.-Y., Baney, J. M., Kramer, E. J. *Langmuir* **1998**, 14,6570.
3. Lin, Y. Y., Hui, C.-Y., Baney, J. M. *J. Phys. D: Appl. Phys.* **1999**, 32, 2250.

## PART III : Dynamic Contacts to Visco-Elasto-Plastic Coating Composites

### Chapter 9. Contacts to Pigmented Coatings

#### 9.1 Introduction

Mechanical contacts between elastic materials with nanometer to micrometer dimensions are well understood, including the increasingly important role of adhesion as the contact size decreases. For elastic materials, the contact radius  $a$  and penetration  $S$  are uniquely determined by the applied load  $P(t)$ , the elastic properties of the contacting materials, and the thermodynamic work of adhesion  $W$ . Fits of  $a$  vs.  $P$  or  $S$  vs.  $P$  data to the appropriate theoretical models allows  $W$  and the effective moduli of the contacting materials to be determined.

Contacts involving elastomers and elastic-plastic materials are less well understood but approximate models are available that allow estimates of  $W$  and mechanical properties [1,2,3]. Contacts to viscoelastic-plastic materials are poorly understood. There is very little quantitative data and, no theoretical models that included both elastic-plastic response and adhesion. In this paper, we present a detailed experimental study of micrometer-sized contacts between a rigid probe and three different viscoelastic-plastic composites. These results are analyzed using crack tip creep during decohesion combined with the elastically recovered crown approach proposed by Johnson.

In this paper we show that, viscoelastic styrene-butadiene latex films at high filler content (270%) exhibit limited viscoelasticity,  $E_o / E_\infty \approx 10 - 50$ , along with residual plasticity, which is most likely due to filler (hereafter, pigment) rearrangement in the latex medium. At high pigment volume concentrations (hereafter, PVC) the composite (coating) structure is a three-phase system. The pigment and latex comprise the *two* solid phases whereas the pore structure comprises the vapor phase. The composite is therefore a complex mechanical structure, which is not purely viscoelastic since irreversible changes in the structure are possible at fairly low strains due

to the voids. Analyzing viscoelasto-plastic systems is complicated and has not been completely done in a contact mechanics experiment. It has, however, been shown that during the loading cycle as the applied load increases the contact passes through four regimes [4]. The initial contact is essential adhesive elastic given by the JKR (Johnson-Kendall-Roberts) model, followed by the elastic-plastic regime where the plastic zone size is limited, then the fully plastic regime and, finally, the finite deformation regime. Once the contact enters the fully plastic zone during bonding, the contact load upon withdrawal will show residual plastic deformation. So the debonding analysis has to account for this permanent deformation. A simple analysis proposed by Johnson relates the final contact radius,  $a_f$ , under a load,  $P_f$ , to the hardness,  $H$ , of the material given by  $\pi a_f^2 H = P_f$  [5]. When the load is removed the material recovers elastically and the radius of the recovered crown is given by the simple Hertzian relationship. In our case, since the material is viscoelastic, the initial response is not elastic but time dependent, which can be described by the crack tip creep effects. Commercial coatings are subjected to severe compressive and tensile stresses during industrial processes such as calendering and printing. The following section provides a brief description of these processes and discusses the significance of this work.

## 9.2 Motivation

### 9.2.1 Effective Medium Approach

In order to understand the deformation behavior of multi-component systems such as pigmented coatings containing high pigment volume concentrations we adopt an effective medium approach. In this approach we assume that the entire composite can be approximated as a continuous, homogenous, isotropic solid. The effective medium is assumed to be viscoelastic-plastic. Viscoelastic response is attributed to the presence of latex and also possibly due to the pigment depending on its type and glass transition temperature. The plastic response is attributed to the presence of a yield mechanism. The microscopic origin of this yield mechanism is not yet

clear. The effective medium approach allows us to analyze the deformation behavior of these pigmented coatings using conventional contact mechanics techniques. Modeling enables extracting some useful parameters, such as material yield stress, which sheds more light in investigating the different dissipative mechanisms taking place during coating deformation. “Yield” could be occurring due to collapse of the pores, which would lead to the formation of new surfaces between the latexes or between the pigments and even between the pigments and latex. In this chapter we will first discuss how this work relates to calendering and printing processes. We will then describe results from indentation testing on Coatings containing different pigment types. The parameters used in modeling the hysteresis curves will be reported. In Discussions, we will suggest possible mechanisms, which lead to permanent (plastic) deformation in these coatings.

### **9.2.2 Calendering**

Calendering is a well-known process in which a material is run through rollers into thin sheets or to produce a smooth glossy finish. Calendering is used for different materials like cloth, polymers, ceramics and paper as well as paperboard. Conventional wisdom of the calendering process suggests that surface finish in the paper is produced by paper slipping against the rolls. More recent knowledge reveals that adhesion between the roll and the sheet causes the outgoing sheet to have a surface that is a replica of the roll surface. Hence, if a smooth sheet is desired, rolls with smooth surface have to be used [6]. In soft nip calendering, the side of the paper that is adhered to the roll undergoes substantial smoothening and gloss action because paper being a porous compressible structure can undergo plastic collapse just by compaction without the need for shear forces unlike metals. Plastic deformation of paper as a result of thickness compression can be produced in paper by a simple collapse of the fiber network [7] and by collapse of the pore structure in case of coatings [8]. Hence, shear does not play a role in the plastic compaction of paper when it is under the constrained geometry of the nip, but adhesive shear forces play a role at the exit, especially for coatings. Exit shear places demand on the inherent strength of the sheet

or the coating on the basesheet since it must withstand the adhesive shearing force without rupturing or sticking.

Modeling of localized deformation of paper in the thickness direction has not yet been done. Thermo-viscoplastic deformation of paper has been known to occur under the calender nip, but has not yet been modeled. Processes such as coating, printing, folding and pressing depend on the out-of plane (thickness) response of paper. Furthermore, the out of plane behavior such as edge wise compression is influenced by the material constraints in the thickness direction. Hence, it is important to understand the compression behavior of paper as well as coatings on a localized scale. In our work we attempt to address issues which deal with compressive mode behavior of viscoelastic, viscoelasto-plastic coatings. Viscoelastic properties of polymers are a function of both time and temperature. These properties need to be determined at the process conditions that the polymer is subjected to, in order completely understand its behavior. The WLF time temperature superposition principle has been used to estimate the properties of a polymer under experimentally inaccessible conditions [9]. Coatings have been prepared on Teflon™, dried, peeled and their dynamic mechanical properties were determined using torsional rectangular geometry on a Rheometrics RDS-II instrument. The purpose was to relate coating viscoelasticity to the end use performance by keeping other parameters constant [10]. Viscoelastic properties of paper coatings influence the extent of gloss improvement, stiffness and crack /fold resistance, sticking during calendering and blister resistance during offset/rotogravure printing.

During calendering, paper undergoes deformation as it is compressed in the calender nip. This compressive energy can either be stored or dissipated depending upon the coating characteristics. After the compressive load has been removed, the coating will either return to its original state with no change in gloss if its perfectly elastic, or permanently deform if its elastic-perfectly plastic resulting in a flatter, smoother surface with increased gloss. At high PVC the void fractions also play an important role in the coatings overall mechanical behavior [11]. The final de-

formed structure of the coating will therefore depend on elasticity of the pigments, viscoelasticity of the latex and the coating pore structure.

### 9.2.3 Printing

As mentioned earlier, it is important to understand the compressive behavior of paper to better explain its behavior in further processes such as coating and printing. For similar reasons, it is important to understand the tensile strength of coatings in order to explain their resistance to picking during printing. For instance in offset printing, ink is transferred to a blanket first and then from the blanket on to the coated surface. At the nip, high tensile stresses (tack force) are generated due to the extensional behavior of polymers present in ink, which are capable of rupturing the coating structure [12]. Surface features, such as pore structure, roughness and pigment distribution as well as orientation along with surface chemistry (latex and pigment interactivity or solubility with the ink vehicle) and surface mechanics (viscoelastic and viscoplastic behavior) determine the performance of the coating in impact printing [13]. In our work we intend to analyze the compressive as well as tensile behavior of commercial pigmented coatings using recent theoretical developments in contact and fracture mechanics of viscoelasto-plastic materials.  $\text{CaCO}_3$  coatings have been shown to perform better in the printing press and investigators have explained this by examining the stress-to-failure of the coatings as well as the failure mechanism [14,15,16].  $\text{CaCO}_3$  coatings show high stress-to-failure than Clay coatings. We suggest that it is the viscoelastic dissipative mechanism in  $\text{CaCO}_3$  coatings, which provides the resistance to failure during compression or tension. Coatings containing  $\text{CaCO}_3$  were more viscoelastic, and therefore more resilient to z-direction failure.

## 9.3 Experimental

Coating formulations were made by mixing commercially available polystyrene plastic pigment pigments (provided by Dow Chemical Company, Midland, Michigan), Clay (provided

by J. M. Huber) and ground  $\text{CaCO}_3$  (provided by IMERYYS Corp.) separately with carboxylated styrene-butadiene latex (provided by Omnova Solutions Inc., Performance Chemicals Division, Akron, OH  $T_g$  0°C). Coatings with pigment volume concentrations (PVC) ranging from 25-75% were made, but only the high PVC were examined in this paper. Table 1 gives composition of each coating. Coatings in aqueous form were cast on Mylar using a draw down coater and dried in the oven at 80°C for 5 minutes. The final thickness of these films was 0.5-1 mm. Real coatings are 10-20  $\mu\text{m}$  thick and therefore these results must be applied with caution.

loading #	Latex type	Pigment type	PVC (%)
1	Carboxylated <b>SB</b> Latex, $T_g$ 5°C, 130 nm particle size, medium crosslinking	Polystyrene plastic pigment (avg. size 450 nm: monodisperse) Trade name: DOW PP 723™	80
2	Carboxylated <b>SB</b> Latex ( $T_g$ 5°C), 130 nm particle size, medium crosslinking	J. M. Huber Clay (90% finer than 2.5 $\mu\text{m}$ ) Trade name: Covergloss™	75
3	Carboxylated <b>SB</b> Latex ( $T_g$ 5°C), 130 nm particle size, medium crosslinking	$\text{CaCO}_3$ from IMERYYS (isometric particle of size with equivalent spherical diameter between 100- 1000 nm) avg. value- 300 nm Trade name: Carbital 90™	72

Table 9.1. Description of the pigmented coatings

A series of PS/latex coatings with PVC 0, 20, 50, 75 and 85 was also made. The root-mean-square roughness of the films, as measured with contact mode atomic force microscopy (AFM), was typically 80-100 nm over areas of several square micrometers. AFM images typically show the surface structure and alignment of pigments. Figure 9.1 shows typical AFM images of the PS/Latex coating.

Contacts were made with diamond probes in a nanomechanical testing system (Hysitron PicoIndenter™ mounted on a Park Scientific Instruments CP scan base). In a typical indentation experiment the displacement (also called deformation or depth of penetration)  $\delta(t)$  of the probe penetrating the coating was measured continuously during the contact cycle. Thermal drift of about 0.05 nm/s limited measurements times to a thousand seconds. In our experiments the contact times ranged from 0.5-20s.

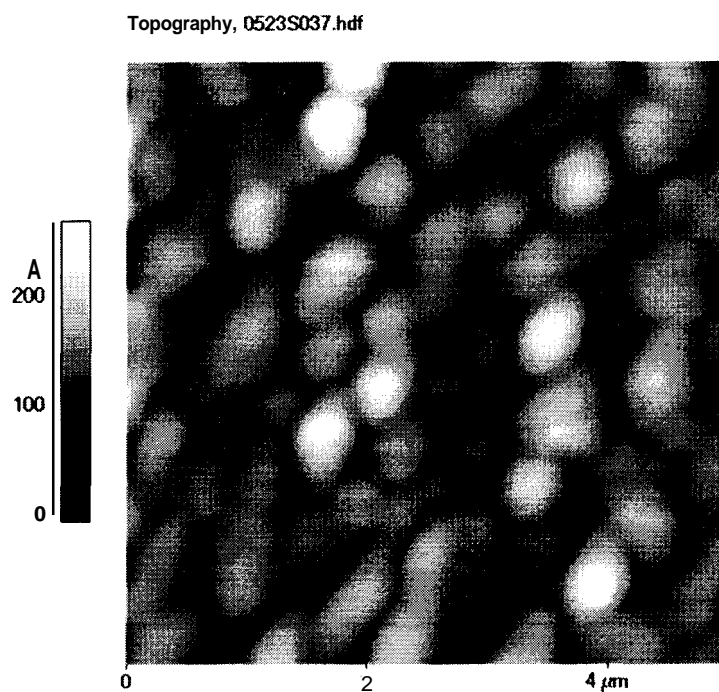


Fig. 9.1 A 5 X 5 Atomic Force Micrograph of the PS/Latex coating (# 1).

In a typical cyclic test, the probe starts about 2.5  $\mu\text{m}$  out of contact, which is necessary to achieve tensile loads sufficient to overcome the probe-sample adhesive forces during the unloading portion of the cycle. In Fig. 5.1b, during segment 1, the probe is brought rapidly into contact, which occurs at point **A**. If the time to achieve contact was less than about 0.1 s, inertial effects cause the indenter motion through air to be nonlinear, as is the case in Fig. 5.1b. Once contact is

achieved, the stiffness of the contact is large enough that inertial effects are no longer important. In segment 2, the load is increased at a constant rate  $dP/dt$  under feedback control to a predetermined maximum value  $P_{max}$ , which is reached at B. During the compressive portion of unloading (segment 3), the rate was  $-dP/dt$ . The unloading rate was not constant during the tensile portion (segment 4), since it is determined entirely by the extension of the indenter springs, which can not be controlled by the feedback system. The total time of contact  $t_c$  could vary between 0.05 s and 20 seconds. The maximum loads used varied between 2000 to 4500  $\mu\text{N}$ . There was no residual plastic deformation in case of the pure latex film, which is not surprising since the latex films are able to sustain high strains (50-200%) without showing signs of plastic yield.

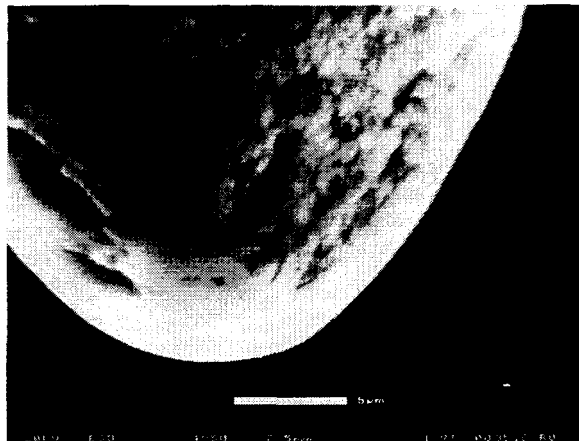


Fig. 9.2 **A SEM** micrograph of the 10 $\mu\text{m}$  spherical indenter. From the scale of 5 $\mu\text{m}$  it can be seen that the approximate diameter of the probe tip is 20 $\mu\text{m}$ . This was also confirmed with **AFM** scans of the indenter tip.



Fig. 9.3 An SEM micrograph of the Berkovich indenter. From the scale of  $1\ \mu\text{m}$  it can be seen that the probe can be approximated as a cone with the same half angle as the Berkovich ( $70.29^\circ$ ). The contact area goes with the contact depth as,  $A=24.5h^2$ . Here  $A$  is the contact area and  $h$  is the contact depth.

This was confirmed by repeated indentation at the same location. We observed no differences between the first and the subsequent indents. All measurements were carried out at room temperature ( $\approx 25\ ^\circ\text{C}$ ). Creep tests were also performed on all samples. In a typical creep test the indenter is brought in contact with the sample at a predetermined set point of  $2\ \mu\text{N}$ . The load is then ramped to a set value in  $0.05\text{s}$  and held constant for about **60s**. Increase in contact depth despite constant load is indicative of material creep, i.e., viscoelastic behavior. The range of frequencies (assuming,  $\omega \approx 1/t$ , ) corresponding to the response times of the indenter is approximately  $0.001\text{-}10\ \text{Hz}$ . Indentation is sensitive to the rheological response of the sample within this frequency interval.

Deformation of pigmented coatings containing  $> 70\%$  elastic organic/inorganic pigments dispersed in a viscoelastic medium of styrene–butadiene latex films have been examined by axisymmetric micro-indentation testing. Typical results are shown in figures **9.7-9.15**. Each test has a loading and an unloading portion. Increasing contact depth corresponds to bonding and decreas-

ing contact depth corresponds to debonding. The load-displacement curves show hysteresis since the bonding and debonding portions do not exactly overlap. There can be many dissipative mechanisms, which contribute to hysteresis. Permanent deformation in the coating structure along with the inherent coating viscoelasticity could be the possible dissipative mechanisms. Therefore, the material is referred to as viscoelastoplastic. For purely elastic-plastic materials the total amount of permanent deformation would correspond to the residual depth at the point of probe detachment during debonding. For purely linear viscoelastic materials, there would be no residual deformation, although the material would show time based recovery. For viscoelastoplastic materials, there exists a permanent residual deformation, which is attained after a time based material recovery. The time constant of recovery is governed by the coating's viscoelastic character.

During the loading cycle the indentation stresses were beyond the elastic limit of the material resulting in plastic deformation which was subsequently measured by imaging the indent. The deformation was shown to be permanent by repeated imaging under low loads for over 2000 minutes. The sequence of images is shown in figures 9.4 through 9.6. The first figure on the left-hand side shows indent 5 minutes after the indentation, followed by an image 1000 minutes after indentation and finally an image 2000 minutes after indentation. For all coatings there is still a residual deformation 2000 minutes after the indent, which is indicative of permanent deformation.

At 70% PVC and above the coating is still viscoelastic [14], primarily due to the latex film but the dissipative effects are limited due to the smaller  $E_o / E_\infty \approx 10 - 50$  ratio, where  $E_o$  is the material instantaneous modulus and  $E_\infty$  is the material relaxed modulus. This ratio is about 3 to 4 orders of magnitude for pure latex films and therefore the viscoelastic dissipative effects are higher for contacts on pure latex films. **As** the pigment concentration increases the material relaxed modulus increases and for coating I containing polystyrene particles, at **85%** PVC the coating behaves as a nearly elastic solid at 25°C with a modulus same as that of pure polystyrene (2-4 GPa).

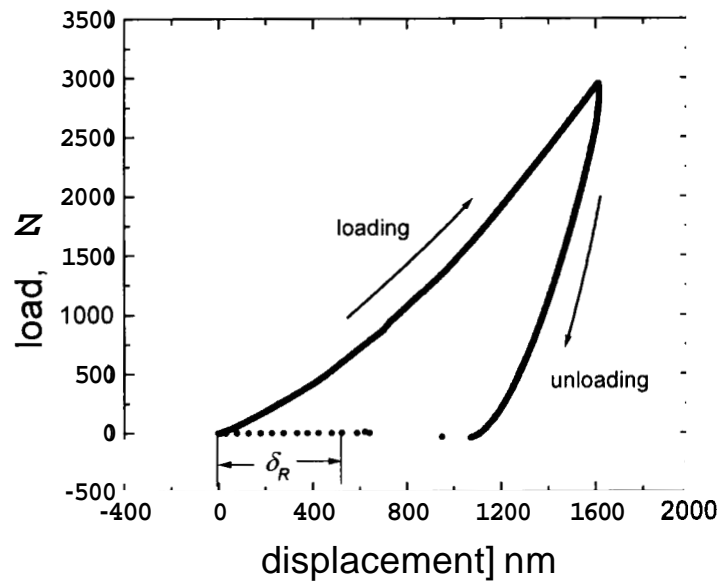


Fig 9.4(a) Load-displacement curve from a typical indent made on coating I with a Berkovich probe. The residual deformation,  $\delta_R$ , can be estimated from imaging the indent over a period of time.  $\delta_R = 580$  nm.

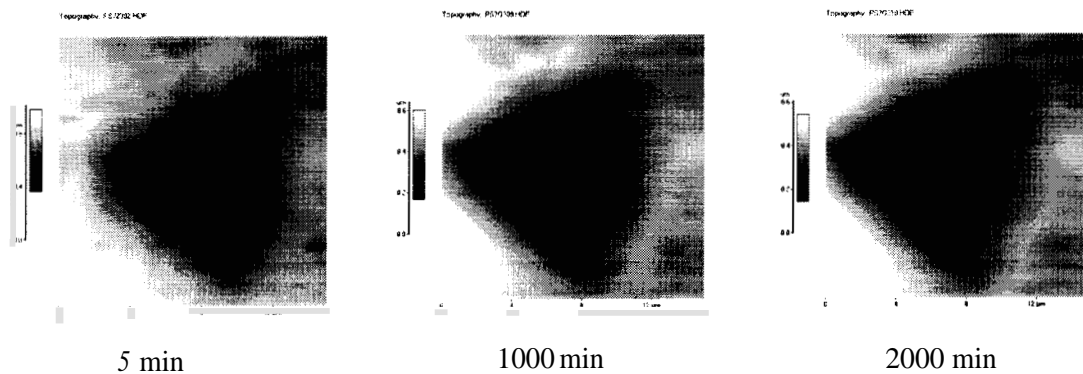


Fig. 9.4(b) Images of the indent made on Coating I (PS). The sequence of images show the evolution of contact depth over a period of 2000 min. The indent recovers initially at a fast rate before attaining an equilibrium value.  $\delta_R$  designates the residual plastic deformation.

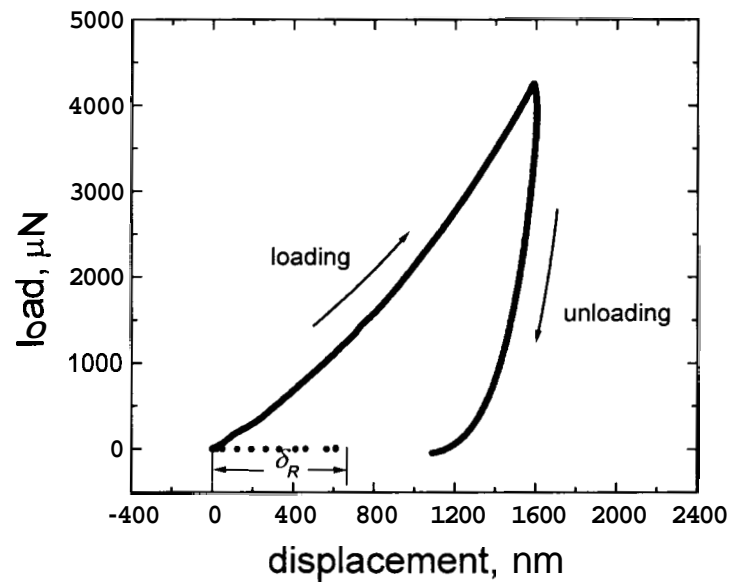


Fig 9.5(a) Load displacement curve from a typical indent made on coating II with a Berkovich probe.  $\delta_R$  is the residual deformation 2000s after indentation.  $\delta_R = 610$  nm.

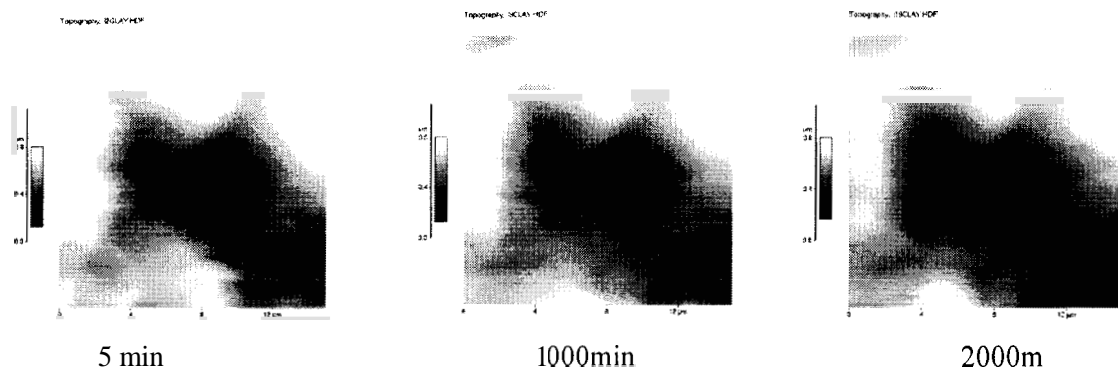


Fig. 9.5 (b) Images of the indent made on Coating II (Clay). These sequence of image shows the evolution of contact depth over a period of 2000 min. The indent recovers initially at a fast rate before attaining an equilibrium value.  $\delta_R$  designates the residual plastic deformation.

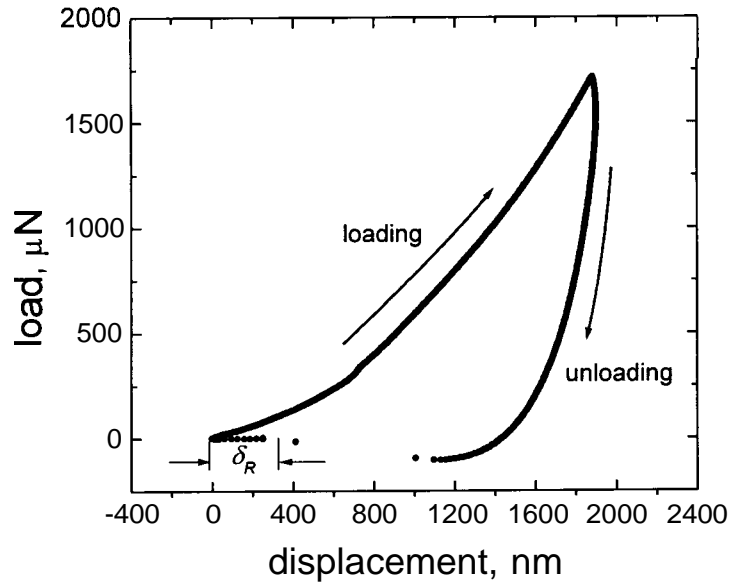


Fig 9.6(a) Load displacement curve from a typical indent made on coating III with a Berkovich probe.  $\delta_R$  is the residual deformation 2000s after indentation.  $\delta_R = 380$  nm.

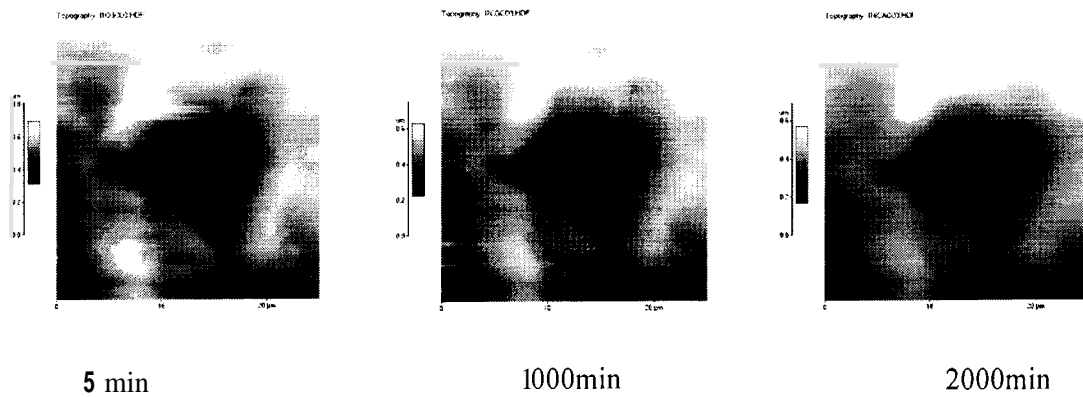


Fig. 9.6 (b) Images of the indent made on Coating III. The sequence of images shows evolution of contact depth over a period of 2000 min. The indent recovers initially at a fast rate before attaining an equilibrium value.  $\delta_R$  designates the residual plastic deformation.

Coating #	$E_{\infty}, E, P$ (Coating compliance parameters)	$E_o$ from Prall [15]	$E_o$ from creep tests	Radius of re-covered crown, $R'$	Average Yield stress, $\sigma_Y$
1	0.52 GPa, 6.2 MPa( $s$ ) <sup><math>p</math></sup> , 0.72	1.5 GPa	0.635 GPa ( $\pm 10\%$ )	15 $\mu\text{m}$ ( $\pm 10\%$ )	2.2 GPa ( $\pm 15\%$ )
2	0.65 GPa, 6.2 MPa( $s$ ) <sup><math>p</math></sup> , 0.72	3 GPa	1.5 GPa ( $\pm 16\%$ )	12 $\mu\text{m}$ ( $\pm 10\%$ )	1.5 GPa ( $\pm 15\%$ )
3	0.1 GPa, <b>0.45</b> MPa( $s$ ) <sup><math>p</math></sup> , 0.72	2.5 GPa	0.3 GPa ( $\pm 10\%$ )	25 $\mu\text{m}$ ( $\pm 5\%$ )	$\geq 2\text{-}5$ GPa

Table 9.2. Mechanical properties as reported with a Dynamic Mechanical Thermal Analyzer (DMTA) and the compressive yield stress values. Coating compliance is given by equation 57 in section 3.3. Here  $E_o$  is the material instantaneous modulus,  $E_{\infty}$  the material relaxed modulus,  $E$  and  $p$  are parameters that define the material compliance function. The radius of the recovered crown  $R'$  and the yield stress,  $\sigma_Y$ , are described in more detail in the results section.

## 9.4 Results

The first step is to investigate creep behavior of the coatings. This was done by performing creep tests. Figure 9.7 show typical results from creep tests performed on the three coatings. The load during the creep tests was 2000  $\mu\text{N}$ . Multiple curves are shown for each Coating to indicate the extent of heterogeneity in the samples. Each curve was obtained at a new point on the surface that had not previously been contacted. In a creep test the material continues to deform after the load has attained a steady value. For purely elastic materials no creep would be observed and for purely viscoelastic materials, creep would be entirely due to material viscoelastic character. For viscoelasticplastic materials, the creep behavior is due to a combination of the material plastic yield as well as due to its intrinsic viscoelastic character.

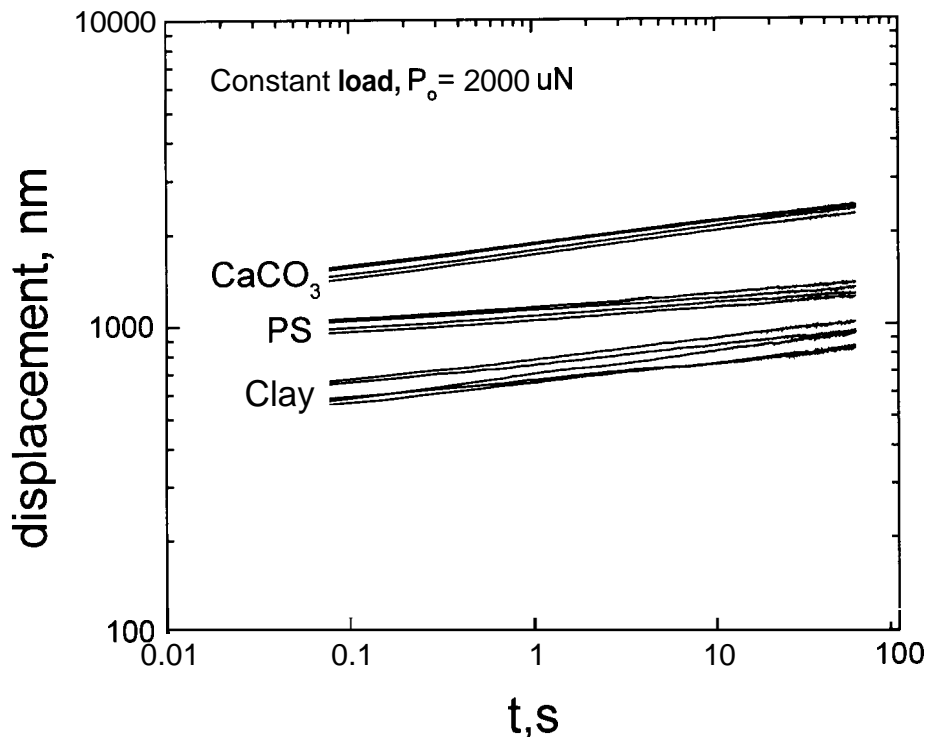


Fig. 9.7 Creep behavior of the different Pigmented Coatings.

All coatings exhibit creep behavior. The creep behavior can be described by a simple functional form represented by,

$$\delta = \delta_0 + C t^m$$

where  $\delta_0$  represents the initial deformation corresponding to  $t=0.05s$ ,  $C$  and  $m$  are fitting constants. Typical values of  $\delta_0$  for coatings I, II and III were 800 nm ( $\pm 5\%$ ), 460 nm ( $+15\%$ ), 1300 nm ( $\pm 7\%$ ), respectively. Typical values of  $C$  for coatings I, II and III were 260 nm/s<sup>-m</sup> ( $\pm 8\%$ ), 210 nm/s<sup>-m</sup> ( $\pm 15\%$ ) and 450 nm/s<sup>-m</sup> ( $\pm 7\%$ ) respectively. Typical values of  $m$  for coatings I, II and III were 0.18 ( $\pm 0.2$ ), 0.13 ( $\pm 13\%$ ) and 0.25 ( $\pm 0.2$ ) respectively. From this information we can also easily calculate the indentation strain rate.

Indentation strain rate is given by,

$$\dot{\varepsilon} = d\left(\frac{\delta}{\delta_o}\right) / dt = \left(\frac{C}{\delta_o}\right) mt^{m-1}$$

If we assume that the material behaves as perfectly viscoelastic within the applied stresses, then we can estimate the instantaneous elastic modulus of the coatings from the initial penetration depth  $\delta_o$ . A simple Hertzian approach describe in chapter **3.1** can be used. The approximate elastic modulus values for coatings I, II and III come out to be **0.635** GPa ( $\pm 10\%$ ), 1.5 GPa ( $\pm 16\%$ ) and **0.3** GPa ( $\pm 8\%$ ) respectively. It will become clear in the results section that these values are underestimates since the stress generated by the applied load exceeds the material yield stress and the material undergoes permanent deformation. The instantaneous modulus of the three coatings in decreasing order is, II>I>III. The plate like structure of clay pigments explains its high modulus. It has been noted earlier that mechanical properties of plate like composites are higher than spherical pigments perpendicular to the direction of particle orientation [17].

Figure 9.8a shows the influence of pigment volume concentration on the creep behavior of coatings. It can be clearly seen that as the pigment concentration increases the amount of creep decreases along with the instantaneous displacement. Fig. 9.8b shows the trend in instantaneous modulus as a function of PVC. Between 50 and 75 % PVC there is a rapid increase in the modulus. These results clearly match with the bulk Dynamic Mechanical Testing results of Prall [15]. Table 2 shows the comparison. Characterizing coatings merely on their viscoelastic behavior is not sufficient to explain their deformation behavior under high strains such as those faced in industrial calendering and printing processes. Analysis of decohesion or debonding is central to the theme of understanding plastic deformation. Hence cyclic test have to be performed and both cohesion and decohesion have to be analyzed in order to completely characterize the material deformation behavior.

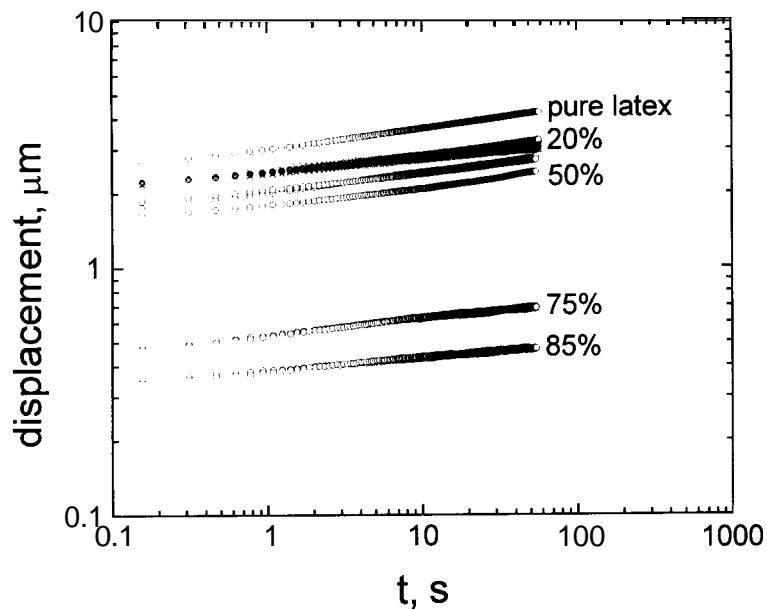


Fig. 9.8 (a) Creep behavior of different pigment volume concentrations of polystyrene pigment under a load of  $1000 \mu\text{N}$ . Multiple curves are shown in order to indicate the heterogeneity in the samples.

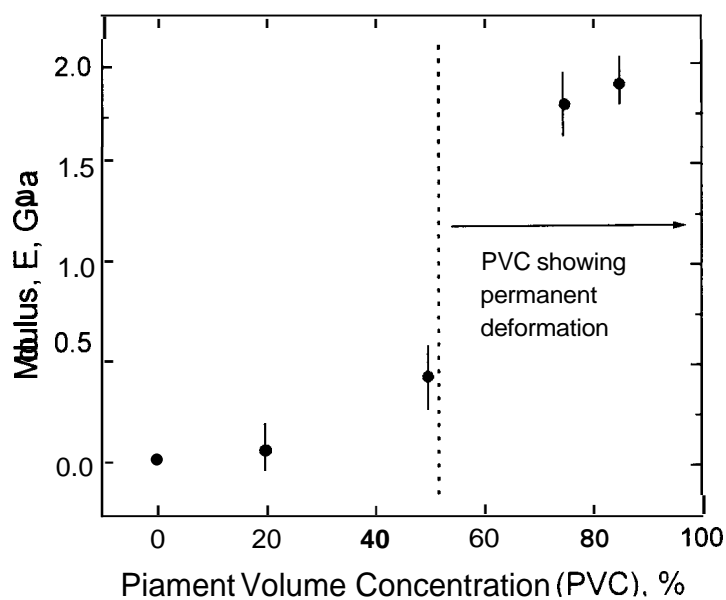


Fig. 9.8 (b) Modulus,  $E$ , corresponding to  $t=0.05\text{s}$  at  $25^\circ\text{C}$  for 0 to 85% PVC for PS coatings. Vertical lines indicate the standard deviation. Permanent deformation was observed in coatings with  $\text{PVC} > 50\%$

Fig. 9.9 shows the evolution of indents made on the three coatings (Figures 9.1, 9.2 and 9.3) over a period of **2000** minutes following a loading unloading cycle. It can be seen that all three coatings show residual, permanent deformation. Coating III shows the least permanent deformation followed by coating I and then coating II. This information is valuable in not only predicting the amount of plastic deformation but also for designing better experiments in order to determine the microscale behind the permanent deformation. The rate of surface recovery depended on the material rheological properties and the extent of yield beneath the surface. Coating III containing  $\text{CaCO}_3$  showed the most percentage recovery of indentation depth, followed by Coating I and finally Coating II. Bulk rheological properties were measured by Prall [18], using small amplitude oscillatory modulations in a Dynamic Mechanical Thermal Analyzer.

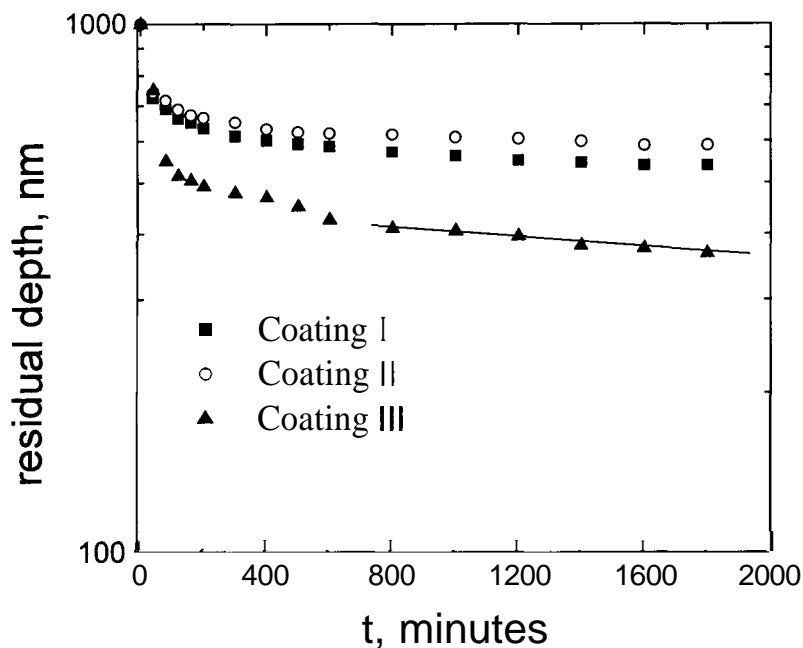


Fig. 9.9 Depth evolution of indents made on the three coatings with a Berkovich indenter. There is an initial rapid recovery, which is governed by the elasticity of the material, followed by a gradual time-dependent recovery, which is governed by the viscoelastic behavior of the material. Coating III shows maximum recovery followed by coating I and coating II respectively.

It can be seen from the curves that there are at least two modes of recovery. In the first 60 minutes there is a rapid decrease in depth. The second mode is applicable for the final part of the recovery curve ( $\geq 500$  min) and can be modeled using a simple power law form. We model the recovery after **600** minutes (line in Fig. 9.9) using a simple power law form represented by,

$$\delta = R t^{-r}$$

where  $R$  and  $r$  are obtained from model fits. The values of  $R$  for coatings I, II and III were 942 nm(min)<sup>r</sup>, **888** nm(min)<sup>r</sup> and 957 nm(min)<sup>r</sup> respectively. The values of  $r$  for coatings I, II and III were 0.074, 0.055 and 0.126 respectively.

Figure 9.10 shows typical results from an indent made on coating I. The loading part of the indents was modeled by the JKR theory, using an effective work of adhesion, and the elastic-plastic to fully plastic transition, using the Tresca's yield criteria. This approach led to an effective yield stress  $\sigma_y$  (yield strain,  $\epsilon_y$ ), which is important in describing the deformation resistance of these materials when subjected to severe compressive and tensile stresses in industrial processes, such as calendaring and impact printing. The unloading portion of the indents was modeled using the radius of the elastically recovered crown, determined approximately by the material hardness, in conjunction with the *crack tip creep* model as proposed by Johnson [20] and described in section 3.2.1. The value of equilibrium work of adhesion was assumed to be 50 mJ/m<sup>2</sup>. This value is appropriate for such soft materials [4] and variations in this value ( $\pm 20\%$ ) did not seem to appreciably affect the modeling results. This value of 50 mJ/m<sup>2</sup> can be shown to be reasonable for coating composite using a simple rule of mixtures. For the latex the work of adhesion has been calculated to be around **80** mJ/m<sup>2</sup> as shown in chapter 5. For polystyrene the work of adhesion has been similarly calculated to be around 40-45mJ/m<sup>2</sup>. Therefore, from a simple rule of mixtures it can be expected that the resultant work of adhesion would be between 40 and **80** mJ/m<sup>2</sup>. More careful experiments need to be done in order to verify this assumption. The loading portion of this indent is divided into three parts depending on the value of critical yield parameter,

$C_Y$ . The critical yield parameter is defined as the ratio of the imposed stress to the material yield stress and is given by,  $C_Y = Ea / R\sigma_Y$ . Here  $E$  is the material instantaneous elastic modulus,  $a$  the contact radius,  $R$  the probe radius and  $\sigma_Y$ , the material yield stress. The early portion of loading is elastic as long as  $C_Y \leq 10$ , but as the loading stresses increase the contact approaches the elastic-plastic regime with  $C_Y \approx 40$ , and finally the material yield stress,  $\sigma_Y$ , is approached when  $C_Y \geq 400$  and we have complete plastic deformation. For the curve in Fig. 9.7 the parameter values for  $E$ ,  $R$  and  $\sigma_Y$  were, 1.0 GPa, 10  $\mu\text{m}$  and 2 GPa respectively. The first step in modeling the curves is to assume perfectly viscoelastic behavior with the compliance given in table 9.2. If the material would be perfectly elastic with an extremely high value of yield stress then the loading would follow the dashed line as shown during the loading part of the curve. The dashed line does a good job of modeling for the initial part of the curve before it finally diverges. This point of divergence is not distinct and varies from curve to curve. Similarly the different regimes of deformation overlap and there is not clear distinction between them. The critical yield parameter, however, can be used to differentiate between the different regimes. The next step is to incorporate material yield stress. Three different yield stress values of yield stress are shown in figure 9.9 and from a direct visual analysis 2 GPa does the best job of modeling the data. Modeling debonding requires a value of  $R'$ , which is the radius of the viscoelastically recovered crown. In order to fit the debonding portion we have to assume values of  $R'$ . The values of  $R'$ , which enabled best fits are shown in table 9.2. Johnsons crack tip creep approach was used to incorporate viscoelasticity in modeling the debonding behavior. This behavior is shown by the line during the debonding portion. If the material were to behave perfectly elastic its behavior would be depicted by the dashed line for the debonding portion. It should be noted that adhesion is included in modeling since we are using the JKR approach.

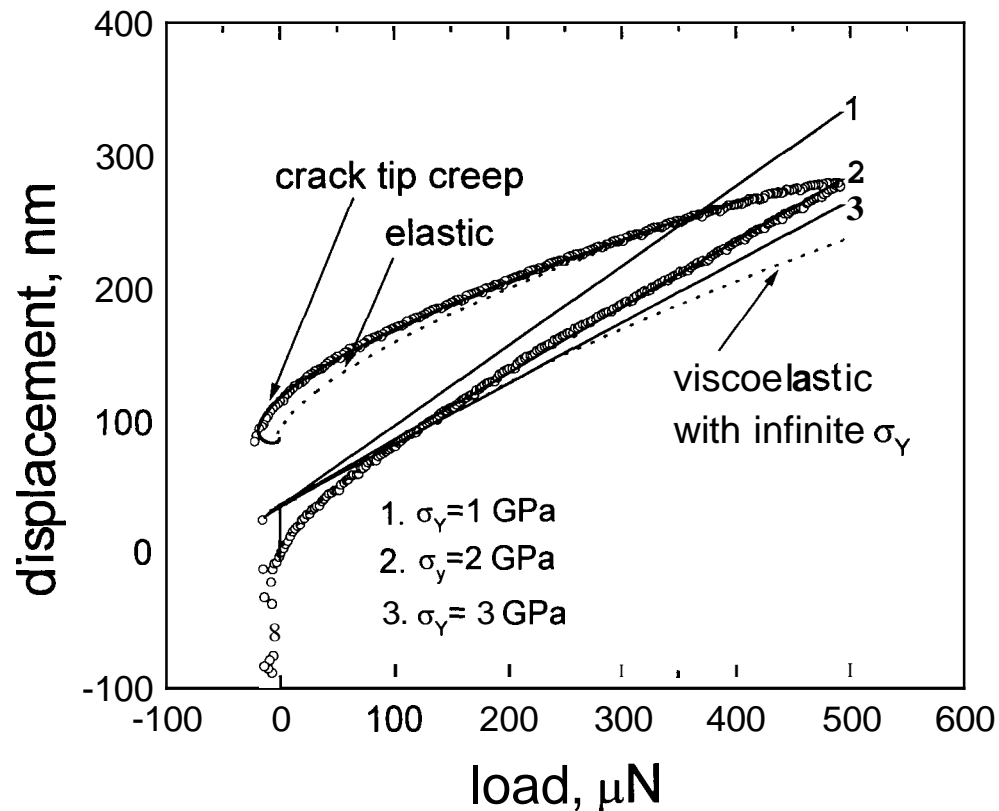


Fig. 9.10 A load-displacement curve from an indent made on coating I (PS). The dashed line for the loading part of the curve is for a purely viscoelastic material. The dashed line for the unloading part of the curve is for a purely elastic-plastic material. The material being tested is viscoelastoplastic. The solid lines during the loading portion of the curves indicate material plastic deformation through the use of a yield stress. Visually, solid line number 2 does the best job of fitting the data and therefore the yield stress corresponding to this line is considered as the material characteristic property.

During unloading if the material was perfectly elastic-plastic it would relax elastically and follow the dotted line. The modulus,  $E_o$ , was assumed to be within 10% of the values given by Prall [15]. Due to the latex, the coating is partially viscoelastic and therefore the unloading profile has to be modeled using the crack tip creep approach as discussed in section 3.2.2. The material compliance was deduced from the Dynamic Mechanical testing done by Prall [15]. The compliance that best fits her data is indicated in Table 9.2. Figure 9.11 and 9.12 show more data for the PS/latex coating. The approximate values of  $R'$  for all coatings are shown in Table 9.2. In both 9.11 and

9.12, curves 1 through 5 represent the first to the last indent made at the same location with decreasing indentation load in order to minimize the extent of plastic deformation. There are two key points to be noted here.

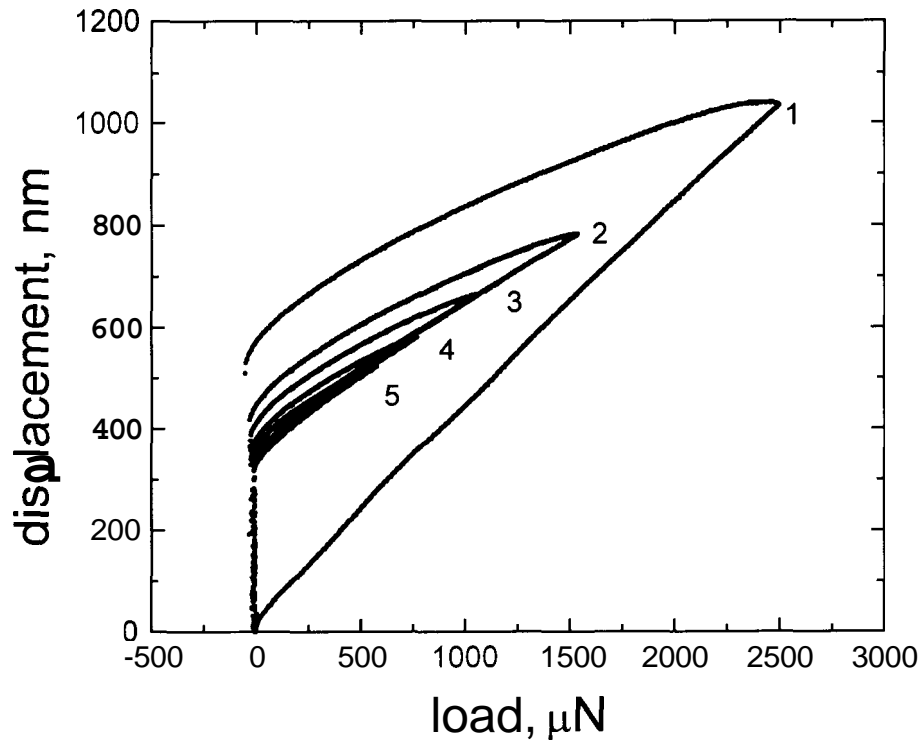


Fig. 9.11 Cyclic tests done at the same location on coating I (PS/latex). The time gap between each indent was about 20s. It can be seen that the first indent results in the most plastic deformation. The subsequent indents almost start at the same location suggesting that the structure is now possibly in a compacted, densified form and behaves more like a viscoelastic material.

Firstly, for indents 2 through 5 the point of contact of the probe with the pre-deformed surface is approximately the same at about 350 nm. This means that the last four indents, which were made on the viscoelastically recovered crown of indent 1, are essentially viscoelastic or moderately viscoelasto-plastic in nature with no signs of subsequent permanent deformation. We reduced the maximum load in the subsequent indents in order to minimize the extent of plastic deformation. This can be confirmed by modeling the loading part of indents 2 through 5 by using

the simple JKR approach with an effective probe radius given by  $RR'/(R+R')$ . The same value of  $W$  of  $50 \text{ mJ/m}^2$  is used in modeling the subsequent indents. Therefore the idea of treating unloading as debonding from a viscoelastic material with an effective radius  $R'$  is reasonable. The dotted lines in figure 9.12 during the loading portion indicate material behavior if it were purely viscoelastic with infinite yield stress. All the dotted lines do not overlap since there was a 10% variation in the instantaneous value of the elastic modulus. Secondly, most of the plastic deformation takes place in the first indent. This was confirmed by repeated indentations at the same locations with the same maximum load. Figure 9.13 shows five indents made on coating I (PS/latex) at different locations under different loading rates. The loading part of the curves can be modeled using the Johnson's elastic-plastic approach with the pure elastic behavior shown by the dotted lines in each case. The modeling parameters are indicated in Table 9.2. In each case there is a residual plastic deformation which is governed by the maximum indentation load. All the dotted lines in this figure do not exactly overlap since there is at least a 10% variation in the material instantaneous modulus. We used the modulus, which was within 10% of the values reported by Prall [15] and gave us the best fit for the initial elastic-loading portion.

Figures 9.14 and 9.15 show the deformation behavior of coatings II (Clay) and III ( $\text{CaCO}_3$ ) respectively. The same procedure, described earlier, was followed to model the complete deformation behavior. The modulus values used for fitting the curves as well as the resultant yield stress values have been reported in table 9.2. For coatings III and I we do not observe much of a difference in the reproducibility of the loading-unloading curves from point to point, which indicates that the samples are fairly uniform in terms of distribution of material properties. However, for coating II, shown in Fig. 9.14, the loading portions of the curves differ substantially from point to point. For instance, indents 1, 2 and 4 in Fig. 9.14 show higher elastic modulus as compared to indents 3, 5. This could be due to the indenter contacting the clay plates at specific

sites, which result in higher modulus values and interstitial sites (between clay plates), which results in lower modulus values.

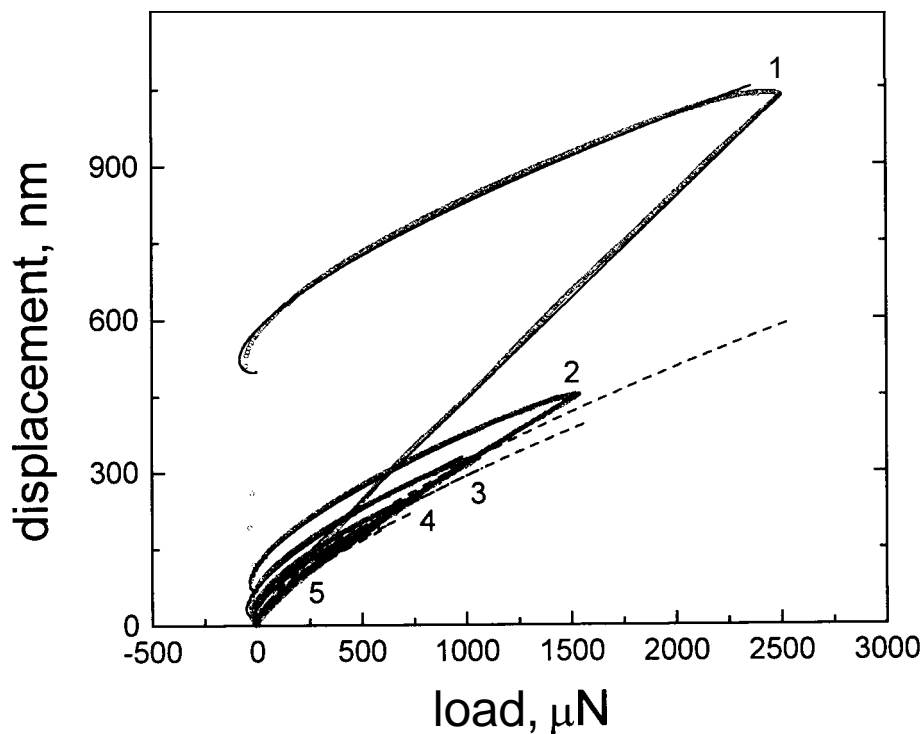


Fig. 9.12 The data as in Fig. 9.11 with model fits. All data have been shifted to start with zero at the initial point of contact. The dotted lines are for a pure viscoelastic case whereas the solid lines take into account material yield behavior. The material yield stress can be calculated from these curves, as described in the text. The dotted lines follow the order of applied load. For instance, the longest dotted line corresponds to the indent with the maximum load (indent 1) and so on.

Table 9.2 shows the average values of yield stress, and compliance function parameters for the three coatings. Coatings II and I have almost similar yield stress values. Coating III did not show substantial yield (showed maximum percentage recovery) for the experimental indentation depths. Although coating III did show some residual plastic deformation, observing the onset of yield from the loading portion was not very clear.

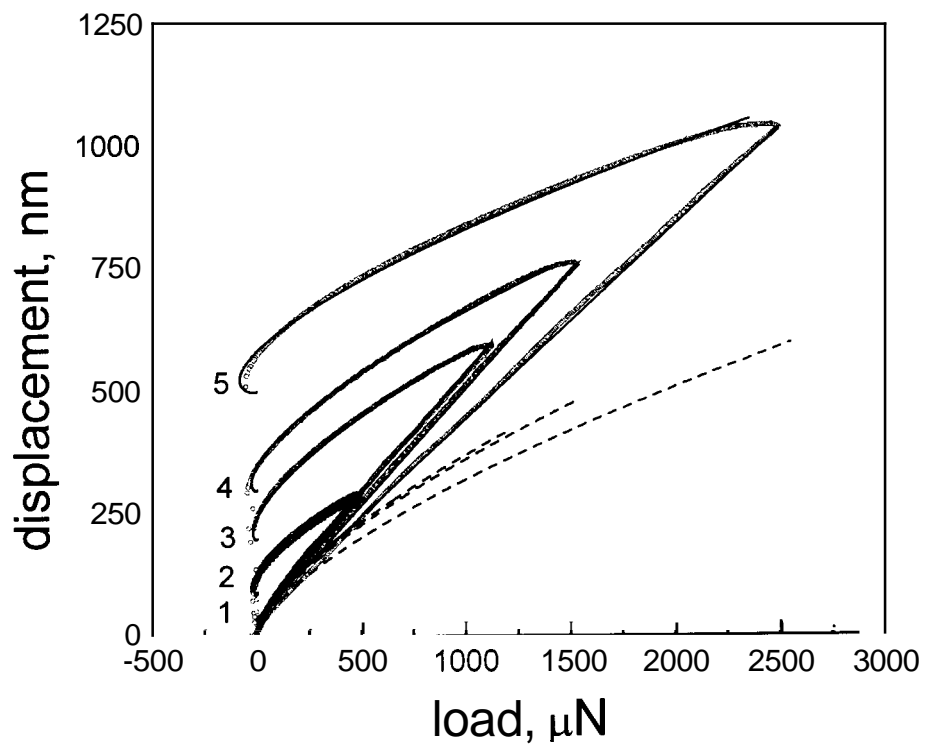


Fig. 9.13 cyclic indents on different locations on coating I. Modeling the curves results in a yield stress value which is almost similar for all the curves. The dotted lines follow the order of applied load. For instance, the longest dotted line corresponds to the indent with the maximum load (indent 5) and so on.

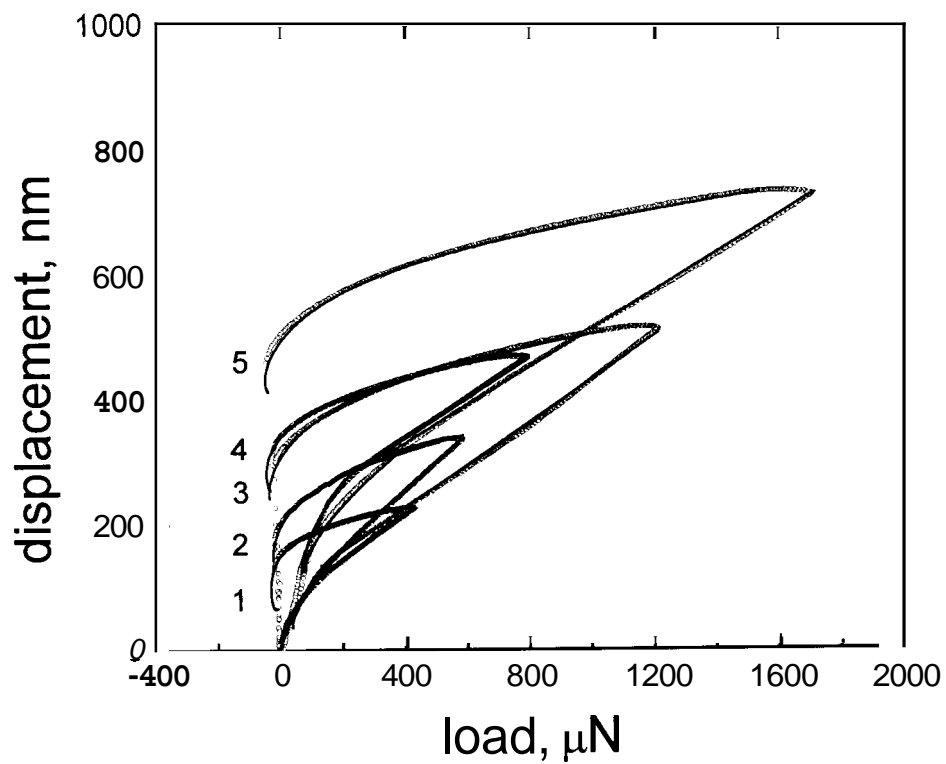


Fig. 9.14 Cyclic indents made on coating 11. The loading part shows a range of behaviors, which could be possibly due to near surface non-uniformities due to the structure of clay particles. The unloading part is more reproducible for all the curves.

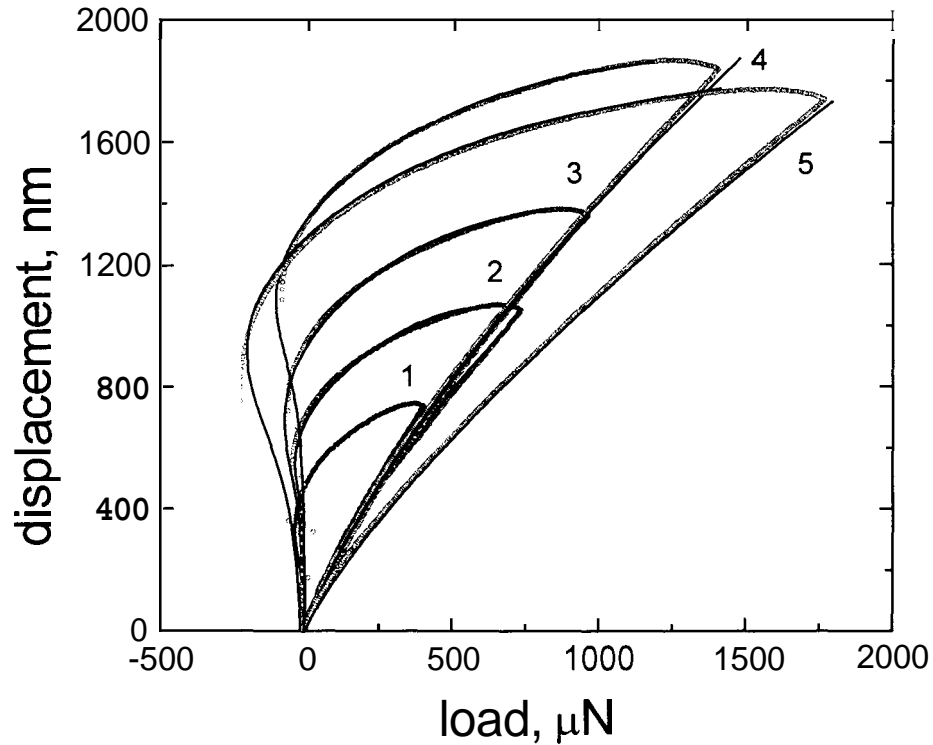


Fig. 9.15 Cyclic test results from coating III. These coatings were more viscoelastic. This is also evident from the large hysteresis in the load-displacement curves. The bulk rheological data from Prall [15], as shown in Table 9.2 also confirms the greater dissipative behavior of Coating III. A maximum yield stress value for this coating is also reported in Table 9.1

Coating II containing Clay shows the most plastic deformation because of its porous structure, followed by Coating II and Coating I. The hardness values play a role in deciding the effective radius of the viscoelastically recovered crown  $R'$ . Greater the value of  $H$ , closer is  $R'$  to  $R$  and the material is more elastic-plastic. Since coatings III has greater values of  $R'$  they show the least plastic deformation.

For the pigment volume concentrations analyzed, coatings containing inorganic clay pigments showed more plastic deformation than the polystyrene plastic pigment and  $\text{CaCO}_3$  pigments.

## 9.5 Discussions

The pigments, latex and air constitute the three phases. When a coating composite is compressed under a load many different events could occur. The pore structure could collapse leading to the formation of new interfaces between latex surfaces. Latex could also possibly come into contact with pigments, thereby forming new latex-pigment junctions. Pigments could also be compressed against other pigments leading to reorganization in the composite structure, reduction in the void fraction and reduction in the total surface area. In this section we will discuss the results obtained above in the light of these possible microscale mechanisms.

We define “permanent deformation” as the ratio of the final indent depth to the depth at contact rupture. The depth at contact rupture can be approximately determined from the load-displacement curves and the final depth has been measured from imaging the indent over a period of 2000 minutes. Coating II shows most permanent deformation followed by coating I and coating III. Load-displacement curves on coating III show most hysteresis. Since coating III shows the least permanent deformation its can be said that most of the dissipation is due to the viscoelastic character of the coating.

In order to determine the possible microscale mechanisms participating in coating deformation, we first determine the area under a typical load-displacement curve. The area under a load-displacement curve gives an idea of the total energy dissipated in the process. This total energy consists of contributions from the material viscoelastic dissipation as well as due to formation of new surfaces and perhaps, other processes. Let’s consider the hysteresis curve in Fig. **9.10**. The total area under this curve is approximately  $2 \times 10^{-11}$  J ( $\pm 5$  %). If we assume that this energy dissipation is entirely due to new latex surfaces coming in contact, then we can estimate the total new area. Using a value of  $70 \text{ mJ/m}^2$ , for latex-latex work of adhesion, about  $25\text{-}36 \mu\text{m}^2$  of new

latex-latex interface would have to form during deformation. From theoretical calculations, (described in section 3.3) for the curve in Fig. 9.10, the maximum contact radius is about  $1.5 \mu\text{m}$ . This clearly suggests that the energy dissipated overestimating the new interface formed. Examining the curve in Fig. 9.7 reveals that viscoelasticity of the latex also plays an important role in determining the overall dissipation. This dissipation could possibly be leading to an overestimation of the contact radius. *So* in order to validate our analysis we need to perform the tests at a rate, which is slower than the relaxation/recovery time of the coating. From Fig. 9.6 it can be seen that the time constant for indent recovery is close to 1000s, whereas most of our experiments were done in 5-10s. The time constant of indent recovery is the time it takes for the indent to recover 70% of its final residual value.

One possible approach towards better understanding the mechanisms behind permanent deformation would be to conduct experiments with a time period of 1000-2000s. The latex itself has its dominant relaxation time in the vicinity of 0.01-0.1s and therefore relaxation of the coating structure cannot be explained solely on the basis of pure latex behavior. The relaxation of the coating is more complicated and its understanding would require more detailed and systematic investigations. Another possible approach is to model the unloading part of the curve assuming the material modulus to be the same as that of the latex relaxed modulus. This would then give us a better idea of the role played by the latex relaxation in determining the hysteresis in the load-displacement curves.

We will now analyze the “formation of new surfaces” reasoning made earlier from a void fraction perspective. This would provide us further confirmation regarding the microscale processes that participate when coatings are compressed. Typical void fraction values for high PVC (70-80%) have been reported to be in the vicinity of 25-35% depending on the type of pigment used [14]. Clay pigments usually result in higher void fraction [18]. In the effective medium model of viscoelastoplastic deformation, there exists a region below the contact where most of

the permanent (plastic) deformation takes place [5]. The radius of curvature of this area can be estimated from,

$$\frac{E \tan \alpha}{\sigma_Y} = 6(1 - \nu) \left( \frac{c}{a} \right)^3 - 4(1 - 2\nu)$$

where  $\nu$  is the material Poisson ratio and  $\alpha$  is the half-angle of the conical indenter. It should be noted that our measurements were not done with a conical indenter and an equivalent expression for a sphere should be used. But for this rough approximation we will use the conical geometry assuming that geometry does not have a substantial impact on this analysis. All other symbols have the usual meaning. For  $E = 1.5$  GPa,  $\sigma_Y = 2$  GPa and assuming  $\nu$  to be 0.3, we can then estimate  $c$  to be approximately 1.2-1.5 times the contact radius  $a$ . The volume corresponding to radius of  $c$  is then given by  $(2/3)\pi c^3$ . This is the volume in which all permanent deformation occurred. The total void fraction corresponding to about 30% of this volume is approximately  $(1/3)\pi c^3$ . We can then calculate the “new surface area available” by calculating the radius corresponding to this volume. This radius comes out to be 1.2-1.3 $a$ , where  $a$  is the original contact radius. The total deformed volume is  $(2/3)\pi a^3$ , which is  $700 \mu\text{m}^3$ . This suggests that there is substantial pore volume present underneath the compressed zone for the formation of new surfaces and part of the energy dissipated in the load-displacement curves can be explained from this analysis. From figure 9.4b, the approximate volume of the permanent deformation is  $12.5 \mu\text{m}^3$ , corresponding to a radius of  $5 \mu\text{m}$ . Therefore, if all the deformation were due to decrease in pore volume, the fractional decrease in the pore volume due to is only about 2-5 %. If we consider each pore to be about 150 nm in diameter then we can estimate the total number of pores collapsed under a deformation. For the indent in figure 9.4b, the total deformed volume is  $12.5 \mu\text{m}^3$  and therefore, the total number of pores would approximately be 890. The total surface area of these pores is about  $100 \mu\text{m}^2$ . If all this surface area were converted to “new” latex-latex inter-

face or latex-polystyrene interface with an average surface energy of 10-20mJ/m<sup>2</sup>, the energy gain would be on the order of 10<sup>-12</sup> J. This value is comparable to the energy dissipated during the indent.

## 9.6 Conclusions

Indentation experiments were conducted using two different probe shapes on pigmented coating composites. The two different probes have been discussed in chapter 2. The pigmented coatings analyzed consisted of organic polystyrene pigments (particle size, 450 nm) and inorganic CaCO<sub>3</sub>, kaolin Clay pigments, dispersed in a discontinuous medium of styrene-butadiene latex. Most commercial pigmented coatings contain more than 70% pigment volume concentration and therefore we analyzed PVC's >70% for all coatings. At this high PVC the predominant behavior of all coatings is elastic-plastic but evidence of viscoelasticity, primarily due to the latex, could be observed during the unloading cycle. The loading part of the curves was modeled by using the JKR theory combined with the Tresca's criteria for plastic yield. When the stresses imposed upon the material exceed the material yield stress, the material deforms permanently. Cyclic experiments were conducted at loads high enough to produce contact stress higher than material yield stress. The residual plastic deformation was imaged using the indenter itself. Another method of confirming permanent deformation was to indent at the same point with decreasing loads over a period to time and observing the "new" point of contact of the probe with the pre-deformed surface. Modeling decohesion incorporates this residual deformation, which appears in the form of the recovered crown of radius  $R'$ . The recovery of the indent is viscoelastic because of the latex present and therefore modeling the unloading part requires two independently measured quantities, which are the residual indent depth,  $\delta_R$ , and the composite compliance,  $\phi(t)$ .

For the coatings analyzed, CaCO<sub>3</sub> pigmented coatings exhibits the most viscoelasticity in terms of the greater hysteresis in the load-displacement curves. This is probably not a surprising

result since  $\text{CaCO}_3$  coatings have been shown to have greater resilience than Clay coatings since viscoelastic dissipation plays a substantial part in the deformation of these  $\text{CaCO}_3$  coatings [19]. Coatings containing Clay have the same viscoelastic character as the polystyrene pigment coating but the clay coatings shows considerably more plastic (permanent) deformation. Overall, clay pigmented coatings show maximum plastic deformation followed by  $\text{CaCO}_3$  and polystyrene pigments. Useful quantitative information about material yield stress and plasticity can be obtained from simple nano-microscale indentation testing which is insightful for understanding the complete material behavior under out-of-plane (thickness) compressive stresses. This information is particularly important as a design variable for formulating specific coatings to match end use applications in the paper, paint and adhesives industry.

The true reason behind the permanent deformation is not yet known. We have discussed “permanent deformation” by describing “formation of new surfaces” due to closing of the porous structure and latex surfaces coming into intimate contact. **A** simple analysis by considering the area under the load-displacement curve reveals that the “formation of new surfaces” approach leads to an overestimate of the “new” area. This is due to the fact that the load-displacement curves are affected by the viscoelasticity of the coatings and therefore the tests need to be done slowly in order to eliminate the convolution effects due to material viscoelasticity. The right test time frame is estimated to be around 1000s. The void fraction approach also suggests that “formation of new surfaces” does partially explain the hysteresis in the load-displacement curves. In the future a systematic approach has to be adopted in order to investigate the different microscale mechanisms participating in the deformation of pigmented coatings. Then load-displacement curves have to be combined with pore structure and pore volume analysis.

9.7 **References for chapter 9**

1. Maugis, D. J. *J. Colloid Interface Sci.*, 1992, 150, 243.
2. Hughes, B. D.; White, L. R. *Q. J. Mech. Appl. Math.* **1979**, 32, 445
3. Maugis, D.; Barquins, M. *J. Phys. D: Appl. Phys.* **1978**, 11, 1989.
4. Mesarovic, S. Dj., Johnson, K.L.; *J. Mech. Phys. of Solids*, **2000**, 48, 2009.
5. Johnson, K.L. Adhesion at the Contact of Solids, in *Theoretical and Applied Mechanics*, Proc. 4<sup>th</sup> IUTAM Congress, Amsterdam, p. 133, Koiter, W.T. (editor), 1974, Johnson, K. L. (1985) Contact Mechanics, Cambridge University Press.
6. Pfeiffer, J. D., *Finishing and Converting Conference Proceedings*, 1980, p. 19, TAPPI Press, Atlanta, GA.
7. Rodal, J. J. A., *TAPPI J.*, 1989, 5, 177.
8. LePoutre, P. The structure of paper coatings: An update, *Progress in Organic Coatings*, **1989**, 17, 89.
9. Ferry, J.D. *Viscoelastic Properties of Polymers*, 3<sup>rd</sup> ed., Wiley, New York, 1980, 641p.
10. Kan, C.S., Kim, L.H., Lee, D.I., van Gilder, R.L. *TAPPIJ*, 1997, 80, 5, 19.
11. Parpaillon, M., Engstrom, G., Pettersson, I., Fineman, I., Svanson, S.E., Dellenfalk, B., and Rigdahl, M., *J. Appl. Poly. Sci.* 1985, 30, 58.
12. Van Gilder, R.L., Purfeerst, R. D. *TAPPIJ.*, 1994, 77, 5, 230-239.
13. Yang, X., Bousfield, D.W., Kettle, J., Hultgren, L., Hayes, P., Proc. of the TAPPI Fundamental Coating Conference, *TAPPI Press*, San Diego, CA, May 2001.
16. Ishikawa, O., Yamashita, T., and Tsuji, A., *Characterizing mechanical properties of latex film and coating layer in paper coating using dynamic mechanical thermal analyzer*. In *Surface Phenomena and Latexes in Waterborne Coatings and Printing Technologies*, Plenum Press New York, **1995**, 91, Joyce, M., Hagen, R., and de Ruvo, A., Mechanical consequences of coating penetration, *Journal of Coatings Technology*, **1997**, 69, 869, 53.

17. Nielsen, L.E.; *Mechanical Properties of Polymers and Composites*, Dekker, New York, **1974**, vol. **2**.
18. LePoutre, P., Hiraharu, T., On the Cohesion of Clay and CaCo<sub>3</sub> Coatings, Note in *J. App Poly. Sci.*, **1989**, **37**, 2077, Inoue, M., LePoutre, P., *J. Adhesion Sci. Technol.*, **1992**, **6**, **7**, 851. Inoue, M., LePoutre, P., *TAPPI Coating Conference Proceedings*, **1992**, **6**, **7**, 858.
14. Zosel, A., *Prog. in Org Coat.*, **1980**, **8**, 47-79, Toussaint, A. *Progress in Org. Coat.*, **1973**, **2**, 237-267, Raman, K., Bousfield, D.W., and Shaler, S.M., *TAPPI Coating Conference Proceedings*, Philadelphia, **1998**.
15. The thesis by Katharina Prall, *Micromechanical Properties of Pigmented Coating Composites*, **2000**, Department of Chemical Engineering, University of Maine, Orono, ME **04473**, USA.
19. Hagen, R., Salmen, L. and deRuvo, A, *J. of Appl. Poly. Sci.*, **1993**, **48**, **603-610**, Hill, L.W., Mechanical Properties of Coatings, *Federation Series on Coating Technology*, 1315 Walnut ST., Philadelphia, PA **19107** USA, **1987**.
20. Johnson, K. L. (2000) "Contact Mechanics and Adhesion of Viscoelastic Spheres," Microstructure and Microtribology of Polymer Surfaces, eds., V. V. Tsukruk and K. J. Wahl, American Chemical Society, Washington, D.C., **23-36**.

## Chapter 10. Summary of Linear Viscoelastoplastic fracture studies

### 10.1 Conclusions

A method for predicting the compressive yield stress,  $\sigma_y$ , of composite coatings containing different pigments dispersed in a semicontinuous matrix of styrene-butadiene latex is presented. This is an effective medium approach since at high pigment volume concentrations the composite is anisotropic and heterogeneous. These materials are viscoelastic due to the presence of latex but also exhibit residual plasticity due to the presence of air. *So* under the application of slight compressive stress the pores collapse resulting in a denser structure. We use the viscoelastic crack tip creep approach in conjunction with a recent work on elastic-plastic deformation done by the same author to model our results and obtain a yield stress. The yield stress values can be directly obtained from the loading part of the curve after assuming a reasonable value for the work of adhesion and an airport information of the materials compliance and the experimental conditions, such as the loading rate and time of contact. Coating yield stress is an important parameter in the calendering and printing operation.

Recently particle motion simulation techniques have been used to model the loading-unloading behavior of highly filled systems. This technique uses a force balance approach to monitor the deformation of a single or multiple particles in a coating composite. Although still in a developmental stage, results from this technique show remarkable resemblance with the indentation test.

### 10.2 Future extensions

This was preliminary study using the viscoelastoplastic materials. In order to study this approach more systematically we need to formulate coatings with different pigment shapes and porosity and study their time dependent deformation behavior. This technique has the potential of being a standard for predicting the mechanism of yield in pigmented coatings.

## PART IV: Influence of Substrate Roughness and Compressibility on Blade Coating

### Chapter 11. A Semi-Quantitative Study of Blade Coating (Simulation)

#### 11.1 Introduction

The elastic deformation of a rough paper web is modeled in conjunction with fluid dynamics during blade coating. Deformations are calculated using the simple spring model assuming paper to be a linear isotropic solid. The constrained column model (CCM) is used to convert the measured elastic modulus values,  $E$ , into spring constant  $k$  by assuming a Poisson ratio value of 0.1 for paper. The fluid flow is modeled using the lubrication theory. Elastic moduli for typical base sheets were estimated by conducting compression tests with a nano-indenter. The pressure distribution is solved along with the compression of the web. As the compressibility of the web increases, the single pressure peak develops a shoulder or a broader shape. A rough incompressible web generates pressure fluctuations under the blade. The roughness amplitude, compressibility, and blade gap ratio are important parameters that influence the pressure distribution under the blade and distribution of coating.

Paper is coated in order to improve its surface smoothness, which has a direct impact on its printing properties. Paper coating and printing is often a high-speed process. Paper is inherently compressible and rough with local variations in these characteristics. One purpose of the coating operation is to cause the surface to be uniform. Additional requirements of the coated paper depend on the end use. Even though the influence of coating rheology on the blade coating process has received much attention, little theoretical work has been given to understand the influence of the base stock roughness and compressibility on the coating process. Recent work by Allem *et al* [1] suggests that blade coating will “level” the base sheet roughness by filling in the valley and covering the hills with little coating, but a good understanding of the distribution of coating on a rough sheet is lacking.

Recent work by Xiang *et al.* [2] indicates that a local variation of coating properties is associated with back trap mottle problems. These issues may be related to coat weight variations after the blade. An important question remains with regard to the coat weight distribution produced by a blade on a rough substrate. This problem has received no theoretical analysis. The work in this paper is a first attempt at trying to understand the influence of substrate roughness on coat weight variation by solving the coupled fluid dynamic and solid mechanic equations.

Blade coating operation has received much attention in the last two decades. Turai [3], Kahila and Eklund [4], Kuzmak [5] have analyzed the various aspects of the blade coating process. All these considered lubrication flow under the blade along with the blade loading as controlling parameters for the coat weight. Saita and Scriven [6] modeled deformation of the blade during bent blade coating. The deformation of the blade was calculated in conjunction with lubrication flow. An important result of the work was that, beyond a certain loading the coat weight increases instead of decreasing. The results show a certain limit to the minimum coat weight that can be obtained with bent blade coating.

Pranckh and Scriven [7] presented a finite element analysis of the blade coating operation with an applicator roll. The full two-dimensional flow field was calculated with free surfaces upstream and downstream of the blade. The blade deflection was computed with the coating flow. The compression of the paper was included as a simple spring model: the substrate deforms locally to local stresses and that local compression is proportional to local loading. The model is particularly viable for low Poisson ratio materials such as paper but might fail to describe materials like rubber. The rubber roll usually has a fifty-fold greater thickness than the web and deformations it undergoes are large compared to the web. Isaksson and Rigdahl [8] incorporated shear-thinning rheology of the fluid. The effect of substrate compression was reported. However, the compression shape and amount were estimated and not calculated. It was, nevertheless, shown that compression of the substrate has a significant effect on the pressure distribution in the blade.

The hardness of the backing roll has been shown to influence the coat weight by Ortman and Donigian [9], which confirmed the deformation of the backing roll during the process. Additionally, it shows that paper deformation is minimal compared to the deformation in the backing roll in terms of determining the coat weight distribution.

Experimental results of blade coating have been presented by Eklund and Kahila [10], Triantafillopolous and Altug [11], Guler and Bousfield [12], Issakson et al., [13]. The lubrication forces are computed based on an assumed geometry. These forces can change drastically based on the geometry; for instance, Guler and Bousfield [12] showed that a 1° shift in the blade angle could cause a doubling of the forces on the blade.

Bousfield *et al.* [14] used the finite element analysis to compute the web and backing rubber roll deformation assuming linear elastic constitutive equations for the paper web and the rubber covered roll. Paper web and the rubber roll were assumed to be linear isotropic solids. Deformation was calculated using the simple spring model and fluid flow was modeled using the lubrication theory. It was shown that substrate compression would cause fine features on the geometry to change thereby modifying the forces in the lubrication flow. A dimensionless number (Elasticity number) as defined previously by Carvahlo and Scriven [15], which includes web velocity, coating viscosity, final film thickness and the elastic modulus of rubber was used to describe excessive compression.

Here we extend the work of Bousfield *et al.* [14] by incorporating the substrate roughness in the model. The deformation of the roughness is calculated in conjunction with the local fluid dynamics. A rough substrate generates pressure fluctuations under the blade. If the roughness is large and the wavelength of the roughness large, the pressure fluctuations can be the same order of magnitude as the blade pressure and can generate sub-ambient pressures. Compressible webs and compressible roughness minimizes the pressure fluctuations and should lead to a smoother operation.

## 11.2 Compression measurements

Surface compressibility of paper was measured with a Berkovich diamond indenter in a nanomechanical testing system (Hysitron PicoIndenter™ mounted on a Park Scientific Instrument™ CP base). A three-plate capacitor technology provides simultaneous actuation and measurement of force and displacement with a prescribed load and displacement resolution of 1nN and 2 nm respectively. The schematic of contact between the indenter tip and substrate is shown in Fig. 11.1. This instrument can also be used to obtain surface images with a limited resolution because of the tip shape.

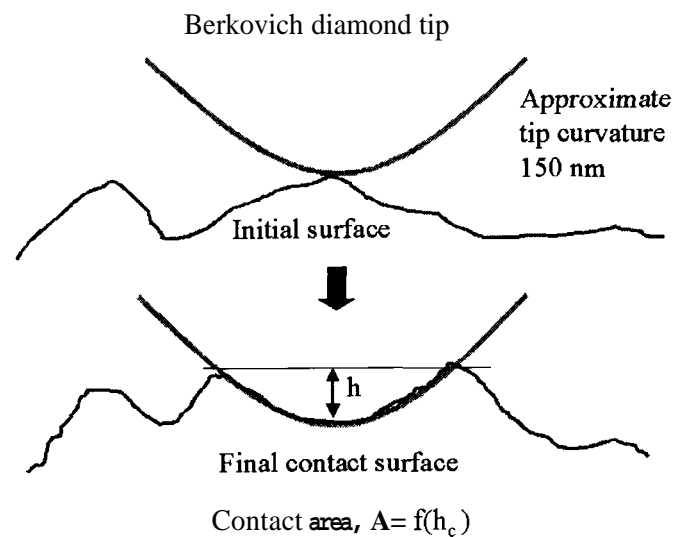


Figure 11.1. Schematic of the initial and final contact between the Berkovich indenter tip and a rough substrate.

Figure. 2 shows a typical load vs. displacement curve ( $F$  vs.  $h$ ) for indents made on paper and also defines the quantities used to measure surface mechanical response. The continuing increase in displacement during the hold period is due to creep and may involve both plastic and viscoelastic processes. The initial slope  $S$  of the unloading curve is related to the effective modulus  $E_r$  by

$$S = \frac{dF}{dh} = 2\gamma E_r \sqrt{A(h_c) / \pi} \quad (1)$$

where  $A(h_c)$  is the projected area of contact at  $h_c$  estimated using a method of Oliver and Pharr [16]. Hay et al [17] pointed out that the correction factor  $\gamma$  is near unity. For hard probes,  $E_r \equiv E/(1-\nu^2)$ , where  $E$  is the Young modulus and  $\nu$  is the Poisson ratio of the substrate. Intrinsic roughness of the substrates can cause  $E_r$  to be overestimated by as much as a factor of ten as shown by Bobji et al. [18]. The natural heterogeneity of the paper samples also contributes additional uncertainty in the determination of  $E_r$ . Thus values of  $E_r$  reported here should be considered as approximate.

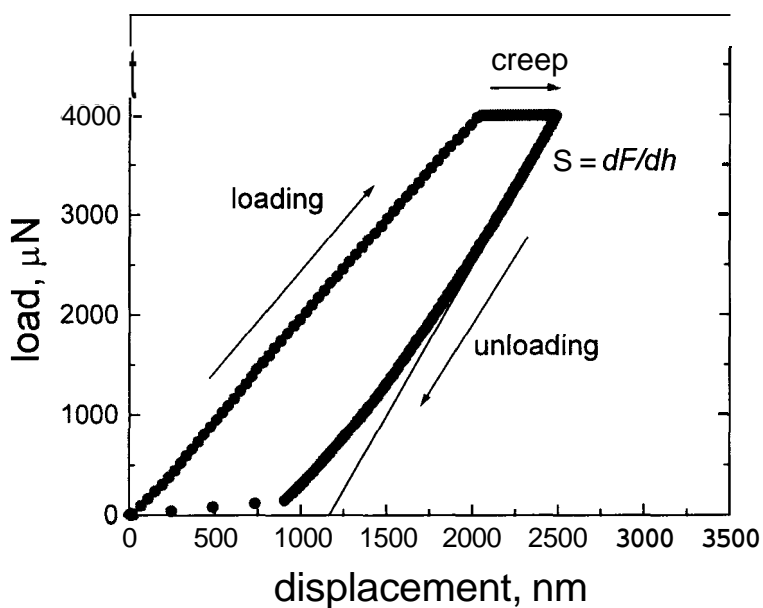


Fig. 11.2 **A** typical load-displacement curve from an indent made on wood-free paper using the nanindentation device.

Indentation experiments were carried out on individual fibers and paper. The modulus values estimated from the stiffness were in the range 0.1-10 GPa. Figure 11.3 shows some typical results for lightly coated paper. The decrease in modulus with depth was found for all materials studied.

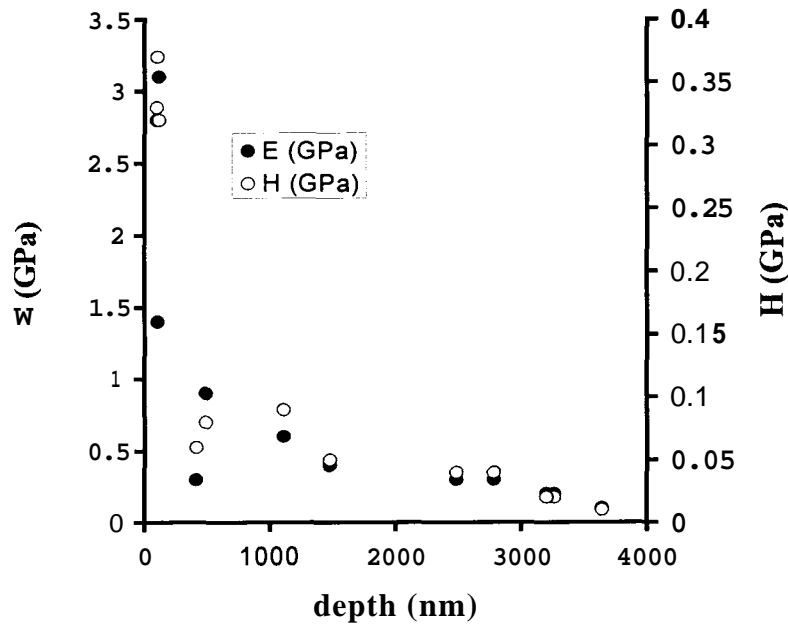


Figure 11.3. Modulus and Hardness estimated from indentations on lightly coated paper.

### 11.3 Model Development

#### 11.3.1 Solid Mechanics

A Fortran code was used to compute the pressure pulse in the dwell zone. Deformation of the paper web was time independent. There was depth dependence in modulus for single fibers as well as paper and other contact area corrections, which will not be discussed here. The blade was assumed to be parallel to the plane of the web. The independent spring model for substrate deformation assumes that the displacement of the web is proportional to the local stress field. The constrained column model (CCM) relates the effective spring constant to the modulus through the Poisson ratio. Because the normal stresses are larger than the tangential stresses, we assume that the local displacement is proportional to the pressure,

$$z - z_0 = kP \quad (2a)$$

$$k = \frac{(1-\nu) E}{(1+\nu)(1-2\nu) L} \quad (2b)$$

where  $z$  is the vertical position of the web surface,  $z_0$  is the undeformed position of the web,  $k$  is the spring constant and  $P$  is the local pressure. In 2b,  $E$  is the measured elastic modulus and  $L$  represents thickness of the base sheet.  $\nu$  is the Poisson ratio of paper and has been assigned a value 0.1. This is similar to the technique used by Bousfield et al [14] and Coyle [19] for forward roll coating with deformable rolls. A key assumption in the spring model is that the applied stress is in equilibrium with the deformation. In actual industrial situation the deformation might lag due to the short time scale of deformation. Current results assume static deformation situation. Dynamic analysis of paper could be added in the future analysis of this problem. Figure 11.4 illustrates the geometry of the situation and the basic parameters.

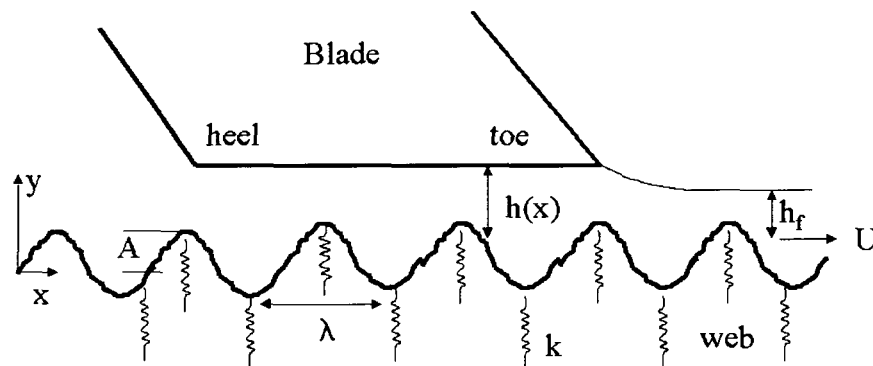


Fig. 11.4. Schematic of the geometry. The gap between the web and blade is stretched for visual purposes.  $U$  is the velocity of the web.  $h_f$  is the average final film thickness.

### 11.3.2 Fluid Dynamics

The fluid dynamics is solved using the lubrication analysis. The pressure profile is found using the equation:

$$\frac{\partial P}{\partial x} = -\frac{12\mu U(h_f - h(x)/2)}{h(x)^3} \quad (3)$$

where  $P$  is the pressure,  $x$  is the position coordinate,  $\mu$  is the viscosity,  $U$  the web velocity,  $h_f$  the final film thickness, and  $h(x)$  is the local distance between the web surface and the blade surface. The pressure boundary conditions are atmospheric pressure at the inlet and outlet streams. The pressure distribution is then integrated to obtain the blade force. If the web deforms then shape factor,  $h(x)$ , changes.

Surface roughness was assumed to be sinusoidal with a roughness amplitude ( $A$ ) and wavelength ( $\lambda$ ). The representation is:

$$h'(x) = A \sin(\lambda x + \phi) \quad (4)$$

$h'(x)$  varies with  $A$  and  $\lambda$  and is incorporated into  $h(x)$ .  $\phi$  is the phase angle. Figure 4 shows the geometry of the blade-paper gap and the coordinate system. The shape factor  $h(x)$  is determined by the geometry of the blade and the instantaneous position of the web accounting for deformation due to compression as

$$h(x) = h_o(x) - h'(x) + kP \quad (5)$$

where  $h_o(x)$  is the geometry of the smooth paper and the blade. Any compression of the substrate increases the gap between the web. Roughness can increase or decrease the gap depending on the location as given in Eq. (3). Fig. 5 in Bousfield et al [14] clearly elucidates the different stages of web compression using this simplified spring model. Here we have used realistic values for elastic modulus of paper along with the constrained column model to obtain an effective value of the spring constant ( $k$ ).

The initial shape factor is calculated assuming no hydrodynamic pressure in equation (4). This shape factor is used to calculate the hydrodynamic pressure distribution under the web by integrating equation (2). This pressure is used to calculate deformation of the paper web and a new shape factor as in equation (4).

The base parameters are a 45-degree angle blade running parallel to the web. Inertial or impulse terms could be included by adding a stagnation pressure, but both are neglected in this work. The geometry has its origin 2 mm upstream from the heel of the blade. The blade thickness is 0.5 mm. The velocity of the web is 15 m/s. The viscosity of the coating is 10 mPas. The wavelength and roughness of the web are changed as well as its compressibility.

A model of this nature involves a number of assumptions. One assumption involves the time scale associated with deformation. The assumption in the above calculation is that the web will instantaneously react to the local pressure field and deform to its equilibrium shape. This assumption can be relaxed in future work, but more information is required to characterize the rapid deformation of paper under these conditions. Our indentation data indicated that creep does occur (Fig. 11.2), but perhaps with a longer relaxation time than important here. Other assumptions include that the web does not absorb fluid, that the coating is Newtonian with constant density, and the web's elastic properties are constant as a function of position and not influenced by moisture. Chen and Scriven [20], for instance, describe the penetration of fluid into a compressible porous web during blade coating. The fluid flow was again described by lubrication theory. Penetration and compression of air was taken into account along with the compression of the web. Compression was again defined using the spring model. Even with these assumptions, it is instructive to understand the influence of roughness and roughness compression on the blade coating process.

## 11.4 Results

Figure 11.5 shows the calculated pressure pulse for incompressible web having 0.18 mm roughness wavelength with 1 and 5  $\mu\text{m}$  roughness amplitude. High roughness amplitudes coupled with low roughness wavelengths lead to drastic fluctuations in the pressure profile. Figure 6 shows similar results except with a smaller wavelength of the roughness. The small wavelength has a smaller influence upon the pressure distribution.

For both Figs. 11.5 and 11.6, the pressure profile is the result at an instance in time. If the phase angle of the roughness changes, the relative location of hills and valleys to the blade will change. The pressure distribution will change rapidly as a function of time. Figure 11.7 shows the results as in Fig. 11.6 except the phase angle increased 180 degrees. The base case is for an incompressible substrate. The locations that were high pressure are now low pressure, as expected. The net result is that fluid near the blade surface will see rapid fluctuations in pressure as the rough web passes under the blade.

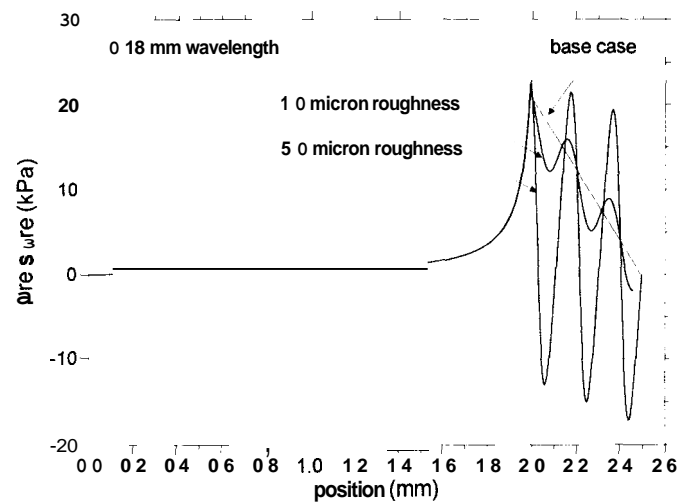


Figure 11.5. Pressure distribution with 0.18 wavelength of roughness and 1 and 5  $\mu\text{m}$  amplitude.

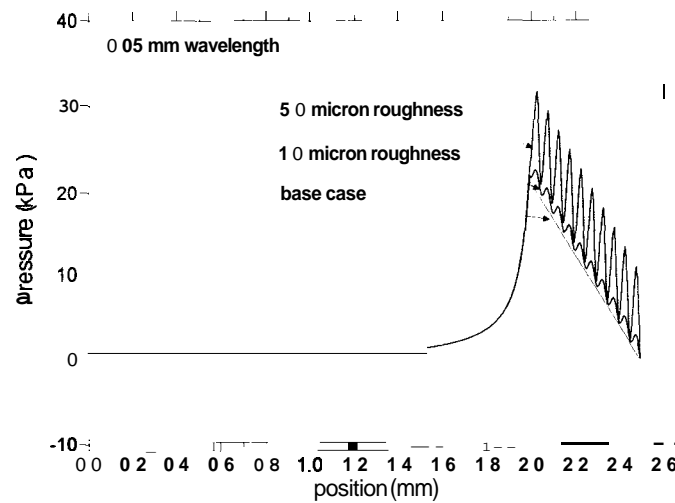


Figure 11.6. Same as Fig. 4 but with 0.05 mm wavelength of roughness.

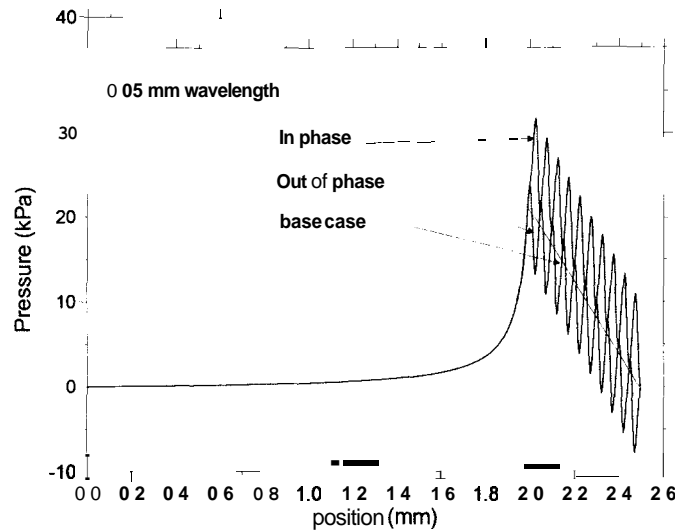


Figure 11.7. Same as Fig. 6 except the roughness is 180 degrees out of phase for 5  $\mu\text{m}$  roughness

Figure 11.8 shows the influence of compressibility on the pressure profile for a smooth web.

Three different compressibility values were compared with a base case of incompressible web. **As** the substrate deformation increases there develops a shoulder near the toe of the blade, which is attributed to the converging nip near the toe as the paper exits from underneath the blade. Figure 5 in Bousfield et al [14] illustrates this situation well. **A** greater compressibility leads to a higher

and narrower peak near the toe as can be seen in the figure. This is due to a steeper converging nip section near the toe. The web was considered to be smooth in this analysis. A major implication of this behavior is that for obtaining the same coat weight on a more deformable substrate a higher blade loading would be required if provided other coating conditions are the same.

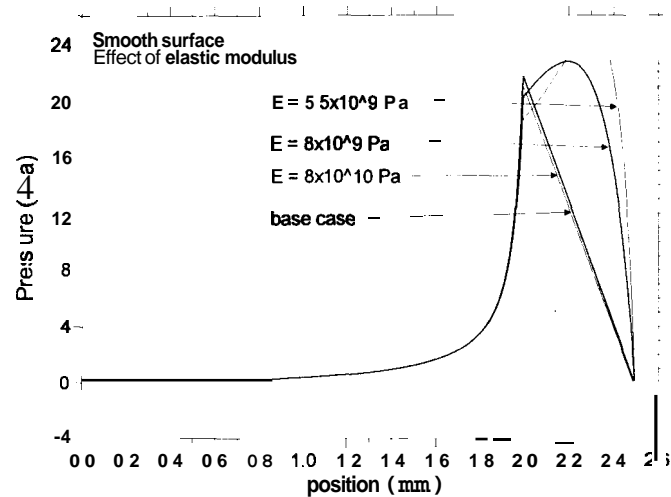


Figure 11.8. Influence of web compressibility on pressure distribution for a smooth web.

Figure 11.9 shows the combined effect of roughness and compressibility. The roughness was kept constant with  $A=1 \mu\text{m}$  and  $\lambda=190 \mu\text{m}$ . Different  $E$  values, varying from 1 MPa to 100 MPa, were used in calculating  $k$  for a base sheet thickness of 0.5 mm. For lower compressibility (higher  $E$ ) the pressure pulse lies close to the base case but as compressibility increases we see greater deviations. The smooth peaks as seen in Fig. 11.8 now have a serrated form due to the rough surface topography. These pressure fluctuations could possibly be responsible for the coat weight variations after the blade. The severity of the fluctuation and the extent of influence on the coat weight distribution would invariably depend on the roughness characteristics  $A$  and  $\lambda$ . The peaks in the pressure pulse are dictated by the topography whereas the form of the profile is described by the compressibility. **Also** noteworthy is the location of the pressure peaks. The pressure peaks for the

most compressible web lie in the narrowest range, which can be explained from the previous plot.

In Fig.5 we did see a narrower, steeper peak for more compressible webs.

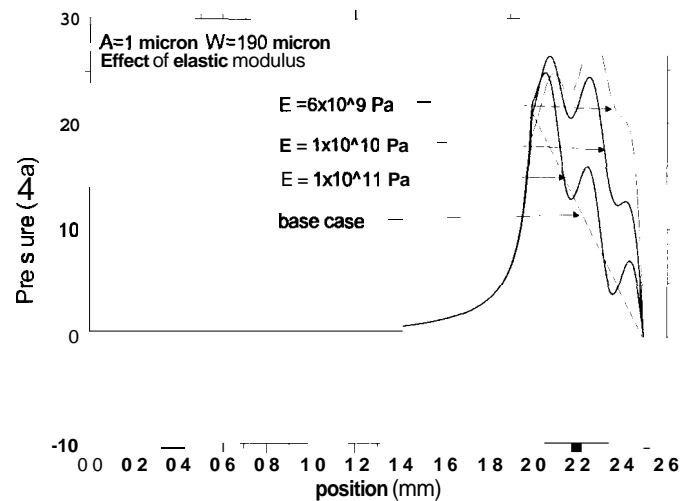


Figure 11.9. Influence of compressibility on roughness pressure distribution for roughness of 1  $\mu\text{m}$  and a wavelength of 190  $\mu\text{m}$ .

There are limitations associated with the spring model. It limits the amount of deformation that can be modeled to give solutions since conflicting demands are placed on the fluid dynamics and solid mechanics. The criterion of single dimensionless elasticity number  $N_E$  still applies. The elasticity number is defined as  $N_E = \mu U / h_f E$  where  $\mu$  is the fluid viscosity,  $U$  the web velocity,  $h_f$  is the nip gap and  $E$  the substrate elasticity. If  $N_E$  is  $>0.015$ , then excessive compression occurs and a steady solution to the set of equations is not possible. The ratio of roughness amplitude to blade gap could possibly be included in this number in order to make the conclusion more robust. An industrial situation will, however, be different because of the porous and viscoelastic nature of the web. As a final comment, the relatively low-pressure peaks in our simulations compared with other work is possibly due to high nip gaps. Decreasing the nip gap will however not significantly alter the conclusions of this work.

## 11.5 Conclusions

A method is proposed to calculate the relationship between the solid mechanics and fluid dynamics for a blade coating system of a rough compressible web. The results indicate a complex pressure profile under the blade is possible due to the web roughness. Larger blade loading is required to obtain the same coat weight compared to the undeformed case and that there is a limit to the minimum coat weight that can be obtained. Small deformation broaden the pressure pulse, but higher deformation lead to greater and narrower pressure peaks near the toe before placing conflicting demands on the equations. Rough substrate compression smoothens out the pressure fluctuations but the degree of compression is limited within the steady solution of the equations. Non-steady conditions may result in the industrial situation.

## 11.6 References for Chapter 11

1. Allem, R., Uesaka., " Coat Weight Distribution on Rough Substrates", Proc. **1999** TAPPI Adv. Coat. Fund. Symp., Toronto.
2. Xiang, Y., Bousfield, D.W., "A new Technique to Analyze Back Trap Mottle ", Proc. **1998** TAPPI Coating Conference, TAPPI Press, pp. **353**, New Orleans, LA **1998**.
3. Turai, L.L., " Analysis of the Blade Coating Process", TAPPI J., **1971**, **54**, **8**, **1315**
4. Eklund, D. and Kahila,S.J., "Processes Occurring under the Blade during Blade Coring", Wochbl. *Papierfabr.* **1978**, **106**,**661**.
5. Kuzmak, J.M., "Bevelled-Blade coating", *TAPPIJ.*, **1986**, **69**, **2**, **72**.
6. Saita, F.A., and L.E Scriven, "Coating Flow Analysis and the Physics of Flexible Blade Coating", Proc. TAPPI Coating Conference, TAPPI Press, pp. **13**, Atlanta, GA, **1985**.
7. Pranckh, F.R., and L.E. Scriven. " The physics of Blade Coating of Deformable Substrates", Proc. *TAPPIJ*, **1990**, **73**, **1**, **163**.

8. Isaksson P., Engstrom, G., Rigdahl, M., "Experimental Analysis of the Dynamic Equilibrium in the Vicinity of the Blade tip during Blade Coating", *Nordic Pulp and Paper Research J.*, **1994**, 3,150
9. Ortman, B.J. and Donigian, D.W., "Coat Weight Non-uniformity due to High Speed Blade Coating: Mechanism and Prevention", Proc. **1992** TAPPI Coating Conference, TAPPI Press, pp. **217**, Atlanta, GA, **1992**.
10. Engstrom, G. and Morin, V., "Analysis of the Processes of Formation and Consolidation in Blade Coating", Proc. TAPPI Coating Fundamentals Symposium, pp. **41-50**, TAPPI press, Atlanta, GA, **1995**.
11. Triantafillopoulos, N.G., and Altug, N., "Experimental Analysis of Forces in Bevelled Blade Coating ", Proc. TAPPI Coating Conference, pp. **77-96**, TAPPI Press, Atlanta, GA, **1994**.
12. Guler, E and Bousfield, D.W., "Blade Force Measurements during Blade Coating", Proc. **1995** TAPPI coating Conference, pp. **53-65**, TAPPI press, Atlanta, GA, **1995**.
13. Isaksson P., Rigdahl, M., " Numerical Simulation of Blade Coaters with short Dwell and Roll Application Coaters", *Rheol. Acta* **33**,**454-467**, **1994**.
14. Bousfield, D.W., M. Wikstrom, and M. Rigdahl, "Roll Deformation During Blade Coating", *TAPPI J.*, **81**, **5**, **207-212**, **1998**.
15. Carvalho, M.S. and L.E. Scriven", "Effect of Deformable roll cover on Roll Coating", *TAPPI J*, **77**, **5**, **201-208**, **1995**.
16. Oliver, W. C., and Pharr, G. M., "An Improved Technique for determining Hardness and Elastic Modulus using load and displacement sensing Indentation experiments ", *J. Maters. Res.* **1992**, **7**, **1564**.
17. Hay, J.C., Bolshakov, A., and Pharr, G. M., " A Critical Examination of Fundamental Relations used in the Analysis of Nanoindentation', *J. Maters. Res.* **1999**, **14**, **2296**.

18. Bobji, M. S., Biswas, S. K., "Deconvolution of Hardness from data obtained from Nanoindentation of Rough Surfaces", *J. Mater. Res.* 1999, 14
19. Coyle, D.J., "Forward Roll Coating with Deformable Rolls: a simple one-dimensional Elasto-Hydrodynamic model", *Chem. Eng. Sci.*, 1998, 43, 2673, Timoshenko, S., Theory of Elasticity, McGraw-Hill Book Co., New York (1934).
20. Chen, K.S.A. and L.E. Scriven, "Liquid Penetration into a Deformable Porous Substrate", *TAPPI J.*, 73, 1, 151, 1990.

## PART V: Summary of Dissertation

### Chapter 12. Summary

Nanoindentation tests were conducted on elastic, viscoelastic and viscoelastoplastic materials using a commercially available nanoindentation device. In the first part of the work we analyzed dynamic contact to viscoelastic materials using two different contact and fracture mechanics theories. These theories include both bulk material properties (creep compliance function, relaxation spectrum) as well as the material surface energy. Although contact mechanics tests have been widely applied to study purely elastic materials or elastomers with glass transition temperatures well below room temperature, they have not been well suited to study viscoelastic materials. Our goal in this work was to develop nanoindentation as a tool to study adhesive viscoelastic materials by using recent theoretical developments in the field of contact and fracture mechanics. A cohesive zone approach was adopted. The cohesive zone parameters are the work of adhesion,  $W$  and the effective range parameter,  $h_c$ . The cohesive zone parameters were first specified using a linear viscoelastic fracture mechanics (LVEFM) theory proposed by Johnson [1]. This theory requires independent determination of the material rheological properties. After specifying  $W$  and  $h_c$ , the next step was to use a more comprehensive theory by Hui. et. al. [2,3], which uses the viscoelastic correspondence principle to express the deformation in terms of a stress intensity functional,  $K_I(t)$ . The stress intensity function depends not only on the material properties but also on the details of the crack tip separation processes. Stress intensity is the most information one can get from a contact mechanics experiment. Understanding stress intensity is a major step forward in effectively designing viscoelastic adhesives.

Our approach towards understanding deformation behavior of adhesives was from a continuum mechanics standpoint. This approach breaks down when the contact narrows down to a few macromolecular chains. The process of separation then becomes highly non-linear and

principles describing polymer chain dynamics have to be employed. It should however be mentioned that in a contact mechanics experiment such non-linear processes are continuously taking place at the edge of the contact (crack tip) but they do not dominate the behavior of the contact. Hence, suggesting that there is an obvious connection between the polymer chain dynamics approach and the continuum mechanics approach would not be too far fetched. More work needs to be done in this direction. Experiments done with the Atomic Force Microscope (AFM) [4], in which single or multiple polymer chains are stretched, have led to fairly good estimation of the spring constant of single chains. This has been done using entropic chain models such as the Freely Jointed Chain (FJC) [5], the Wormlike Chain Model (WLC) and the persistence chain models [6]. Recent work done by Chaudhury [7] shows that, using the information of polymer chain dynamics described above, the energy dissipation associated with bond dissociation, chain scission, viscous chain desorption can be calculated. This energy is intrinsically related to the stress intensity at the crack tip or the process zone. Hence we can directly compare the results from continuum mechanics with the results that would be predicted from polymer chain dynamics.

In the second part of our work we have extended the elastic-plastic theory by Johnson [8] to include material viscoelasticity. This was achieved by combining Johnson's crack tip creep theory, with the elastic-plastic theory. This combined theory led to the prediction of a material compressive yield stress, which has potential use in industrial operation dealing with composites. Different pigment types dispersed in a matrix of styrene-butadiene latex were examined using the nanoindentation technique. Imaging the indent showed that the deformation is permanent and hence material plasticity had to be accounted for in the form of a yield stress. Modeling the cyclic test curves required a priori information about the material dynamic rheological properties. This information was obtained from test done by Prall [9]. The processes yielding to final plastic/permanent yield in the material need further research.

## 12.1 Reference for chapter 12

1. Johnson, K. L *Microstructure and Microtribology of Polymer Surfaces*, eds. V. V. Tsukruk and K. J. Wahl, American Chemical Society, Washington, D.C., **2000**.
2. Hui, C.-Y., Baney, J. M., Kramer, E. J. *Langmuir* 1998, 14,6570.
3. Lin, Y. Y., Hui, C.-Y., Baney, J. M. *J. Phys. D: Appl. Phys.* **1999**, 32, 2250.
4. Bemis, J. E., Akhremitchev, B. B., Walker, G. C. *Langmuir*, 1999, 15,2799.
5. Rief, M., Gautel, M., Oesterhelt, F., Fernandez, J. M., Gaub, H. E. *Science*, 1997,276, 1109, Rief, M., Oesterhelt, F., Heymann, B., Gaub, H. E. *Science*, 1997,275, 1295.
6. Marko, J. F., Sigga, E. D. *Macromolecules*, **1995**, 28, 8759.
7. Ghatak, A., Vorvolakos, K., She, H., Malotky, D. L., Chaudhury, M. K. *J. Phys. Chem. B* **2000**, 104, 4018.
8. Mesarovic, S. Dj., Johnson, K. L. *J. Mech. Phys. of Solids* **2000**, 48, 2009.
9. Micromechanical Properties of Pigmented Coatings, A thesis by Katharina Prall, Dept. of Chemical Engineering, University of Maine, Orno, ME 04473, 2000.

## Bibliography

Agarwal, N., Farris, R. J. (1999) "Thermodynamics of Deformation of Latex Blend Coatings and its Implications for Tailoring Their properties" *J. Coatings Technology*, 71, 896, 61-72.

Allen, R., P. Uesaka (1999) "Coat Weight Distribution on Rough Substrates," Proceeding of the TAPPI Advance Coating Fundamental Symposium, Toronto.

Asif, S. A. S. Wahl, K. J., R. J. Colton (1999) "Nanoindentation and Contact Stiffness Measurements using Force Modulation with a Capacitive Load-Displacement Transducer," *Rev. Sci. Instrum.*, 34, 456-463.

De Grace J. H., Boluk, M. Y., Aspler, J. S., Y. H. Zang (1991) "Direct Measurement of tensile Stress ("tack") in thin Ink Films," *J. Rheology*, 35, 345-352.

Barenblatt, G. I. (1962) "The Shape of a Crack Tip," *Adv. Appl. Mech.*, 7, 55-66.

Barthel, E. (1998) "On the Description of the Adhesive Contact of Spheres with Arbitrary Interaction Potentials," *J. Colloid Interface Sci.*, 200, 7-18.

Barquins, M., and D. Maugis (1981) "Tackiness of Elastomers," *J. Adhesion*, 13, 53-65.

Basire, C., C. Fretigny (1997) "Kinetic of Adhesion of a Viscoelastic Sample by Force Microscope," *C. R. Acad. Paris, Series IIb* 1997, 325, 211-218.

Bemis, J. E., Akhremitchev, B. B., G. C. Walker (1999) "Finite Sample Thickness Effects on Elasticity Determination Using Atomic Force Microscopy," *Langmuir*, 15, 5630-5634.

Bobji, M. S., S. K. Biswas (1999) "Deconvolution of Hardness from data obtained from Nanoindentation of Rough Surfaces," *J. Mater. Res.*, 14, 15-23.

Bousfield, D.W., Wikstrom, M., M. Rigdahl (1998) "Roll Deformation During Blade Coating," *TAPPIJ.*, 81, 5, 207-212.

Burns, A. R., Houston, J. E., Carpick, R. W., T.A. Michalske (1999) "Molecular Level Friction As Revealed with a Novel Scanning Probe" *Langmuir*, 15,2922-2930.

Carvalho, M.S., L.E. Scriven (1995) "Effect of Deformable roll cover on Roll Coating," *TAPPI J.*, 77, 5,201-208.

Chaudhury, M. K. (1996) "Interfacial Interaction Between Low Energy Surfaces," *Materials Sci. Engin.*, R16, 19, 97-159.

Chaudhury, M. K. (1999) "Rate-Dependent Fracture at Adhesive Interface," *J. Phys. Chem. B*, 103, 6562-6566.

Chen, K.S.A., L.E. Scriven (1990) "Liquid Penetration into a Deformable Porous Substrate," *TAPPIJ.*, 73, 1, 151-161.

Coyle, D.J. (1998) "Forward Roll Coating with Deformable Rolls: A simple One-dimensional Elasto-Hydrodynamic Model," *Chem. Eng. Sci.*, 43,2673-2684.

Timoshenko, S. (1934) Theory of Elasticity, McGraw-Hill Book Co., New York.

Derjaguin, V., Muller, V. M., Y. P. Toporov (1975) "Effect of Contact Deformations on the Adhesion of Elastic Spheres," *J. Colloid Interface Sci.*, 53, 3 14-326.

Eklund, D., S. J. Kahila (1978) "Processes Occuring under the Blade during Blade Coating," *Wochbl.Papierfabr.*, 106, 66 1-665.

Engstrom, G., V. Morin (1995) "Analysis of the Processes of Formation and Consolidation in Blade Coating," Proceedings of the TAPPI Coating Fundamentals Symposium, Atlanta, GA, 4 1-50.

Falsafi, A., Deprez, P., Bates, F. S., M. Tirrell (1997) "Direct Measurement of Adhesion Between Viscoelastic Spheres: A contact Mechanics Approach," *J. Rheol.*, 41, 1349-1361.

Ferry, J. D. (1980) Viscoelastic Properties of Polymers, John Wiley & Sons: New York.

Findley, W. N., Lai, J. S., K. Onaran (1989) Creep and Relaxation of Nonlinear Viscoelastic Materials, Dover, Mineola, N.Y.

Ghatak, A., Vorvolakos, K., She, H., Malotky, D. L., M. K. Chaudhury (2000) "Interfacial Rate Processes in Adhesion and Friction," *J. Phys. Chem. B*, 104, 4018-4030.

Giri, M., Unertl, W. N., D. W. Bousfield (2000) "Stress Intensity in Adhesive Viscoelastic Contacts," *Tribology Letters*, 9, 33-39.

Giri, M., Unertl, W. N., D. W. Bousfield (2001) "Dynamic Contacts to Adhesive Viscoelastic Materials: Work of Adhesion," *Langmuir*, in press.

Giri, M., Unertl, W. N., C.-Y. Hui (2001) "Dynamic Contacts to Adhesive Viscoelastic Materials: Debonding Stress Intensities," *Macromolecules*, in preparation for submission.

Graham, G. A. C., G. C. W. Sabin (1973) "The Correspondence Principle of Linear Viscoelasticity for Problems that Involve Time-dependent Regions," *Int. J. Engng. Sci.*, 11, 123-140.

Greenwood, A. J., K. L. Johnson (1981) "The Mechanics of Adhesion of Viscoelastic Solids" *Phil. Mag. A*, 43, 697-711.

Greenwood, A. J. (1997) "Adhesion of Elastic Spheres," *Proc. R. Soc. Lond. A*, 453, 1277-1297.

Guler, E., D. W. Bousfield (1995) "Blade Force Measurements during Blade Coating," *Proceedings of the TAPPI coating Conference*, TAPPI press, Atlanta, GA, 53-65

Hagen, R., Salmen, L., A. deRuvo (1993) "Dynamic Mechanical Studies of a Highly Filled Composite Structure: A Lightweight Coated Paper," *J. of Appl. Poly. Sci.*, 48, 603-609.

Hay, J.C., Bolshakov, A., G. M. Pharr (1999) "A Critical Examination of Fundamental Relations used in the Analysis of Nanoindentation," *J. Maters. Res.*, 14, 2296-2305.

- Hill, L.W. (1987) Mechanical Properties of Coatings, *Federation Series on Coating Technology*, 1315 Walnut ST., Philadelphia, PA 19107 USA.
- Hui, C.-Y., Baney, J. M., E. J. Kramer (1998) "Contact mechanics and Adhesion of Viscoelastic Spheres," *Langmuir*, 14, 6570-6578.
- Hurtado, J. A., K. S. Kim (1999) "Scale effects in friction of single-asperity contacts: Part I; from concurrent slip to **single-dislocation-assisted** slip," *Proc. R. Soc. London. A*, 455, 3363-3384.
- Hurtado, J. A., K. S. Kim (1999) "Scale effects in friction of single-asperity contacts: Part II; **Multiple-dislocation-cooperated** slip," *Proc. R. Soc. London. A*, 455, 3385-3400.
- Inoue, M., P. LePoutre (1992) "Peel behavior of Clay Coatings," *J. Adhesion Sci. Technol.*, 6, 7, 851-856.
- Isaksson P., Engstrom, G., M. Rigdahl (1994) "Experimental Analysis of the Dynamic Equilibrium in the Vicinity of the Blade tip during Blade Coating," *Nordic Pulp and Paper Research J.*, 3, 150-155.
- Isaksson P., M. Rigdahl, (1994) "Numerical Simulation of Blade Coaters with short Dwell and Roll Application Coaters," *Rheol. Acta*, 33, 454-467.
- Ishikawa, O., Yamashita, T., A. Tsuji (1995) "Characterizing mechanical properties of latex film and coating layer in paper coating using dynamic mechanical thermal analyzer," in Surface Phenomena and Latexes in Waterborne Coatings and Printing Technologies, Plenum Press New York, 91-105.
- Johnson, K.L. (1978) "Adhesion at the Contact of Solids," in Theoretical and Applied Mechanics, Proc. 4<sup>th</sup> IUTAM Congress, North Holland, Amsterdam, Koiter, W.T.,S 133.
- Johnson, K. L. (1985) Contact Mechanics, Cambridge University Press.

- Johnson, K. L., Kendall, K., A. D. Roberts (1971) "Surface Energy and the Contact of Elastic Solids," *Proc. R. Soc. Lond. A*, 324,301-313.
- Johnson, K. L., J. A. Greenwood (1997) "An Adhesion Map for the Contact of Elastic Spheres," *J. Colloid and Interface Sci.*, 192,326-333.
- Johnson, K. L. (2000) "Contact Mechanics and Adhesion of Viscoelastic Spheres," Microstructure and Microtribology of Polymer Surfaces, eds., V. V. Tsukruk and K. J. Wahl, American Chemical Society, Washington, D.C., 23-36.
- Joyce, M., Hagen, R., and de Ruvo, A., Mechanical consequences of coating penetration, *Journal of Coatings Technology*, 1997, 69,869, 53-58.
- Kan, C.S., Kim, L.H., Lee, D.I., R. L. van Gilder (1997) "Viscoelastic Properties of Paper Coatings: Relationship between Coating Structure – Viscoelasticity and End use Performance," *TAPPIJ.*, 80,5, 191-201.
- Kuzmak, J.M., "Bevelled-Blade coating", *TAPPI J.*, 69(2): 72-75 (1986)
- Landman, U., Luedtke, W. D., Burnham, N. A., R. J. Colton (1990) "Atomistic Mechanisms and Dynamics of Adhesion, Nanoindentation and Fracture," *Science*, 248,454-461
- Lantz, M. A., O'Shea, S. J., Welland, M. E., Johnson, K.L. *Phys. Rev. B* 1997, 55, 10776.
- LePoutre, P. (1989) "The structure of paper coatings: An update," *Prog. in Org. Coat.*,17, 89-97.
- LePoutre, P., T. Hiraharu (1989) "On the Cohesion of Clay and CaCO<sub>3</sub> Coatings," Note in *J. App Poly. Sci.*, 37,2077-2079.
- Lin, Y. Y., Hui, C.-Y., J. M. Baney (1999) "Viscoelastic Contact, Work of Adhesion and the JKR Technique," *J. Phys. D: Appl. Phys.*, 32,2250-2260.
- Maugis, D (1995) "Extension of the Johnson-Kendall-Roberts Theory of the Elastic Contact of Spheres to large Contact Radii," *Langmuir*, 11, 679-682.

Maugis, D (1992) "Adhesion of Spheres: The JKR-DMT Transition using a Dugdale Model," *J. Colloid Interface Sci.*, 150, 243-269.

Mesarovic, S. Dj., K. L. Johnson (2000) "Deformation of Elastic-Plastic Adhesive Spheres," *J. Mech. Phys. of Solids*, 48, 2009-2023.

Nielsen, L.E. (1974) Mechanical Properties of Polymers and Composites, Dekker, New York, vol. 2.

Oliver, W. C., G. M. Pharr (1992) "An Improved Technique for determining Hardness and Elastic Modulus using load and displacement sensing Indentation experiments", *J. Mater. Res.*, 7, 1564-1583.

Ortman, B.J. D. W. Donigian (1992) "Coat Weight Non-uniformity due to High Speed Blade Coating: Mechanism and Prevention", Proceedings of the 1992 TAPPI Coating Conference, TAPPI Press, Atlanta, GA, 217-224.

Parpaillon, M., Engstrom, G., Pettersson, I., Fineman, I., Svanson, S.E., Dellenfalk, B., M. Rigdahl (1985) "Mechanical Properties of Clay Coating Films Containing Styrene-Butadiene Copolymers," *J. Appl. Poly. Sci.*, 30, 581-592.

Prall, K. (2000) Thesis on *Micromechanical Properties of Pigmented Coating Composites*, Department of Chemical Engineering, University of Maine, Orono, ME 04473, USA.

Pranckh, F.R., and L.E. Scriven (1990) "The physics of Blade Coating of Deformable Substrates," *TAPPIJ.*, 73, 1, 163-173.

Pfeiffer, J. D., *Finishing and Converting Conference Proceedings*, 1980, p. 19, TAPPI Press, Atlanta, GA.

Raman, K., Bousfield, D.W., and Shaler, S.M., Analyzing the effect of binder content on the mechanical properties of paper coatings, *TAPPI Coating Conference Proceedings*, Philadelphia, 1998.

Rief, M., Gautel, M., Oesterhelt, F., Fernandez, J. M., H. E. Gaub (1997) "The Detachment of Polymer Chains from a Weakly Adsorbing Surface using an AFM tip," *Science*, 276, 1109-1114.

Rief, M., Oesterhelt, F., Heymann, B., H.E. Gaub, (1997) "The Elasticity of Single polymer Chains," *Science*, 275, 1295-1298.

Rice, J. R. (1979) "Calculating the Energy release Rate for Crack Propagation in Viscoelastic Medium," Proc. 8<sup>th</sup> US Natl. Cong. Appl. Mech. Los Angeles: Western Periodicals, 191.

Rice, J. R. (1968) "A path independent Integral and the Approximate Analysis of Strain Concentration by Notches and Cracks," *J. Appl. Mech.*, 5, 379-386.

Rodal, J. J. A. (1989) "The Calendering of Paper," *TAPPIJ.*, 5, 177-187.

Saita, F.A., and L.E Scriven, "Coating Flow Analysis and the Physics of Flexible Blade Coating", Proc. TAPPI Coating Conference, TAPPI Press, pp. 13, Atlanta, GA (1985).

Schapery, R. A. (1975) "A Theory of Crack initiation and Growth in Viscoelastic Media **I**. Theoretical Development," *Int. J. Fracture*, 11, 1, 141-159.

Schapery, R. A. (1975) "A Theory of Crack initiation and Growth in Viscoelastic Media **11**. Approximate method of Analysis," *Int. J. Fracture*, 11, 3, 369-387.

Schapery, R. A. (1975) "A Theory of Crack initiation and Growth in Viscoelastic Media **111**. Analysis of Continuous growth" *Intl. J. Fracture*, 11, 4, 549-562.

Schapery, R. A. (1978) "A method for Predicting Crack Growth in Nonhomogenous Viscoelastic Media," *Intl. J. Fracture*, 14, 3, 293-309.

Schapery, R. A. (1989) "The Mechanics of Crack Closing and Bonding in Linear Viscoelastic Media," *Intl. J. Fracture*, 39, 163-189.

- Singer, I. L., H. M. Pollock (editors) (1992) Fundamentals of Friction: Macroscopic and Microscopic Processes, Kluwer Academic Publishers, Dordrecht, Netherlands.
- Tabor, D. (1948) "Plastic Deformation caused by Hard Steel Spheres on Flat Metallic Surfaces," *Proc. R. Soc. Lond.*, *A192*, 247, 181-186.
- Ting, T C. T. (1966) "The Contact Stress Between a Rigid Indenter and a Viscoelastic Half-Space," *J. Appl. Mech.*, **33**, 845-854,
- Ting, T.C.T. (1968) "Contact Problems in the Linear Theory of Viscoelasticity," *J. Appl. Mech.*, *J. Appl. Mech.*, **35**, 248-254.
- Toussaint, A. (1973) "Influence of pigmentation on the mechanical properties of paint films," *Progress in Org. Coatings*, *2*, 237-267.
- Triantafillopolous, N.G., N. Altug (1994) "Experimental Analysis of Forces in Bevelled Blade Coating," *Proc. TAPPI Coating Conference*, TAPPI Press, Atlanta, GA, 77-96.
- Turai, L.L. (1971) "Analysis of the Blade Coating Process," *TAPPIJ.*, **54**, 8, 1315-1318.
- Unertl, W. N., *Microstructure and Tribology of Polymers*, editors; V. V. Tsukruk and K. J. Wahl American Chemical Society, Washington, DC, **2000**.
- Unertl, W. N. (2000) "Creep Effects in Nanometer-scale Contacts to Viscoelastic Materials," *J. Adhesion*, **74**, 195-226.
- Unertl, W. N. (1998) "Adhesion of Styrene-Butadiene Latexes to Inorganic Mineral Surfaces," *Langmuir*, *14*, 2201-2207.
- Van Gilder, R.L., R. D. Purfeerst (1994) "Effect of Binder type on the Printing Behavior of Pigmented Coatings in a Six-sheet Offset Press," *TAPPIJ.*, **77**, 5, 230-240.
- Wahl, K. J., Stepnowski, S. V., W. N. Unertl (1998) "Viscoelastic Effects in Nanometer- scale Contacts Under Shear," *Tribology Lett.*, **5**, 103-107.

Wang, Y., D. Juhue, M. A. Winnik., O.M. Leung., M. C. Goh (1992) "Atomic Force Microscopy Study of Latex Film Formation," *Langmuir*, 8, 760-763.

Woodland D. D, W. N. Unertl (2001) "Wetting and Spreading Behavior of Styrene-Butadiene Latexes," to be Published.

Yamaguchi, Y., Ishikawa, O., Yamashita, T., A. Tsuji (1993) "A Study of Viscoelastic Properties of Coated Layer in Paper Coating", *TAPPI Advanced Coating Fundamentals*, 5 1-58.

Yang, W.H., *J. Appl. Mech.*, 1968, 35, 379.

Yang, X., Bousfield, D.W., Kettle, J., Hultgren, L., P. Hayes, (2001) "Ink Tack Development in Pigmented Coatings," *Proc. of the TAPPI Fundamental Coating Conference*, TAPPI Press, San Diego, CA.

Yang, X., D. W. Bousfield (1998) "A new Technique to Analyze Back Trap Mottle," *Proc. 1998 TAPPI Coating Conference*, TAPPI Press, New Orleans, LA, 335.

Young, R. J., P. A. Lovell (1991) *Introduction to Polymers*, Second edition, Chapman & Hall, London.

Zosel, A., (1980) "Mechanical behavior of coating films," *Prog. in Org Coat.*, 8, 47-79.

### Appendix A: MathCad file extract for Johnson's crack tip creep approach

This appendix contains the MathCad file for the crack tip creep approach proposed by Johnson. The details of this theory are described in section 3.2.1. This MathCad files a typical fitting approach Latex # 4. The latex material properties were determined from Dynamic Mechanical Testing as described in chapter 4. The two fitting parameters that were used in this procedure are Wand  $h_o$ ,

1. The parameters of the three-body solid are given in chapter 4.
2. The assumed values of Wand  $h_o$  (in SI units) are

$$\Delta\gamma := 0.076 \quad h_o := 5.1 \cdot 10^{-10}$$

3. The applied load is given by,

$$P_o := 20.0 \cdot 10^{-6} \quad \text{Pod} := \frac{P_o}{3 \cdot \pi \cdot R \cdot \Delta\gamma} \quad \text{Pod} = 2.792$$

where Pod is the dimensionless form for applied load  $P_o$ .

4. The loading rate is given by,

$$D := \frac{\text{Pod}}{t_o} \quad D = 6.98$$

where  $t_o$  is 0.4s in this particular case

5. The dimensionless constant  $A$  is given by,

$$A := \left[ \frac{36 \cdot R \cdot \Delta\gamma}{\pi \cdot h_o^3 \cdot E} \right]^{\frac{2}{3}} \cdot \tau \cdot D \quad A = 104.533$$

**For the bonding part (increasing contact radius), the differential equation is:**

$$y'(t) = 3 \cdot (2 \cdot y(t) \cdot t)^{\frac{1}{2}} - 3 \left( \frac{y(t)}{t} \right) - \left( \frac{2 \cdot y(t)^3}{t^3} \right)^{\frac{1}{2}} \cdot A \cdot \ln \left( \frac{1 - k}{1 - y(t)} \right)$$

with the boundary condition given by,

$$y(0.01) = 0.0001$$

The differential equation is solved using the ODESOLVE routine provided in MathCad. The statement looks like,

$$y := \text{odesolve}(t, \text{num1}, 500)$$

where *num 1* is just a dimensionless parameter corresponding to the point to maximum contact radius. The number in the last placeholder indicates the number of points between the initial of contact and num1 .

**For the debonding part (decreasing contact radius), the differential equation is:**

$$y'(t) = 3 \cdot (2y(t) \cdot t)^{\frac{1}{2}} - 3 \left( \frac{y(t)}{t} \right) - \left( \frac{2}{t^3 \cdot y(t)} \right)^{\frac{1}{2}} \cdot A \cdot \ln \left( \frac{1-k}{1 - \frac{1}{y(t)}} \right)$$

with the boundary condition given by,

$$y(\text{num2}) = 0.986$$

The same ODESOLVE routine is used to solve this differential equation. Once both  $\beta$  and  $a$  are known for both the bonding and debonding parts, then we can compute load (**P**) as well as displacement ( $\delta$ ) using the relations given by,

$$\bar{P} = \bar{a}^3 - \sqrt{2\beta\bar{a}^3} \quad \text{and} \quad \bar{\delta} = 3^{2/3} \bar{a}^{-2} \left[ 1 - \frac{2\sqrt{3}}{3} \bar{a}^{-3/2} \right], \quad \text{where } \bar{a} \text{ is the dimensionless radius and}$$

the displacement,  $\delta$ , is related to its dimensionless form by  $\delta = \left( \frac{9\pi^2 W^2 R}{16E_\infty^2} \right)^{1/3} \bar{\delta}$ . Once both  $\delta$  and **P** are known for the bonding and debonding part we can model the hysteresis curve;

### Appendix B: MathCad file extract for the HBKL complete approach

This appendix contains basic elements of the MathCad file for the Hui, Baney, Kramer and Lin approach for treating adhesive viscoelastic contacts. The details of this theory are described in section 3.2.2 and 3.2.3. This MathCad files is used for determining the stress intensity factor for an entire bonding-debonding cycle for Latex # 3. The latex material properties were determined from Dynamic Mechanical Testing as described in chapter 4.

The constants that need to be predetermined are the cohesive zone parameters ( $W$  and  $h_o$ ),  $C_m, \gamma_m$  and  $\omega$ . The material compliance,  $C(t)$ , is given by the power law in equation (2) (replace  $n$  by  $q$  for the MathCad procedure shown below) of section 3.2.1.  $dPdt$  stands for the loading rate,  $mlp$  indicates the maximum load point whereas  $mxl$  denoted maximum displacement point.

For the increasing load of the bonding portion the following routine was used.

```

aload := | i ← 0
         | while i < mlp
         |   | aload0 ← a0
         |   | Z0 ←  $\frac{1}{8 \cdot \pi \cdot W \cdot C(t_0) \cdot (aload_0)^3} \left[ \frac{8 \cdot (aload_0)^3}{3 \cdot R} - dPdt \cdot \left[ Co \cdot t_0 + \frac{C1 \cdot (t_0)^{q+2}}{(q+1) \cdot (q+2)} \right] \right]^2$ 
         |   | λi ←  $\frac{1}{2} \cdot \left( Cm \cdot Z_i + \sqrt{Cm \cdot Z_i} \cdot \sqrt{Cm \cdot Z_i + \frac{4}{Cm} - 4} \right) - 1$ 
         |   | daloaddti+1 ←  $\omega \cdot \frac{(\lambda_i)^{-1}}{(1 + \dots)} \cdot \frac{1}{8 \cdot \pi \cdot W \cdot C(t_i) \cdot (aload_i)^3} \left[ \frac{8 \cdot (aload_i)^3}{3 \cdot R} - dPdt \cdot \left[ Co \cdot t_i + \frac{C1 \cdot (t_i)^{q+2}}{(q+1) \cdot (q+2)} \right] \right]^2$ 
         |   | aloadi+1 ← daloaddti+1(ti) + aloadi
         |   | Zi+1 ←  $\frac{1}{8 \cdot \pi \cdot W \cdot C(t_i) \cdot (aload_{i+1})^3} \left[ \frac{8 \cdot (aload_{i+1})^3}{3 \cdot R} - dPdt \cdot \left[ Co \cdot t_{i+1} + \frac{C1 \cdot (t_{i+1})^{q+2}}{(q+1) \cdot (q+2)} \right] \right]^2$ 
         |   | i ← i + 1
         |   | aload

```

Fig. B.1 A MathCad subroutine showing the incremental method used to calculate contact radius  $a$ , using the Schapery's method, for the increasing load portion. Here  $aload$  indicates the contact radius during this loading portion of the curve

For the creep part for the bonding portion the contact radius,  $a_u$ , is given by the following routine. It should be noted that the load is decreasing in this portion of the load-displacement curve.

```

au := | i ← mlp
      | while i < mxd
      |   au_mlp ← Re(a_load_mlp)
      |   Z_mlp ←  $\frac{1}{8 \cdot \pi \cdot W \cdot C(t_{mlp}) \cdot (a_{u\_mlp})^3} \left[ \frac{8 \cdot (a_{u\_mlp})^3}{3 \cdot R} + dPdt1 \cdot \left[ Co \cdot t_{mlp} + \frac{C1 \cdot (t_{mlp})^{q+2}}{(q+1) \cdot (q+2)} \right] \right]^2$ 
      |    $\lambda_i \leftarrow \frac{1}{2} \cdot \left( Cm \cdot Z_i + \sqrt{Cm \cdot Z_i} \cdot \sqrt{Cm \cdot Z_i + \frac{4}{Cm} - 4} \right) - 1$ 
      |   daudt_{i+1} ←  $\omega \cdot \frac{(\lambda_i)^{-1/m1}}{(1 + \lambda_i)^2} \cdot \frac{1}{8 \cdot \pi \cdot W \cdot C(t_0) \cdot (a_{u_i})^3} \left[ \frac{8 \cdot (a_{u_i})^3}{3 \cdot R} + dPdt_i \cdot \left[ Co \cdot (t_i) + \frac{C1 \cdot (t_i)^{q+2}}{(q+1) \cdot (q+2)} \right] \right]^2$ 
      |   au_{i+1} ← daudt_{i+1}(t_i) + au_i
      |   Z_{i+1} ←  $\frac{1}{8 \cdot \pi \cdot W \cdot C(t_{mlp}) \cdot (a_{u_{i+1}})^3} \left[ \frac{8 \cdot (a_{u_{i+1}})^3}{3 \cdot R} + dPdt_i \cdot \left[ Co \cdot (t_i) + \frac{C1 \cdot (t_i)^{q+2}}{(q+1) \cdot (q+2)} \right] \right]^2$ 
      |   i ← i + 1
      | au

```

Fig. B.2 Fig. B.1 **A** MathCad subroutine showing the incremental method used to calculate contact radius  $a$ , using the Schapery's method, for the creep portion of the loading-unloading cycle.

```

kl := | for i ∈ 0..mxd
      |    $kl_i \leftarrow \frac{4 \cdot (a_{C_i})^3 - 3 \cdot R \cdot \left[ dPdt1 \cdot \left[ Co \cdot t_i + \frac{C1 \cdot (t_i)^{q+2}}{(q+1) \cdot (q+2)} \right] \right]}{6 \cdot \sqrt{\pi} \cdot R \cdot Co \cdot (a_{C_i})^{\frac{3}{2}}}$  if i < mlp
      |    $kl_i \leftarrow \frac{4 \cdot (a_{C_i})^3 + 3 \cdot R \cdot \left[ dPdt1 \cdot \left[ Co \cdot t_i + \frac{C1 \cdot (t_i)^{q+2}}{(q+1) \cdot (q+2)} \right] \right]}{6 \cdot \sqrt{\pi} \cdot R \cdot Co \cdot (a_{C_i})^{\frac{3}{2}}}$  otherwise

```

Fig. B.3 **A** MathCad subroutine showing the incremental method used to calculate the stress intensity factor,  $K_I$  for the crack closing portion of the hysteresis cycle.

For the debonding portion, a functional form for the contact radius is assumed. This functional form is given by,

$$a(t_u) = a_{\max} - At,^3 - Bt,^2$$

where  $a_{\max}$  is the maximum contact radius and **A** and **B** are arbitrary constants.  $t_u$  is the time during debonding. The relationship between the contact radius and contact depth is given by,

$$\delta(t_u) = \frac{a(t_u)^2}{R} - \sqrt{\frac{2\pi W a(t_u)}{E(t_u)}}$$

The stress intensity for the debonding portion is then calculated using equation 36 described in section 3.2.3.

### **Biography of the Author**

Manish Giri was born on the 18<sup>th</sup> of August, 1973 in Jamshedpur, Bihar, India. He graduated from the Air Force School, New Delhi in May 1992. In May 1996 he received his Bachelor of Engineering from the University of Roorkee, Roorkee, India. He then moved to the United States of America to continue higher education. In June 1998 he received his Masters of Science degree in Chemical Engineering from the Oregon State University in Corvallis, Oregon. In August 1998 Manish began his Ph.D. program in Chemical Engineering at the University of Maine.

During his graduate studies at the University of Maine, Manish worked on the research projects sponsored by the Paper Surface Science Program (PSSP) at the University of Maine. Manish is a member of the Society of Rheology, Adhesion Society, American Chemical Society and the American Vacuum Society. He is a candidate for the Doctor of Philosophy degree in Chemical Engineering from The University of Maine in August, 2001.